On the relation between seismic source dynamics, tsunami generation and propagation, and numerical modelling complexity for large earthquakes in subduction zones

Antonio Scala[1], Stefano Lorito[2], Cipriano Escalante Sanchez[3], Fabrizio Romano[2], Gaetano Festa[1], Alice Abbate[2], Hafize Basak Bayraktar[2], Manuel Jesús Castro Díaz[3], Jorge Macías[4], and José Manuel González-Vida[4]

[1]Università di Napoli Federico II
[2]Istituto Nazionale di Geofisica e Vulcanologia
[3]Universidad de Malaga
[4]Universidad de Málaga

January 23, 2024

Abstract

Tsunamis are rare, destructive events, whose generation, propagation and coastal impact processes involve several complex physical phenomena. Most tsunami applications, like probabilistic tsunami hazard assessment, make extensive use of large sets of numerical simulations, facing a systematic trade-off between the computational costs and the modelling accuracy. For seismogenic tsunami, the source is often modelled as an instantaneous sea-floor displacement due to the fault static slip distribution, while the propagation in open-sea is computed through a shallow water approximation.

Here, through 1D earthquake-tsunami coupled simulations of large M>8 earthquakes in Tohoku-like subduction zone, we tested for which conditions the instantaneous source (IS) and/or the shallow water (SW) approximations can be used to simulate with enough accuracy the whole tsunami evolution. We used as a reference a time-dependent (TD), multi-layer, non-hydrostatic (NH) model whose source features, duration, and size, are based on seismic rupture dynamic simulations with realistic stress drop and rigidity, within a Tohoku-like environment.

We showed that slow ruptures, generating slip in shallow part of subduction slabs (e.g. tsunami earthquakes), and very large events, with an along-dip extension comparable with the trench-coast distance (e.g. mega-thrust) require a TD-NH modelling, in particular when the bathymetry close to the coast features sharp depth gradients. Conversely, deeper, higher stress-drop events can be accurately modelled through an IS-SW approximation. We finally showed to what extent inundation depend on bathymetric geometrical features: (i) steeper bathymetries generate larger inundations and (ii) a resonant mechanism emerges with run-up amplifications associated with larger source size on flatter bathymetries.

On the relation between seismic source dynamics, tsunami generation and propagation, and numerical modelling complexity for large earthquakes in subduction zones

A. Scala[1,2], S. Lorito[2], C. Escalante Sánchez[3], F. Romano[2], G. Festa[1,2], A. Abbate[2,4], H. B. Bayraktar[2], M. J. Castro[3], J. Macías[3], J. M. Gonzalez-Vida[3]

[1] Department of Physics "Ettore Pancini", University Federico II, Napoli, 80126, Italy.

[2] Istituto Nazionale di Geofisica e Vulcanologia, Rome, 00143, Italy

[3] EDANYA Group, University of Malaga, Malaga, 29080, Spain

[4] Department of Mathematics, Informatics and Geosciences, University of Trieste, 34128, Italy

Corresponding author: Antonio Scala (antonio.scala@unina.it)

Key Points:

- Slow and large ruptures (e.g. tsunami earthquakes and mega-thrust) require a time-dependent, non-hydrostatic modelling
- Deeper, high stress-drop earthquakes might be modelled through an instantaneous source, shallow water approximation
- Inundation depends on bathymetric features: larger inundations on steeper depth gradients and resonant run-up amplifications are observed

Abstract

Tsunamis are rare, destructive events, whose generation, propagation and coastal impact processes involve several complex physical phenomena. Most tsunami applications, like probabilistic tsunami hazard assessment, make extensive use of large sets of numerical simulations, facing a systematic trade-off between the computational costs and the modelling accuracy. For seismogenic tsunami, the source is often modelled as an instantaneous sea-floor displacement due to the fault static slip distribution, while the propagation in open-sea is computed through a shallow water approximation.

Here, through 1D earthquake-tsunami coupled simulations of large M>8 earthquakes in Tohoku-like subduction zone, we tested for which conditions the instantaneous source (IS) and/or the shallow water (SW) approximations can be used to simulate with enough accuracy the whole tsunami evolution. We used as a reference a time-dependent (TD), multi-layer, non-hydrostatic (NH) model whose source features, duration, and size, are based on seismic rupture dynamic simulations with realistic stress drop and rigidity, within a Tohoku-like environment.

We showed that slow ruptures, generating slip in shallow part of subduction slabs (e.g. tsunami earthquakes), and very large events, with an along-dip extension comparable with the trench-coast distance (e.g. mega-thrust) require a TD-NH modelling, in particular when the bathymetry close to the coast features sharp depth gradients. Conversely, deeper, higher stress-drop events can be accurately modelled through an IS-SW approximation. We finally showed to what extent inundation depend on bathymetric geometrical features: (i) steeper bathymetries generate larger inundations and (ii) a resonant mechanism emerges with run-up amplifications associated with larger source size on flatter bathymetries.

Plain Language Summary

In the last two decades, tsunamis originated by large earthquakes have generated major damages and more than 250k casualties. Strategies to quantify and mitigate the associated risk are based on numerical simulations of the physical processes regulating the generation, propagation of the waves and subsequent flooding on the coast. These simulations would require unaffordable computational resources; to solve this problem, numerous approximations are introduced that need to be tested. In this work, we studied which earthquakes, depending on the speed at which they deform the sea bottom when they trigger a tsunami, and on how big they are, require a more detailed modelling approach, and which ones, instead, might be accurately simulated through approximated approaches. We also show how such findings are related to different bathymetric characteristics near the coast and inland, which may enhance or reduce the tsunami effects.

1 Introduction

Due to the rare occurrence of tsunamis and the strong influence of bathymetry and coastal morphology on tsunami evolution, tsunami community makes use of numerical simulations to compensate for the scarcity of observations (see e.g. Behrens et al., 2021; Sugawara, 2021; Babeyko et al., 2022). Here, we consider tsunamis generated by earthquakes in subduction zones, since the most destructive tsunamis in the last decades were generated by interslab subduction events (Grezio et al., 2017; Davies & Griffin, 2020). For these sources, tsunami simulations require the numerical modelling of the earthquake source process, the solid-fluid interaction during the tsunami generation, and the wave propagation on a complex bathymetry up to the inundation of the coastal topography. Numerical modelling of these diverse physical processes typically requires different solvers with a certain level of coupling between them. They range from the simplest solution consisting of instantaneous seafloor from a static slip (Okada, 1985) to more complex modelling implementing either a two-step (Saito et al., 2019) or a fully coupled approach to describe the seismic and the tsunami source processes (Lotto & Dunham, 2015; Lotto et al., 2019).

Each solver adopts approximations and simplifications to limit the computational cost associated with the simulations. This is particularly relevant when an application requires many high-resolution simulations, such as in probabilistic tsunami hazard analysis (PTHA, Grezio et al., 2017; Davies et al., 2018; Gibbons et al., 2020; Basili et al., 2021; Behrens et al., 2021), inverse problems (Romano et al., 2020, 2021), or tsunami forecasting for early warning purposes (Selva et al., 2021). One way to cope with the containment of the computational cost is to approximate the tsunami height after shoaling, or the runup process with analytical or stochastic methods (Brocchini & Peregrine, 1996; Gailler et al., 2018; Glimsdal et al., 2019; Souty & Gailler, 2021). Recently, an emerging way to approach the problem is to exploit emulators as surrogates of the simulations (Gopinathan et al., 2021; Ehara et al., 2023) or AI-based techniques to estimate the inundation parameters from offshore or low-resolution simulations (Makinoshima et al., 2021; Ehara et al., 2023). From a distinct perspective, the computational cost of numerical modeling can be reduced without losing resolution by opportunely decreasing the number of simulations. This can be done by performing an optimal sampling of the parameter space (e.g. Davies et al., 2022), or by exploiting the similarity of tsunami scenarios due to different earthquake sources (e.g. Williamson et al., 2020).
All these strategies are complementary to the purpose of this study, which aims to establish an optimal simulation strategy for the specific case of large earthquakes in subduction zones and the ensuing tsunamis.

The subduction slab is often represented as a planar or a segmented interface (LeVeque et al., 2016; Li et al., 2016; Sepúlveda et al., 2017). However, recently, curved surfaces are being modelled increasingly often (Nakano et al., 2020; Scala et al., 2020; Tonini et al., 2020). The seismic rupture on the interface is modelled as an instantaneous elastic dislocation, or as the linear superposition of dislocations of different amplitude representing heterogeneous slip distributions, in a homogeneous half-space (Okada, 1985; Meade, 2007). The resulting instantaneous elastic deformation of the sea floor is eventually smoothed (Kajiura, 1963) to obtain a static sea surface anomaly, that generates waves owing to gravity. The tsunami propagation is then numerically computed in the nonlinear shallow water approximation (Stoker J. J., 1992) until the coastal inundation, fully neglecting dispersive wave effects.

However, the rupture process has a finite duration and the zones affected by elastic dislocation change as the seismic rupture expands. The spatial and temporal scales of the seismic rupture process, controlled by roughness, size and speed, have a wide range of variability making the above-mentioned approximations valid depending on specific applications (see Abrahams et al., 2023 and references therein). At the first order, we can characterize the scales through the duration and extent of the initial sea level perturbation which, in turn, can be related to the average rigidity and the stress drop of the seismic source (Bilek & Lay, 1999; Geist & Bilek, 2001). On the other hand, the generation process cannot always be accurately modelled as an instantaneous deformation smoothed with a Kajiura filter as input to a shallow water model to propagate the initial static displacement. For slow ruptures, or short-wavelength sea bottom displacements, a more accurate modelling of the time-dependent coupling between the sea bottom and the water layer, and of the subsequent tsunami evolution may be necessary (see, as well, the discussion in Abrahams et al., 2023 and references therein). Beyond that, several numerical comparisons against experimental data (Ma et al., 2012; Macías et al., 2021a, 2021b) demonstrated that accounting for dispersive effects is essential for faithfully simulating waves in the vicinity of the continental shelf, as well as to model run-up, shoaling, and wet-dry areas. Although in a different tectonic setting (outer-rise normal faulting) the dispersive effects might amplify tsunami waves (Baba et al., 2021). To enhance the model's non-linear dispersive properties, it is crucial also to include information on the vertical structure of the flow. In Macías et al. (2021a, 2021b), waves generated after rigid or granular landslides were found to be high frequency and dispersive, with the generated flows exhibiting a complex vertical structure.

Here, we aim to address if and for which cases a modelling of time-dependent rupture complexity and non-hydrostatic regime accounting for a more physically realistic modelling of seismic source and tsunami processes, respectively, are necessary to guarantee the accuracy of the results for the forecasting of tsunamis generated by large earthquakes in subduction zones. At the same time, we approach this problem keeping in mind the compromise between accuracy and computational demand for practical applications. Thus, a complementary goal is to identify, depending on the cases, which is the minimum computational effort needed to preserve an acceptable accuracy in the results.

In this work we start with the 1D time-dependent sea-level displacement (along the x -direction of the sketch in Figure 1a) generated by a 1D numerical model of the seismic rupture (Murphy et al., 2016, 2018; Scala et al., 2017, 2019). This displacement is the input for the 1D tsunami generation and evolution with a non-hydrostatic 3-layer tsunami code (Escalante et al., 2019, 2023). The bathymetry and topography adopted in this study are simplified 1-D versions of transects perpendicular to the coast of Tohoku in Japan. This setup is used as the 'ground-truth' to benchmark more simplified approaches using either instantaneous seafloor displacement, or a one-layer shallow water scheme, or a combination of the two. Although we are aware of the limitations of the 1D approach, it allows us to perform a large number of simulations spanning a broad range of rupture velocities and extensions on different bathymetric profiles and coastal slopes, and with enough spatial resolution to perform inundation modelling. The metrics used to validate the different approaches/approximations are the sea-surface evolution, the offshore maximum wave amplitude at different depths, seaward and landward from the trench, the flow depth and the maximum runup inland.

The paper is organized as follows: the coupled modeling of earthquake and tsunami and the numerical setup are presented in sections 2 and 3, respectively. In section 4 the results are described, while discussions about results and final remarks can be found in sections 5 and 6, respectively.

2 Methods: Coupling modelling of earthquake and tsunami

2.1 Earthquake rupture dynamics modelling

To model 1D earthquake rupture dynamics in a 2D elastic domain, we used the same approach proposed in Scala et al. (2017, 2019). We solve the general elastodynamic problem:

$$\begin{cases} \rho(x)\ddot{u}(x,t) = \vec{\nabla}\cdot\sigma(x,t) \\ \sigma(x,t) = c(x){:}\vec{\nabla}u(x,t) \end{cases} \tag{1}$$

In equation (1), x is the position, t the time, $\rho(x)$ is the bulk density, $\sigma(x,t)$ and $c(x)$ the stress and the elastic coefficient tensors respectively, while $u(x,t)$ represents the particle displacement. The traction $T = \sigma \cdot n$ is imposed to be zero on the seafloor interface, neglecting the acoustic coupling between the seafloor and the water itself.

The fault is modelled through a domain decomposition around a 1D interface where the continuity of the traction T is imposed. The fault slip and slip rate are defined as $\delta u(\tilde{x},t) = u_2(x_2,t) - u_1(x_1,t)$ and $\delta v(\tilde{x},t) = v_2(x_2,t) - v_1(x_1,t)$ respectively, with $\tilde{x}$ representing a generic point on the interface while the subscripts 1 and 2 mark the quantities computed on the two sides of the fault. The contact between the two sides of the fault is modelled through the Signorini's condition: the normal traction is either negative and hence the two lips are in contact and prone to frictionally slide or equal to zero, making each side of the interface a free surface and generating an opening (see also eq. (2) in Scala et al., 2019). When the two sides of the fault interface are in contact, the frictional sliding is governed by the following Coulomb condition:

$$\begin{cases} [T^t(\tilde{x},t) - C(\tilde{x}) + fT^n(\tilde{x},t)]\cdot|\delta v^t(\tilde{x},t)| = 0 \\ [T^t(\tilde{x},t) - C(\tilde{x}) + fT^n(\tilde{x},t)] \leq 0 \end{cases} \tag{2}$$

In equation (2), the superscripts t and n represent the tangential and normal directions with respect to the interface, C is a level of remote cohesion on the fault that is assumed to decrease to zero approaching the free surface. The friction f is here assumed to linearly decrease with slip from a static level f_s to a dynamic one f_d over a finite length of slip D_c (Slip weakening; Ida, 1972).
Elastodynamic equations with a sliding interface are numerically solved through a 2D Spectral Element Method (SEM, Komatitsch & Vilotte, 1998) where quadrangular elements are discretized using $9x9$ Gauss-Lobatto-Legendre nodes, ensuring at least 5 points for the minimum propagating wavelength and at least 4 points to model the fault cohesive zone (Scala et al., 2017).The free surface is naturally modelled in SEM while the other boundaries mimic an infinite half-space through the implementation of PMLs (Festa & Vilotte, 2005).
A Newmark second order forward time scheme is implemented with an average Courant number of about 0.04. Such a small value allows to model the shallowest part of the domain honouring the shape of the domain between the fault and the free surface, and ensuring the stability also in the stretched elements within this wedge.
The fault is modelled as a planar interface embedded in a homogeneous medium and forming a dip angle $\delta = 20°$ with the horizontal direction similarly to what proposed by Scala et al., (2019). The free surface, in turn, is inclined of an angle $\alpha = 3.5°$ with respect to the horizontal direction, this value being an average of the bathymetry slopes for the different profiles in the vicinity of the trench (Figure 1). Since we aim to model a simplified Tohoku-like environment in terms of fault

geometry and topo-bathymetric distributions (see Section 2.4 for more details), the dip angle represents an average value between the almost horizontal trench and the steeper slope of the deep crust-mantle interface as shown in other works (Kozdon & Dunham, 2013; Murphy et al., 2018) implementing 1D extrapolations of Slab 2.0 modelling (Hayes et al., 2018).

The remote stress field is oriented to mimic the combination of a vertical lithostatic and a horizontal tectonic loading. Their components are compatible with a reverse frictional sliding mechanism as expected for interface subduction events. On the fault interface the initial normal traction $T_0^n(\tilde{x}, t)$ linearly increases to mimic the increase of lithostatic loading (Huang et al., 2012; Murphy et al., 2016, 2018). The static and the dynamic friction coefficients f_s and f_d are imposed to be equal to 0.25 and 0.05 respectively to prevent the opening at the free surface (Scala et al., 2019). The strength excess $s = (f_s T_0^n - T_0^t)/(T_0^t - f_d T_0^n)$ is set to 2 on the entire interface to avoid the acceleration of rupture toward supershear regimes (Burridge, 1973), since it was never observed during the largest reverse subduction tsunamigenic earthquakes. Therefore, the shear strength $f_s T_0^n$ the dynamic level $f_d T_0^n$, the initial shear stress T_0^t and the local stress drop $T_0^t - f_d T_0^n$ increase with depth accordingly to T_0^n. A cohesion C vanishing toward the fault-free surface intersection is imposed with a value of about 10% of the maximum stress

All the input/output physical quantities are normalised to infer general results from the simulations. The slip on the fault δu and the ensuing displacement on the surface d are normalised by means of the critical slip weakening distance leading to the dimensionless parameters $\widetilde{\delta u} = \delta u / D_c$ and $\tilde{d} = d / D_c$. All the tractions T are normalised through the maximum stress drop on the fault $\Delta\sigma_0$ as $\tilde{T} = T/\Delta\sigma_0$. The distances z, including the fault extension W and the ensuing tsunami source size λ (See Figure 1), and the time t are normalised as $\tilde{z} = \frac{\Delta\sigma_0}{\mu D_c} z$ and $\tilde{t} = \frac{V_s \Delta\sigma_0}{\mu D_c} t = \frac{\Delta\sigma_0}{V_s \rho D_c} t$ respectively. In these two latter normalisation factors, μ and ρ are the medium rigidity and density respectively with $V_s = \sqrt{\mu/\rho}$ the S-wave propagation velocity. This setup allows us to define an ensemble of different tsunami sources featuring a broad range of source extensions and durations running a single dimensionless earthquake simulation and selecting parameters like $D_c, \Delta\sigma_0, \mu$ and ρ in realistic ranges constrained by observations (see details in Section 3).

To trigger the spontaneous crack, we defined an asperity featuring an initial shear stress larger than the shear strength and having a size L_c large enough to allow the rupture to move away from the nucleation zone (Uenishi & Rice, 2003) .The nucleation asperity is placed at an intermediate depth with respect to the whole domain. Previous numerical experiments have shown that this is the preferential nucleation depth to generate events rupturing the whole domain and hence to describe the behaviour of a megathrust earthquake (Murphy et al., 2018).

2.2 Tsunami modelling

We used a multilayer shallow-water non-hydrostatic model. The multilayer approach was introduced by Audusse et al. (2011) and Fernández-Nieto et al. (2014) to capture vertical effects in shallow flows. The equations are depth-averaged at every layer, leading to a layer-wise constant approximation. Such a technique was already efficiently applied to landslide-generated tsunamis (Macías et al., 2021a) and for dry granular flows (Escalante et al., 2023a). Concerning dispersion, following the pioneering work of Casulli (1999), non-hydrostatic effects are incorporated into the shallow water framework by splitting the total pressure into hydrostatic and non-hydrostatic components, providing a given profile for the non-hydrostatic component and the vertical velocity, together with the incompressibility condition. This approach has been recently further developed improving the dispersive layer-averaged approximations (Fernández-Nieto et al., 2018; Escalante et al., 2023b), and efficiently GPU-implemented using finite volume and finite difference schemes (Escalante et al., 2018). A vertical discretization of the fluid into several layers only approximates the physics of the fluid. The number of layers can be increased to bring the system close to three-dimensional solvers, becoming able of adequately describing the vertical structure of the flow. That leads to notable improvements in the dispersion properties of the model. The multilayer model used in this study is the following (see, Fernández-Nieto et al., 2018):

$$
\begin{gathered}
\partial_t h + \partial_x (h\bar{u}) = 0, \\
\partial_t (h_\alpha u_\alpha) + \partial_x (h_\alpha u_\alpha^2) + g h_\alpha \partial_x \eta + u_{\alpha+1/2}\Gamma_{\alpha+1/2} - u_{\alpha-1/2}\Gamma_{\alpha-1/2} \\
= -\frac{1}{2} h_\alpha \partial_x \big(p_{\alpha+1/2} + p_{\alpha-1/2}\big) + \big(p_{\alpha+1/2} - p_{\alpha-1/2}\big)\partial_x z_\alpha + K_{\alpha-1/2} - K_{\alpha+1/2} - \tau_\alpha^u, \\
\partial_x (h_\alpha w_\alpha) + \partial_x (h_\alpha w_\alpha u_\alpha) + w_{\alpha+1/2}\Gamma_{\alpha+1/2} - w_{\alpha-1/2}\Gamma_{\alpha-1/2} = -h_\alpha \big(p_{\alpha+1/2} - p_{\alpha-1/2}\big) - \tau_\alpha^w.
\end{gathered}
\tag{3}
$$

In the system (3), $h(x,t)$ represents the total water height at each point $x \in \Omega \subset R$, and time $t \geq 0$, where Ω is the considered (horizontal) domain. The water height is decomposed along the vertical axis into a prescribed number of layers $L \geq 1$ (see Figure S1 in Supporting Information). For any layer α, its thickness will be assumed to be $h_\alpha = l_\alpha h$, for some values $l_\alpha \in (0,1)$ such that $\sum_{\alpha=1}^{L} l_\alpha = 1$. Usually, $l_\alpha = 1/L$ is selected. The upper and lower interfaces of the layer α are represented by $z_{\alpha+1/2}$ and $z_{\alpha-1/2}$, respectively, that is, $z_{\alpha+1/2} = z_b + \sum_{\beta=1}^{\alpha} l_\beta h$. The uppermost interface corresponds to the sea surface, denoted by $\eta(x,t) = h(x,t) + z_b(x,t)$; the lowermost one corresponds to the seafloor basin represented by $z_b(x,t)$, which is supposed to be perturbed by the earthquake. Finally, $z_\alpha = \frac{1}{2}\big(z_{\alpha-1/2} + z_{\alpha+1/2}\big)$ denotes the level of the middle point of the layer. The depth-averaged velocities in the horizontal and vertical directions are written as $u_\alpha(x,t)$, and $w_\alpha(x,t)$, respectively. Finally, $p_{\alpha+1/2}$ denotes the non-hydrostatic pressure at the interface $z_{\alpha+1/2}$, and is assumed to be 0 at the free surface. The mean of the depth-averaged horizontal velocities is indicated by $\bar{u} = \sum_{\alpha=1}^{L} l_\alpha u_\alpha$.

Moreover, for any field $f \in \{u,\ w\}$, we denote $f_{\alpha+1/2} = \frac{1}{2}(f_{\alpha+1} + f_\alpha)$. As usual $g = 9.81\ m/s^2$ is the gravity acceleration and $\Gamma_{\alpha+1/2}$ parametrizes the mass transfer across interfaces:

$$
\Gamma_{\alpha+1/2} = \sum_{\beta=\alpha+1}^{L} \partial_x \Big(h_\beta \big(u_\beta - \bar{u}\big)\Big),
\tag{4}
$$

where we assume no mass transfer through the seafloor or the free surface ($\Gamma_{1/2} = \Gamma_{L+1/2} = 0$). Each layer is supplemented with the following divergence-free constraint $\mathcal{I}_\alpha = 0,\ \alpha \in \{1,2,\dots,L\}$, where

$$
\begin{gathered}
\mathcal{I}_\alpha = h\alpha \partial_x u_\alpha + 2\overline{w}_{\alpha+\frac{1}{2}} - 2w_\alpha, \\
\overline{w}_{\alpha+\frac{1}{2}} = \partial_t z_b + u_\alpha \partial_x z_{\alpha+1/2} - \sum_{\beta=1}^{\alpha} \partial_x \,(h_\beta u_\beta),
\end{gathered}
\tag{5}
$$

and the term $\partial_t z_b$ accounts for the movement of the bottom interface.

Note that the system is endorsed with extra dissipation accounting for friction with the bottom (τ_α^u), for viscous terms that model the shear stresses between the layers ($K_{\alpha\pm1/2}$), and for the breaking of the waves near the coast (τ_α^w). Here, we used the following dissipation models proposed by Macías et al. (2021a)
For the friction effects between the water and the seafloor, we used a standard Gauckler-Manning friction formula applied to the lowest layer

$$\tau_\alpha^u = \begin{cases} gLn^2|u_1|\dfrac{hu_1}{h^{4/3}}, & \alpha = 0 \\ 0, & \alpha \in \{2, \dots, L\} \end{cases} \tag{6}$$

We followed a simplified version of the model presented in Bonaventura et al. (2018) for the shear stress between the layers

$$K_{\alpha+1/2} = -\nu \frac{u_{\alpha+1} - u_\alpha}{(h_{\alpha+1} + h_\alpha)/2} \tag{7}$$

where ν is a constant kinematic viscosity, and $K_{1/2} = K_{L+1/2} = 0$.

For the breaking dissipation model, we considered here an extension of the simple, efficient, and robust model considered in Escalante et al. (2019) for a two-layer model:

$$\tau_\alpha^w = C\, w_\alpha\, |\partial_x(hu_\alpha)|, \quad \alpha \in \{1, \dots, L\} \tag{8}$$

The coefficient $C(x,t)$ defines breaking criteria to switch on/off the dissipation of the energy due to the presence of a breaking wave (e.g., Roeber et al., 2010). Here, we used

$$C = \begin{cases} 35\left(\dfrac{|\bar{u}|}{0.4\sqrt{gh}} - 1\right) & \text{if } |\bar{u}| > \sqrt{gh}, \\ 0 & \text{if } |\bar{u}| \le \sqrt{gh}. \end{cases} \tag{9}$$

The system in equations (3)-(5) satisfies an energy balance equation (Fernández-Nieto et al., 2018). The used modelling includes the non-hydrostatic ocean response and accurately captures dispersion and related effects during tsunami propagation and generation (Ma et al., 2012; Macías et al., 2021a, 2021b). Using a standard, Stokes-type, Fourier analysis for the linearized version of equations (3)-(5) around the water at rest steady-state, the phase, group velocities, and linear shoaling gradient are determined and compared with the Airy or Stokes linear theory for different numbers of layers (see Figure S2 in the Supporting Information, where relative errors are shown for the phase and group velocities, as well as for the shoaling gradient). One can prove uniform convergence for the analytical values when the number of layers increases (Fernández-Nieto et al. 2018).

A detailed description of the numerical discretization and implementation of this model, along with the comparison of results with standard benchmark problems, were presented in Text S1 and Text S2 of Supporting Information.

3 Numerical setup and the simulated dataset

The time-dependent vertical displacements caused by the dynamic rupture simulations are used as generation mechanism for the tsunami simulations. The displacement of the bathymetry and of the topography are both considered. The intersection between the fault and the free surface (the seafloor) coincides with the deepest point of the bathymetry and corresponds to the trench (see sketch in Figure 1a). The zero height of the bathymetry represents the initial sea level and positive values represent the topographic elevation of the coast. The sea surface elevation for all the grid points, both offshore and inland, is collected each 30 seconds. All the tsunami simulations last 2 hours.

One example of the dimensionless sea floor deformation at various times during one simulation is shown in Figure1(b). The distance from the trench is meant along the horizontal direction. It is worth to notice that the final static deformation (yellow curve in Figure 1b) might feature a lower maximum amplitude with respect to the transient deformation occurring previously (green curves in Figure 1b). This effect is due to the surface deformation induced by the trapped waves within the wedge as already shown by Oglesby et al. (2000) and Scala et al. (2019). A secondary vanishing deformation with a maximum amplitude of about 25% of the final static displacement, still due to the propagating seismic waves, triggers a tsunami wave propagating rightward from the trench ahead of the main wave.

Starting from a single dimensionless seismic rupture simulation, a broad range of different tsunami sources can be modelled. Exploiting the normalization presented in Section 2.1, we can vary the rigidity μ and the density ρ of the medium, the stress drop $\Delta\sigma$ of the earthquake and the characteristic slip weakening distance D_c, to obtain different durations, maximum amplitudes, and lateral extensions. The event size is then directly connected to the characteristic tsunami source wavelength.

The rigidity and the density are selected to cover a broad range of elastic properties which typically characterize the slab interfaces at the characteristic seismogenic depths, integrating values from reports released by Earthquake Research Promotion of Japanese Government (available at https://jishin.go.jp/main/chousa/17apr_chikakozo/model_concept-e.pdf, with densities extrapolated through Ludwig et al., 1970) and from several tomographic models for the Japanese slab (e.g. Takahashi et al., 2004; Yamada & Iwata, 2005; Miyake et al., 2008). The sampled rigidity, density values, the shear wave velocity $V_s = \sqrt{\mu/\rho}$ and the corresponding subduction layers, are reported in Table S1 of Supporting Information.

The stress drop values are sampled in a range between 0.2 and 30 MPa according to general observations about crustal, downdip interplate and tsunami earthquakes (Kanamori & Brodsky, 2004; Venkataraman & Kanamori, 2004; Bilek et al., 2016; Abercrombie et al., 2017; Folesky et al., 2021). Within this range, we selected 15 values such that their logarithms are equally spaced. A single characteristic slip weakening distance is selected ($D_c = 2\ m$) leading to a maximum slip $\delta u \sim 15\ m$ for the rupture dynamic simulations. This value is consistent with the one extrapolated for a $M_w = 9.0$ event according to the scaling law proposed by Skarlatoudis et al. (2016).

Combining all the sampled parameters, 345 different tsunami initial conditions could be set. However, most of them lead to either unrealistic or out of range of interest seismic source size.

The smallest rigidity values cannot be associated indeed with large stress drops and vice versa, to avoid modelling too small and too large earthquakes, respectively. Imposing a range of fault widths compatible with the expected value ($\pm 1\sigma$) of the scaling relations proposed by Strasser et al. (2010) for a magnitude interval $8.0 \leq M_w \leq 9.0$, we selected 81 out of the 345 combinations of parameters (See figure S9a and Table S2 in Supporting Information).
Each parameter combination leads to a characteristic source duration $\tau = \tau' \mu \mathrm{D_c}/(\Delta\sigma V_s)$ and to an along-dip source size $W = W' \mu D_c / \Delta\sigma$, with $\tau' = 17.1$ and $W' = 8.3$ representing the dimensionless duration and width computed through the dynamic rupture simulation. From τ and W values a proxy of rupture velocity V_r can be estimated (Figure S9b in Supporting Information). The rupture duration ranges between 25 s and 570 s, while $0.2km/s \leq V_r \leq 2.3km/s$, these values fitting the common observations for recent tsunamigenic earthquakes (Yoshimoto & Yamanaka, 2014; Ye et al., 2016). In the next section, all the results will be presented as a function of τ, W and the ratio $\tau/W \ \propto 1/\mathrm{V_s}$ that represents a size-normalized rupture duration and hence a measure of the characteristic rupture slowness. Some of the results will be presented as a function of $\lambda = W \cdot cos(dip) = W \cdot cos(20°)$ as indicated in Figure 1(a). This last quantity is the horizontal maximum extension of the seismic source and within this simple geometrical model represents a proxy of the characteristic wavelength of the source. The longest durations owe to small values of rigidity and stress drops, in turn deriving from shallow-depths rheological conditions, while the fastest sources are associated with large values of rigidity and stress drop, a more realistic condition for deeper events (Bilek & Lay, 1999; Geist & Bilek, 2001; Ebeling & Okal, 2012; Okal et al., 2016).Within this framework, the choice of a logarithmic scale for the stress drop along with the large number of models featuring small rigidity values (Table S2 in Supporting Information) allows us to more finely sample sources characterized by longer duration which are expected to mostly detach from the standard instantaneous source modelling.

We considered the time-dependent 3-layer non-hydrostatic model (hereinafter TD-NH) as the reference and we compared against it the simplified models (instantaneous source and shallow water, hereinafter IS and SW respectively). For the aim we simulated each initial condition 4 times (TD-NH, IS-NH, TD-SW and IS-SW). The IS were simulated imposing an instantaneous seafloor deformation equals to the final static displacement (as the yellow curve in Figure 1b). SW is simulated through a single layer hydrostatic approximation, and we used a Manning friction coefficient equal to 0.025. A constant Courant number equal to 0.9 is imposed. All these choices are justified by the performed tests, described in sections TextS1 and TextS2 in Supporting Information

The comparison is performed through three metrics: the wave amplitude η (sea surface elevation with respect to the still water level) and its maximum η_{max} at offshore gauges, the flow-depth D and its maximum D_{max} at onshore gauges (the water amplitude onto the topographic elevation) and the maximum run-up R_{max} that is the maximum topographic elevation reached by the tsunami during the inundation. For any metrics K we defined the discrepancy ΔK as the relative error due to the use of a simplified model:

$$\Delta K = \frac{K_{ref} - K_{simpl}}{K_{simpl}} \tag{10}$$

ΔK might assume negative values indicating that a simplified model produces an overestimation with respect to the reference one.

To investigate how much the results depend on the coupling between the tsunami and the oceanic and coastal morphology, the initial deformations are projected onto 6 different 1D topo-bathymetric profiles (colored lines on the map of Figure 1c). Each profile (blue lines in the insets around the map in Figure 1c) is extracted from the 30 arc-sec model SRTM30+ (https://topex.ucsd.edu/WWW_html/srtm30_plus.html) and then simplified to obtain piece-wise linear depth variations (colored profiles in the insets of Figure 1c) characterized by a planar scarp combined with either a planar or a segmented shelf towards and beyond the coast. This simplification allows to limit the effect of short size discontinuities and to provide general considerations about the effects depending on the large-scale geometrical features. The scarp slopes are quite similar to each other and are characterized by an average angle of 3.5° among the 6 profiles. Conversely, in the vicinity of the coast, the slopes are gentler in the southern part of the Tohoku region (Sendai and Fukushima areas), and steeper in the northern part (Iwate prefecture) with an intermediate behavior along the profile containing the nucleation area of the Tohoku earthquake. The mainland is modelled as a single slope. Most of the results presented in the next section will be obtained for the Tohoku nucleation area (red profile and bathymetry in Figure 1c) while a comparison between the different bathymetries is shown in section 4.3.

To ensure enough spatial resolution we performed a preliminary convergence test, running equivalent simulations on 6 grids characterized by different space sampling $\Delta x = [500m;\ 250m;\ 125m;\ 62{,}5m;\ 31{,}25m;\ 15{,}625m]$. We tested the discrepancy of each grid with respect to the finer one (assumed as a reference) computing the $\Delta_{\eta_{max}}$ offshore and the $\Delta_{D_{max}}$ on the coast similarly to eq. (**10**) but considering the module of the difference as numerator and the value on the finest grid as denominator. With this definition the Δ values represent the relative errors due to the use of a rougher grid. This analysis has been carried out extracting η_{max} and D_{max} at fixed gauge positions (regardless of the time at which these maxima are recorded) for two end-member initial conditions that is the largest size event (ID 1 in Table S2, $W = 275.3\ km$) and the smallest size one (ID 81 in Table S2 $W = 57.06\ km$) respectively. We retrieved $\Delta_{\eta_{max}} < 5\%$ everywhere and for both tests, already with rather rough grids (up to $\Delta x = 125\ m$ offshore and $\Delta x = 62.5\ m$ in the vicinity of the coast, Figures S10c and S10d in Supporting Information). However, $\Delta_{D_{max}}$ is below the threshold only for $\Delta x = 31{,}25\ m$ in the vicinity of the maximum run-up position at least for the smallest size simulations (see Figure S10a in Supporting Information). Since one of our aims is to model with enough accuracy the inundation features, including the maximum run-up, we finally used $\Delta x = 31{,}25\ m$ for the whole simulation dataset.

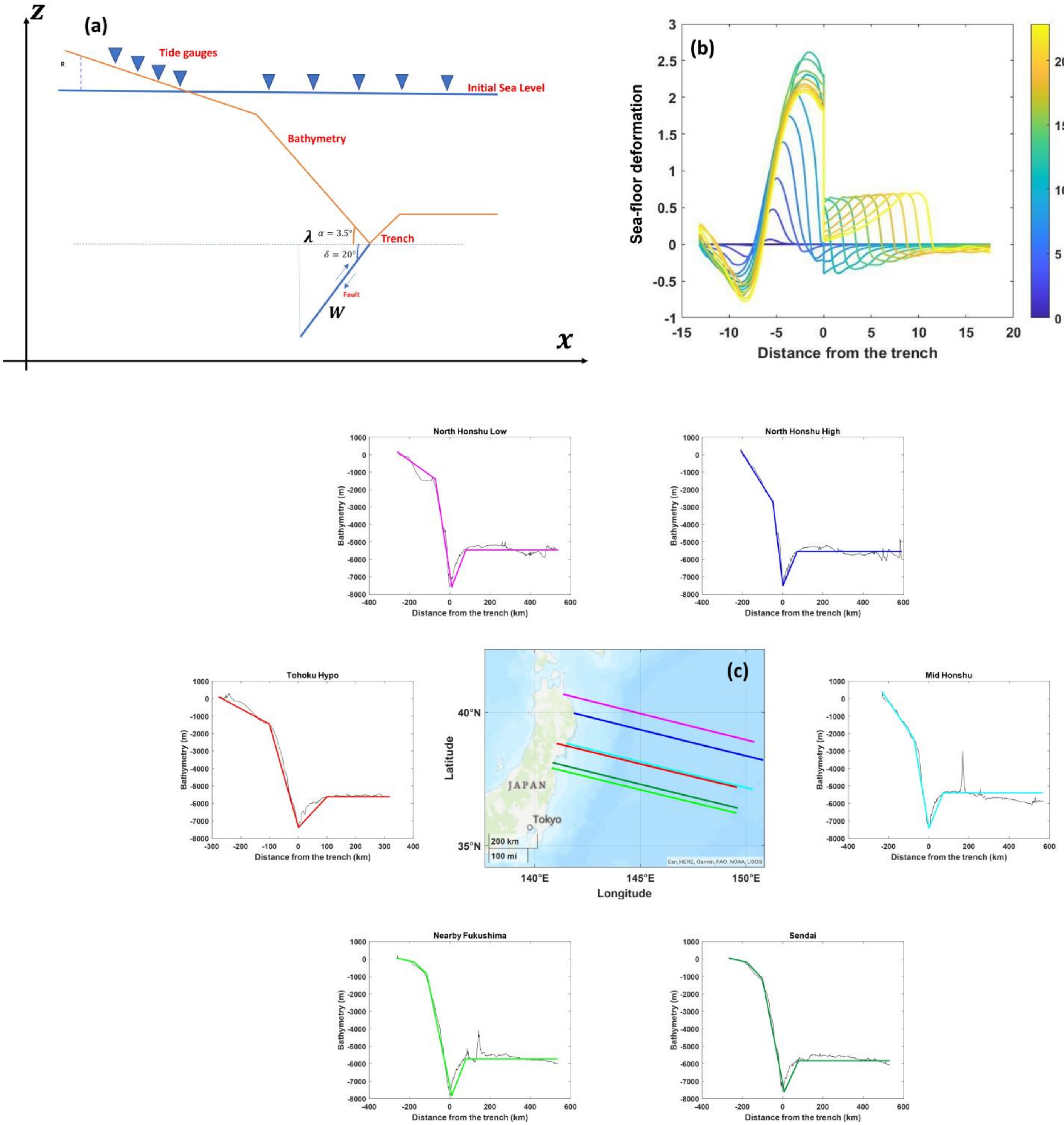

(a)
z
x
R
Tide gauges
Initial Sea Level
Bathymetry
Trench
λ
α = 3.5°
δ = 20°
Fault
W
(b)
Sea-floor deformation
Distance from the trench
Time
(c)
North Honshu Low
North Honshu High
Tohoku Hypo
Mid Honshu
Nearby Fukushima
Sendai
Bathymetry (m)
Distance from the trench (km)
Latitude
Longitude
JAPAN
Tokyo
200 km
100 mi
40°N
35°N
140°E
145°E
150°E
Esri, HERE, Garmin, FAO, NOAA, USGS

Figure 1: Schematic description of the simulation setup. (a) Sketch of the geometrical setup. The angle between the bathymetry (orange line) and the horizontal dashed line is exaggerated for sake of clarity. The blue triangles represent the gauges where the wave amplitude is computed both inland and offshore. W and λ represent the width on the fault and the horizontal extension of the surface deformation respectively. (b) Time dependent vertical topo-bathymetric deformation as a function of the distance from the trench. The time increases from blue to yellow curves with a final static deformation featuring a lower maximum with respect to the transient deformation occurring before. All the variables are plotted as dimensionless parameters. (c) Different modelled bathymetries. The modelled bathymetries are extracted from the 1D profiles in the map. Within the insets the bathymetry variation for each profile is plotted as a black line while the simplified geometry used in the simulations is plotted with the same color of correspondent profile in the map.

4 Results

4.1 Off-shore and coastal wave amplitude

Time-dependent VS instantaneous source

First, we show a qualitative comparison between the water waves generated by the non-hydrostatic time-dependent (TD-NH) and instantaneous sources (IS-NH). Figure 2 shows the wave amplitude as a function of the distance from the trench for two different initial conditions (simulations ID 31 and 11 are plotted on the left and right columns respectively, see Table S2 in Supporting Information) at different time steps and for both TD-NH and IS-NH. While the two simulations are characterized by the same τ/W value and hence by an equivalent dynamic evolution, the simulations on the right panels (Figures 2b-d-f) feature a large enough W (and τ) to generate coastal subsidence. For both simulations (small and large W), the TD sources feature a larger maximum wave amplitude than the corresponding IS, and the maxima occurs at various times, as an effect of the different duration of the transient. However, this transient is rapidly attenuated during the landward propagation outside of the source region, and, starting from a certain time, the IS systematically features larger η_{max} with respect to the TD simulation (Figures 2e and 2f). Conversely, towards the open sea, rightward from the trench, we retrieve the opposite behavior with the TD source leading to larger yet delayed maximum η as an effect of the directivity (the seaward motion of the upper plate).

Regardless of the source temporal features (TD vs IS), the main difference between simulations with small and large W emerges while the waves are approaching the coast. For small W , such that λ is smaller than half distance between trench and the coast, (Figures 2a-c-e), the wave shoals. For larger ruptures (Figures 2b-d-f), the instantaneous sea drawback limits the shoaling and thus the amplification of the wave close to the coast as can be spotted by comparing Figures 2e and 2f.

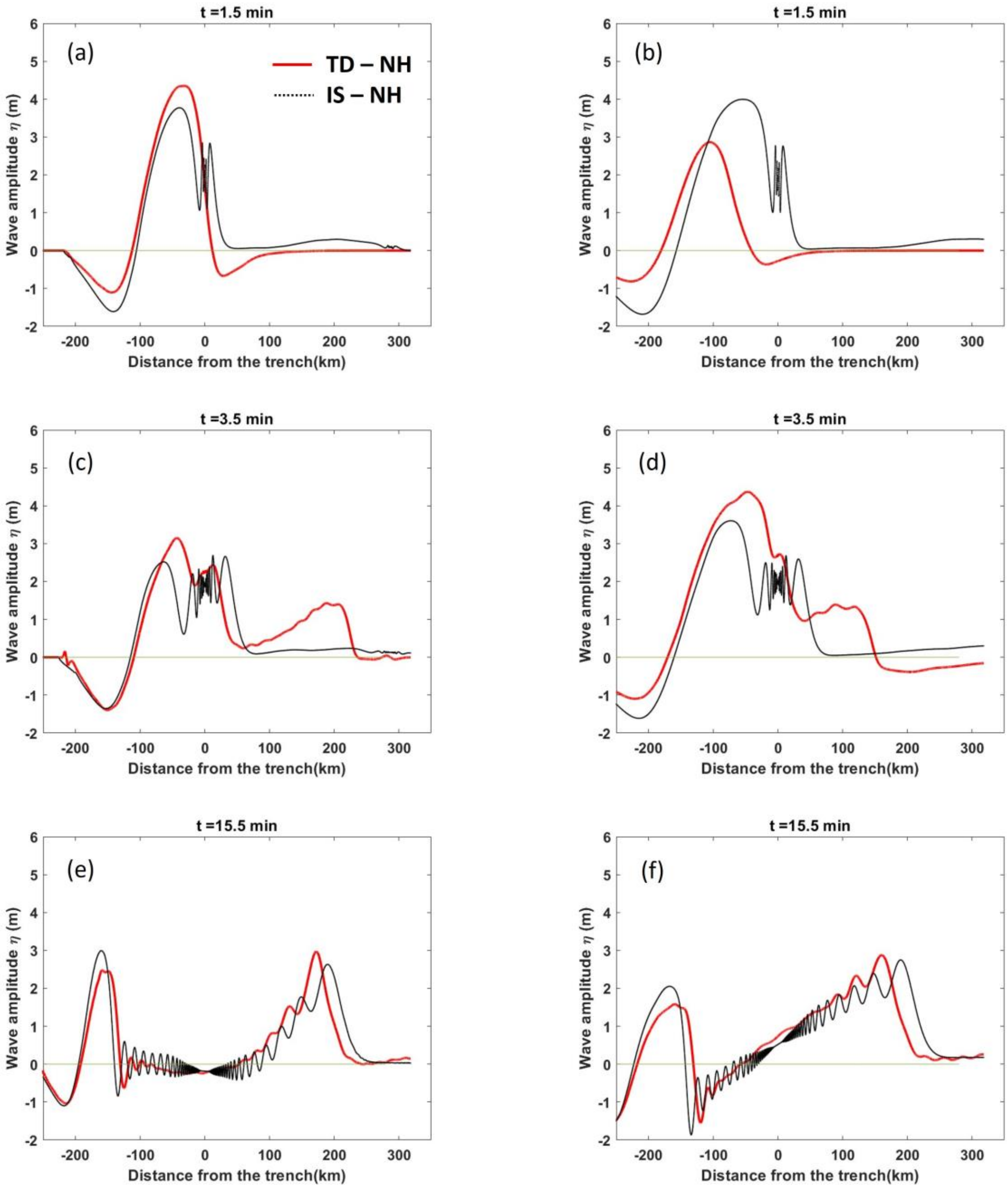

Figure 2: Wave amplitude as a function of the distance from the trench for TD – NH (red curves) and IS – NH (black dotted lines) at three different time steps and for two simulations: the ID 31 (left panels) and the ID 11 (right panels) in Table S2 in Supporting Information. These simulations represent examples of small and large-size sources, respectively. The whole evolution can be found in the Supporting Information (Movies S1 and S2).

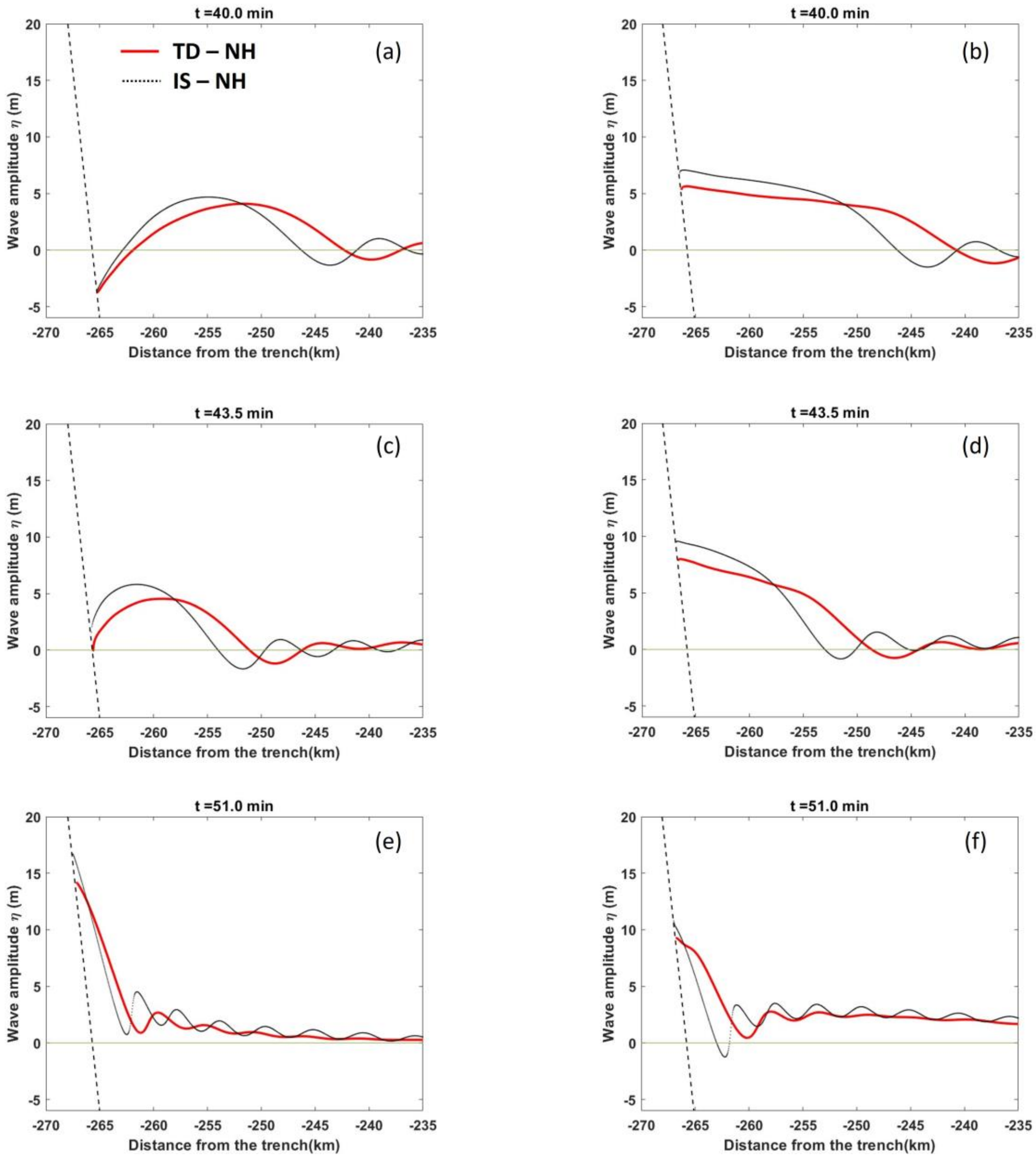

Figure 3: Wave amplitudes, zoomed around the coast, as a function of the distance from the trench for TD – NH (red curves) and IS – NH (black dotted lines) at three different time steps and for two simulations: the ID 31 (left panels) and the ID 11 (right panels) in Table S2 of Supporting Information. These simulations represent examples of small and large size sources respectively. The short-dashed line on the left represents the coastline within each panel. The whole evolution can be found in the Supporting Information (Movies S3 and S4).

This difference is evident also by zooming around the coastline (Figure 3) at a later stage ($t > 40\text{min}$). From this close-by view, it can also be seen that the inundation begins earlier for rupture with large W (Figure 3b), when for the small W simulation, the tsunami is still in the shoaling phase (Figure 3a). When the large source simulation has almost reached its maximum (Figure 3d), the inundation for the smaller source starts (Figure 3c), reaching in the end a maximum run-up that is about 1.5 times the one for the large W, for both IS and TD sources. This is a direct consequence of the potential energy accumulation during the shoaling process (Figures 3e and 3f). However, independently of the size and duration of the TD source, approximating it with an instantaneous source always results in a larger inundation both in terms of flow-depth D and maximum run-up R_{max}.

To systematically quantify the discrepancy between the IS and TD sources, we investigated the variability of $\Delta_{D_{max}}$ at the points on the coast (eq. (**10**)), as a function of τ/W (horizontal axis) and λ (different colors) for all the 81 simulations (see section 3 and Table S2 in Supporting Information). In Figure 4 the results for the first point on the coast are summarized. We observed that the IS source systematically overestimates the flow-depth ($\Delta_{D_{max}}$ values are always negative, Figure 4a). The slower the TD rupture, the larger the discrepancy with the correspondent IS simulation. A second trend depending on the source extension emerges, as for fixed τ/W, larger ruptures lead to larger discrepancies. A comparison between the time histories of the flow-depths at the first point on the coast is shown in Figure 4b, for the simulations inside the dashed rectangle in Figure 4a. The four simulations are characterized by the same source dynamic time scale, that is τ/W, with the larger extension due to a larger stress drop $\Delta\sigma$. The flow-depth amplitude D_{max} increases with λ until a maximum value (cyan curves in Fig. 4b) with an overestimation between 3% and 7% due to the instantaneous modelling. For larger λ, D_{max} decreases featuring larger overestimations up to about 14%. This overestimation is particularly significant for the largest λ values, because the inundation directly relates with source time history which becomes dominant given the virtual absence of landward propagation and shoaling. We have verified that comparable results hold when a SW propagation modelling is used, which is important because the most commonly adopted approximation is the SW-IS approach (Figure S11 of Supporting Information).

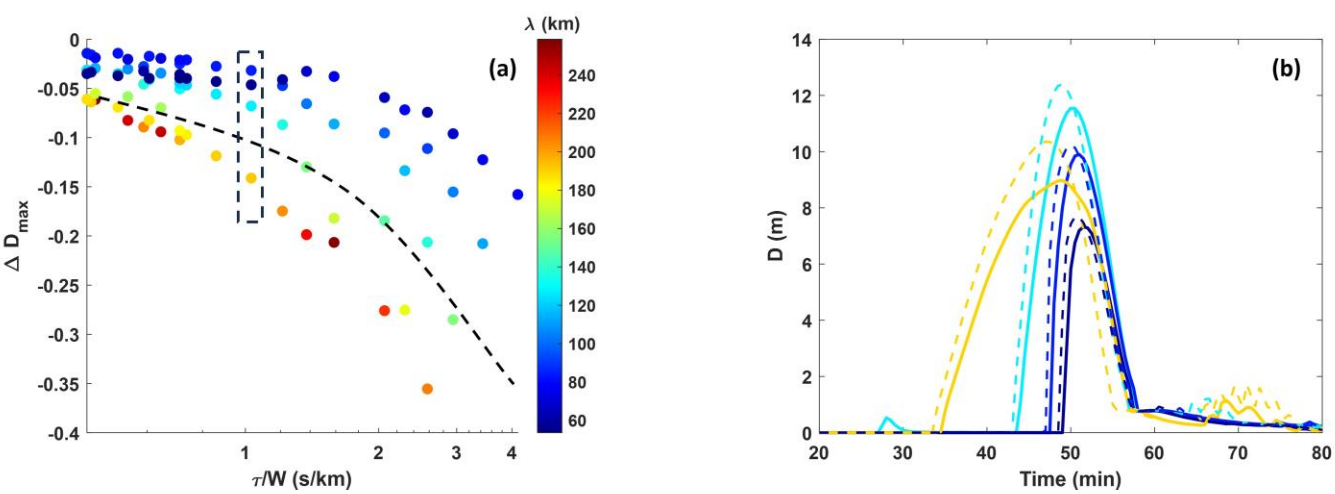

Figure 4: Relative discrepancy between time-dependent (TD-NH) and instantaneous source (IS-NH) results in terms of flow-depth at the first point on the coast (a) ΔD_{max} at the first point on the coast as a function of τ/W with color scale marking the source horizontal extension λ**.** The black dashed line separates the two highlighted trends for small and large ruptures. (b) Flow-depth as a

function of time for the four simulations within the black-dashed rectangle in panel (a) plotted with the same colors. In panel (b) TD and IS sources are represented through solid and dashed lines respectively.

Non-hydrostatic VS Shallow Water propagation

To perform a systematic comparison between the accuracies of NH and SW propagation schemes in modelling a tsunami generated by a TD seismic source, we run a set of SW propagation simulations of tsunamis triggered by the same seismic TD source as used in the NH simulations described in the previous section.

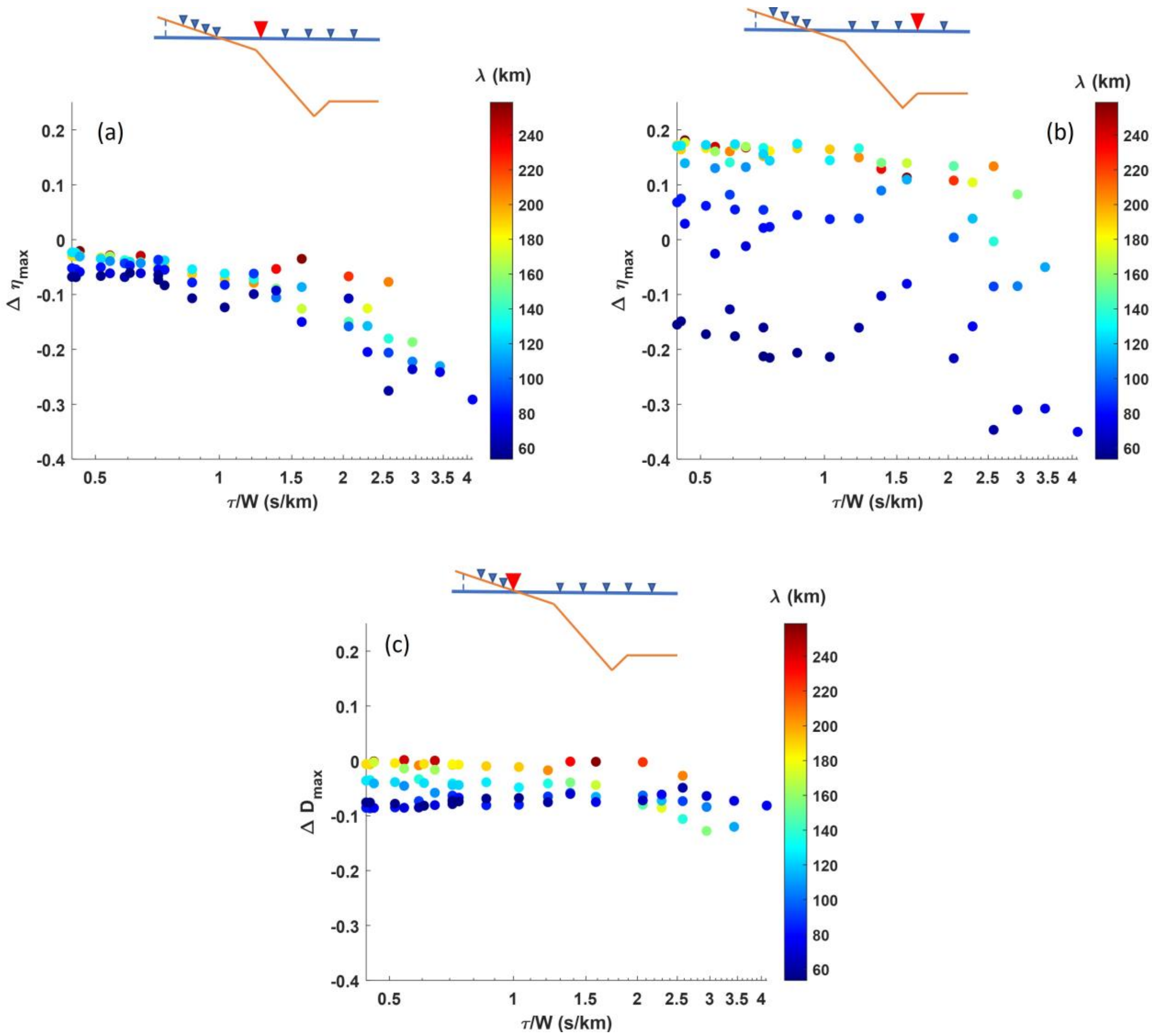

Figure 5**:** Relative discrepancy between Non-Hydrostatic (NH) and Shallow Water (SW) results when TD sources are used for both propagation regime. (a) $\Delta\eta_{max}$ at a gauge placed along the coastward propagation as a function of τ/W with color scale marking the source horizontal extension λ. (b) $\Delta\eta_{max}$ at a gauge placed rightward beyond the trench as a function of τ/W with color scale marking the source horizontal extension λ. (c) ΔD_{max} at the first point on coast as a function of τ/W with color scale marking the source horizontal extension λ. For sake of comparison the figures are plotted with the same scale. A sketch of the position of points where the Δ are computed is plotted within each panel.

Figures 5(a) and (b) show the $\Delta\eta_{max}$ for two gauges located between the source and the coast and beyond the trench respectively, while in Figure 5(c) the ΔD_{max} is shown for the first point on the coast. Even though for the smallest modelled source, λ is more than 7 times larger than the maximum sea-floor depth, and hence the SW limit is quite far to be violated (Abrahams et al. 2023), significant $\Delta_{\eta_{max}}$ with negative values down to -30% occurs, indicating that SW systematically overestimates the NH wave amplitude during the coastward propagation (Figure 5a). For the slowest and smallest ruptures, the $\left|\Delta_{\eta_{max}}\right|$ is enhanced as an effect of short wavelength oscillations affecting both the primary and the secondary waves. Such oscillations are due to coupling of the dynamic evolution of the source with the instantaneous dissipative shock introduced by the SW propagation (See wave evolution in left panels of Figure S12 in Supporting Information).

For smaller ruptures, a similar SW overestimation is retrieved also in the open ocean propagation beyond the trench, while a systematic underestimation emerges at intermediate and large source sizes λ as shown in Figure 5(b).

However, such differences affect to a lesser extent the flow-depth maximum amplitude on the coastal points with only few very slow simulations featuring a $|\Delta D_{max}|$ slightly larger than 0.1, as evidenced in Figure 5(c) for the slowest ruptures.

Modelling NH and SW regimes with IS instead significantly reduces $\left|\Delta_{\eta_{max}}\right|$ offshore (Figures S13a and b in Supporting Information) and $|\Delta D_{max}|$ on the coast (Figure S13c) for small source size λ, while the SW underestimation for intermediate and large λ values, beyond the trench, is characterized by similar $\Delta_{\eta_{max}}$. Despite in this condition the maximum amplitude metrics being overall convergent, an interesting feature emerges following the waveform evolution with time for the secondary waves. Indeed, when an instantaneous source is modelled, the NH propagation generates high-frequency oscillations behind the primary wave possibly hampering the correct modelling of secondary waves eventually generated by the dispersive propagation regime (Figure S14 in Supporting Information). In other words, in case of instantaneous ruptures with strong gradients, a singularity is generated on seafloor. The propagation of such a singularity generates a train of secondary waves that propagates overlapping to the dispersive waves. Such effect has been confirmed by laboratory experiment and convergence tests, performed with a refined grid and modelling 5 and 7 non-hydrostatic layers.

4.2 Inundation and maximum run-up

To address how the modelling approximations affect the inundation we used the maximum run-up R_{max} and $\Delta_{R_{max}}$ as metrics. We performed similar comparisons as for the amplitude, first between the TD-NH and IS-NH, and then between TD-SW and TD-NH. We show the results also for IS-SW.

Figure 6(a) shows the ΔR_{max} for IS-NH taking TD-NH as a reference, as a function of τ/W and λ. A trend similar to the one shown in Figure 4(a) is observed, with an increasing discrepancy for slower and larger ruptures. However, the largest ruptures generate significantly smaller values of both R_{max} and $\Delta_{R_{max}}$ as a consequence of the significant subsidence that completely prevents the shoaling limiting the run-up. When the same comparison is performed between TD-NH and TD-SW, we retrieved smaller discrepancies with maximum values of $\Delta_{R_{max}}$ around the 16% for the smallest modelled sources (Figure 6b). A negligible contribution to the discrepancy is associated to the parameter τ/W, which emerges only for very slow ruptures ($\tau/W > 3$ s/km)

The absolute R_{max} behavior for all the 81 simulations and for the 4 models is summarized in Figure 6(c) evidencing a resonant character as a function of λ. The resonance is pretty perfect for IS cases, with an optimal amplification for a narrow λ range, around 100-120 km. For TD sources, both for SW and NH, R_{max} is also influenced by the source duration leading to a scattered R_{max} pattern against λ still following the resonant trend. The λ value for which the resonance is observed depends on the specific costal slope, as will be illustrated in Section 4.3.

Focusing on the discrepancies for SW simulations we also highlight that: i) the rupture size for which the resonance is observed is independent of the propagation regime; ii) the overall SW overestimation holds even when the more realistic TD-NH and TD-SW are compared. However, in Figure 6(d), we observe that while with an IS the SW versus NH, ΔR_{max} is always less than 10%, it becomes larger with a TD source, with a maximum of about 16%. Looking at the time evolution of inundation (Figure S15 in Supporting Information), we confirmed that the largest ΔR_{max} emerging for small λ in TD simulations are actually due to the short-wavelength oscillations (left panels of Figure S15 in Supporting Information). These oscillations are attenuated for larger ruptures (Figure S15 of Supporting Information, right panels) and suppressed for IS simulations (black dotted lines in Figure S14)

To summarize, as expected in realistic conditions for large subduction earthquakes, with $\lambda \gg H$, the difference between NH and SW models are definitely less significant than the discrepancy emerging between IS and TD simulations, at least in terms of wave maximum amplitude and maximum run-up. However, the SW overestimation increases for very slow ruptures leading to $|\Delta| \sim 20\%$ for the investigated metrics. In terms of waveform features, as seen, the use of either a SW model for a TD source or a NH regime for instantaneous seafloor deformation causes short wavelength oscillations affecting both the smaller oscillations behind the primary wave and, sometimes, the inundation metrics, at least for $\lambda < \lambda_R$ with λ_R being the resonance wavelength described in Figure 6(c).

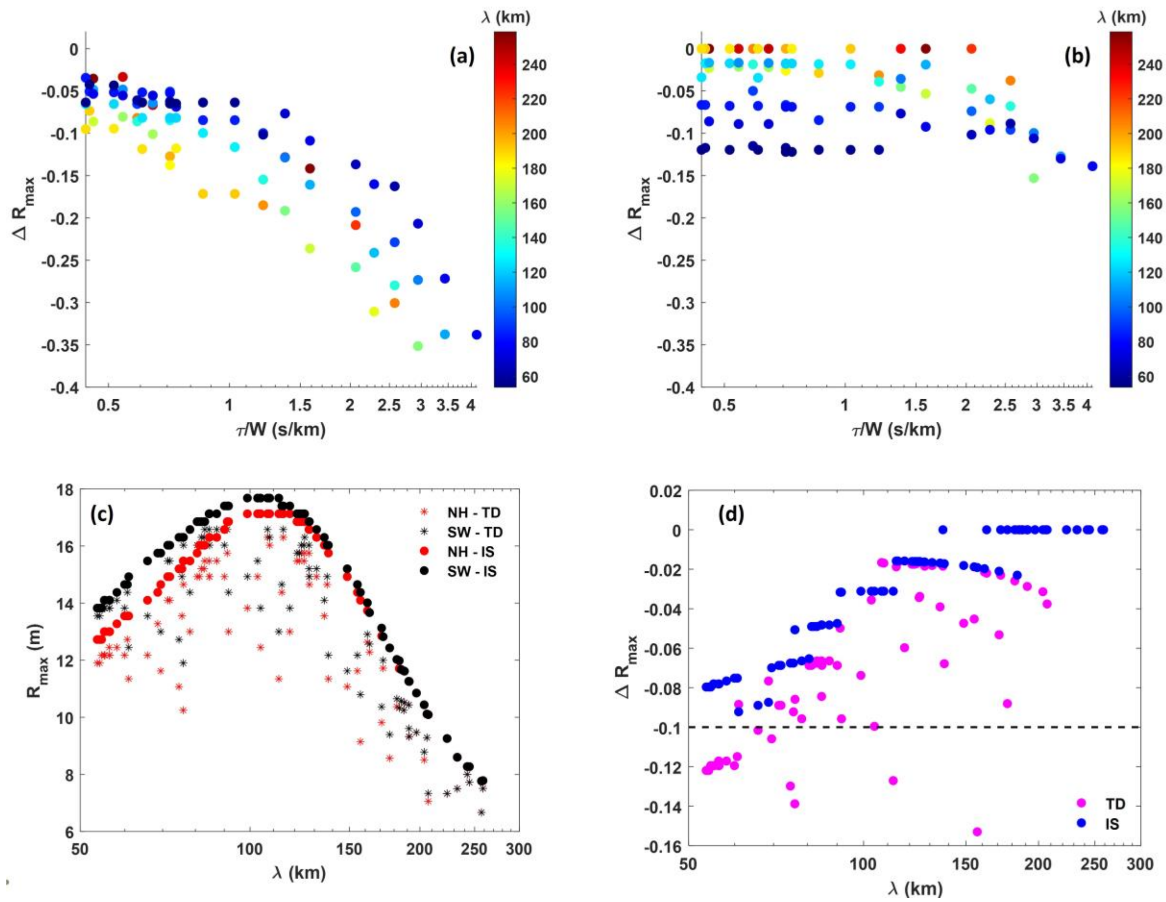

Figure 6: Maximum run-up R_{max} comparison between the four different models (TD-NH, IS-NH, TD-SW, IS-SW). (a) ΔR_{max} between TD-NH and IS-NH as a function of τ/W with color scale marking the source horizontal extension λ. (b) ΔR_{max} between TD-NH and TD-SW as a function of τ/W with color scale marking the source horizontal extension λ. For sake of comparison, the Figures in panels (a) and (b) are plotted with the same scale. (c) R_{max} on the coast as a function of λ for the four different models (d) ΔR_{max} as a function of λ with blue and magenta dots referring to IS-NH vs IS-SW and TD-NH Vs TD-SW comparison, respectively. The dashed line indicates that only for TD sources some simulations feature $|\Delta R_{max}| > 0.10$

4.3 Effect of bathymetry

To investigate the effect of different bathymetric conditions, particularly as far as the run-up resonance is concerned, we repeated the complete set of simulations for the other 5 simplified topo-bathymetric profiles (Figure 1c). While the 6 different bathymetries are similar in the deep part, they mostly differ in the slope at shallower depth in the vicinity of the coast and inland. Since some bathymetric profiles are similar, in Figure 7(a) we only show the results for three of them. The results shown so far were retrieved for the profile referred to as "Tohoku Hypo" (Figure 1c). The southernmost profile referred to as "Sendai" is characterized by a significantly flatter slope, while "North Honshu High" by a steeper slope in the vicinity of the coast. These three profiles are interpreted as a proxy of the overall behavior in presence of intermediate, flat and steep topo-bathymetric profiles, respectively.

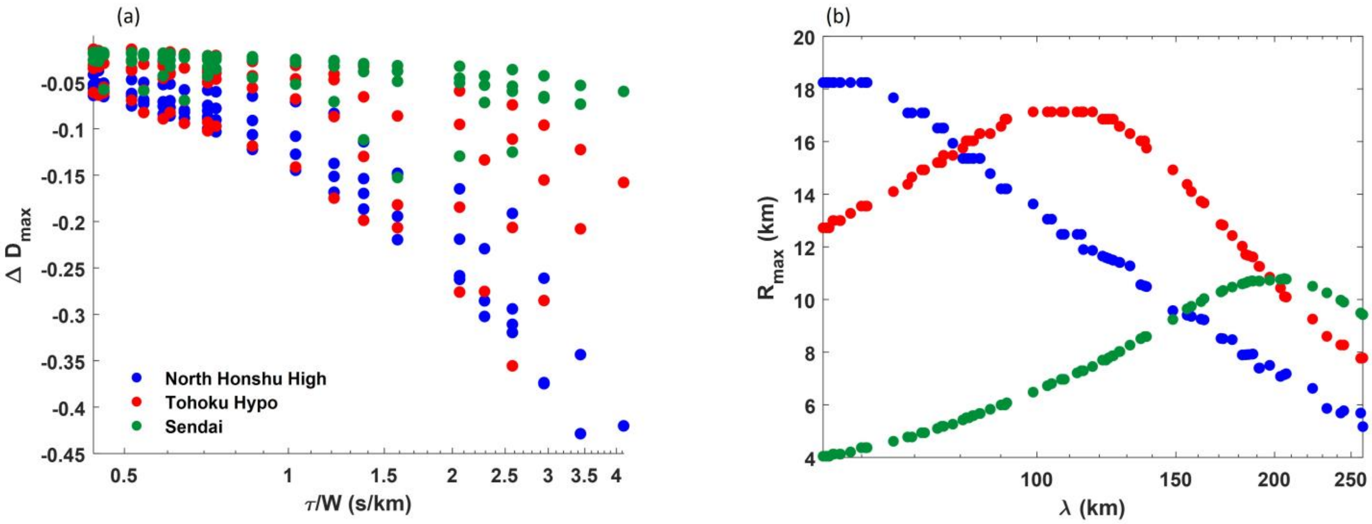

Figure 7: Inundation metrics for different bathymetric geometry. (a) ΔD_{max} (TD-NH vs IS-NH) at the first point on the coast for the profiles referred to as "North Honshu High", "Tohoku Hypo" and "Sendai" respectively according to the map in Figure 1(c). (b) maximum run-up R_{max} (for IS-NH case) as a function of horizontal source extension λ for the 3 bathymetric profiles following the same legend of panel (a).

Figure 7(a) shows the $|\Delta D_{max}|$ between IS-NH and TD-NH source simulations at the first point on the coast, for all the simulations and for the 3 different profiles. We retrieved for all the bathymetries the double trend evidenced in Section 3.1 with larger discrepancy emerging not only for slower ruptures but also for large size sources. However, a flatter bathymetry leads to smaller $|\Delta D_{max}|$ implying that when a tsunami wave propagates towards more gentle depth variation an instantaneous source would produce inundation scenarios more similar to time-dependent sources as compared to steeper environments. Contemporarily, in a flatter environment, the inundation is attenuated both in terms of flow-depth on the coast and maximum run-up with the size of resonance that increases as the bathymetry slope decreases (see Figure 7b). For the sake of clarity, this latter panel only shows the trends for the IS-NH case. However, we verified that, for all the bathymetries, the rupture size for which the resonance occurs is independent of both the source treatment (IS or TD) and the choice of propagation regime (NH or SW, compared with Figure 6c).
In conclusion, a gentler slope of the coast, as in the case of the flood plains in the area of Sendai-Fukushima selects a longer wavelength component of tsunami waves, generating less intense inundations in terms of both flow-depth on the coast and maximum run-up. Moreover, in a

Tohoku-like environment, like the one we have modelled in this study, the longer wavelengths are more controlled by the deformation occurring very close to the hypocenter (Satake et al., 2013). This contributes to reduce the discrepancy between IS and TD simulations for the flatter bathymetric profiles.

5 Discussion

5.1 Comparison with real earthquakes and tsunamis

To understand in which cases time dependent and/or non-hydrostatic effects should be considered, the 81 simulations performed for the "Tohoku Hypo" bathymetry (intermediate slope) are plotted in Figure 8(a) as a function of their source slowness τ/W and size λ. They are classified depending on whether the parameter ΔR_{max} (TD-NH vs IS-NH) is larger (red dots) or smaller (orange and green dots) than 0.1, considering as acceptable a relative discrepancy smaller than 10%. The source slowness and size are related to seismic parameters like the stress drop, the average rigidity and hence the average depth of the source (Bilek & Lay, 1999; Geist & Bilek, 2001; Sallarès & Ranero, 2019). As expected, the slower the rupture the more time-dependent rupture modelling is needed. The instantaneous approximation tends to fail when the characteristic tsunami propagation speed at the source, on the order of $\sqrt{gH_{trench}}$ (with H_{trench} being the depth at the trench) is comparable with the rupture velocity V_r, for which the quantity $(\tau/W)^{-1}$ acts as a proxy (e.g. see Abrahams et al., 2023), as it occurs for the slowest ruptures considered here. However, beyond that, we found that the ΔR_{max} (TD-NH vs IS-NH) also depends on the source size. Indeed, larger ruptures, for which along-dip distance is comparable with trench-coast distance, more likely lead to inaccurate solutions from approximated models. In these cases, the inundation is more controlled by what happens at the source rather than by the propagation processes (e.g., the shoaling).
To provide modelers with tangible recommendations, we compared the parameters of the sources presented in Figure 8(a) with those inferred for some subduction interface tsunamigenic earthquakes . Their features are summarized in Table S3 of Supporting Information. We extracted the duration τ, the width W and the dip angle from the teleseismic data inversions by Ye et al. (2016), for all the events, including the Maule 2010 Mw 8.8 and the Tohoku-Oki 2011 Mw 9.1 earthquakes, with the exception of the 2004 Sumatra-Andaman earthquake, whose parameters are taken from the finite-fault model summary released by USGS (https://earthquake.usgs.gov/earthquakes/eventpage/official20041226005853450_30/finite-fault, Banerjee et al. 2007). We computed a proxy of the source size along the dip as $\lambda = W \cdot \cos\delta$, with δ being the dip angle (See Table S3 in Supporting Information). Such a comparison in Figure 8 has the goal of comparing the characteristic space and time scales of simulations with those of the real events. However, single real events might be also affected by specific conditions related to local geometry, shallow structure, bathymetry variation, and ratio between source size and trench-coast distance as it happens for the Maule 2010 earthquake (Romano et al., 2020), which may differ from the Tohoku-like setup used in our 1D simulations. Hence, this comparison should be regarded as a general indication. Nonetheless, according to this comparison, some of the megathrust events, characterized by relatively shallow slip and not too high stress-drop, such as Maule 2010 and Tohoku 2011, are very close to the accuracy limit to use an instantaneous source, while the 2004 Sumatra-Andaman event is well in the region where instantaneous source modelling leads to inaccurate solutions and a time-dependent source should be used. The use of a TD source implies, in turn, the necessity of a NH regime to avoid the spurious oscillations shown

in Figures S12 and S15 (in Supporting Information) and the consequent systematic SW overestimation evidenced in Figures 6(c) and 6(d).
Conversely, large stress drop events (relatively rapid ones, sometimes referred to as “snappy” earthquakes, see e.g. Ebeling & Okal, 2012; Okal et al., 2016) can be well modelled with an instantaneous source. Finally, earthquakes featuring a small extension along the dip, might lead to larger errors when modelled by an instantaneous source, if they are characterized by very slow ruptures, like the tsunami earthquakes (small values of stress drop and rigidity). However, a direct comparison between the findings of this study and tsunami earthquakes must be interpreted with some prudence, since such events are characterized by a quite large along-strike extension as compared to their width (Kanamori, 1971; Tanioka & Satake, 1996a; Tanioka & Seno, 2001). Such a feature cannot be considered in the 1D model and will be the scope of future work.
Lastly, In Figure 8(a) the orange dots represent the simulations for which ΔR_{max} (TD-NH vs IS-NH) < 0.1 while ΔR_{max} (TD-NH vs TD-SW) > 0.1. Such simulations are characterized by a small source extension ($\lambda \sim 7 H_{trench}$) and, although they could be modelled through an IS description, they require a NH modelling to avoid exceeding the imposed discrepancy tolerance. Within this region we retrieve very short-sized interslab events like the 2009 Papua event or the Tohoku foreshock of 2011, March 9th. In such a case, even if metrics like the maximum run-up are accurately modelled through an IS approach, a TD source must be used to prevent the short wavelength oscillations affecting the dispersive secondary waves (See red curves in Figure S14 in Supporting Information). For the same reason, for faster events (e.g. deeper, larger stress drop earthquakes for which $\sqrt{gH} \cdot \tau / W \ll 1$), that can be precisely simulated with an IS, the choice of a SW modelling represents a preferable option (see green regions in Figure 8).

We have verified that ΔD_{max} or ΔR_{max} depend also on topographic features (see Figure 7a). Figure 8(b) shows the same plot as Figure 8(a) with the ΔR_{max} values, but using the flatter “Sendai” near-coast bathymetry and topography. As shown in Figure 7(a), the ΔD_{max} values on the coast are smaller for flatter bathymetries and this leads to smaller Δ values also in terms of maximum run-up. As a consequence, only very slow ($V_r < 0.5\ km/s$) and large ruptures (λ larger than half trench-coast distance) yield inaccurate inundation modelling when an IS source is used as a tsunami generation mechanism. Only the modelling of events similar to the giant 2004 Sumatra event would require a TD source. The differences highlighted between Figures 8(a) and (b) are consistent with the results related to the 2011 Tohoku-Oki event, by Satake et al. (2013) who showed how a time-dependent source modelling is required to accurately retrieve the inundation features along the coast in front of the hypocenter of the event. Satake et al., (2013) also showed that an instantaneous source was enough to model a realistic inundation in the southern regions of Sendai and Fukushima. For flatter bathymetries, for which the shortest wavelength sources generate negligible inundations, all the ΔR_{max} (TD-NH-vs TD-SW) values are below the imposed tolerance of 0.1. For the sake of completeness, the results summarized in Figure 8 are compared with the condition $W/\tau = 2\sqrt{gH_{trench}}$ that represents a proxy of the instantaneous source limit (Abrahams et al., 2023). An equivalent horizontal line fixing as a reference a SW limit $\lambda = 2H_{trench}$ would be well below the shortest modelled source.

At least for a Tohoku-like up-dip rupture, using an instantaneous source always overestimates the inundation on the coast as compared to the corresponding time dependent modelling. Therefore, for some applications, the IS can be still used as a conservative approach, even though relatively inaccurate, if a kinematic or a dynamic realistic description of the seismic source process is not available. Nevertheless, we have also verified that for some simulations the maximum amplitude of waves propagating towards the open ocean along the directive direction is underestimated by the IS modelling. This might produce an underestimated inundation warning towards those islands which are located along the up-dip direction, in the vicinity of the trench.

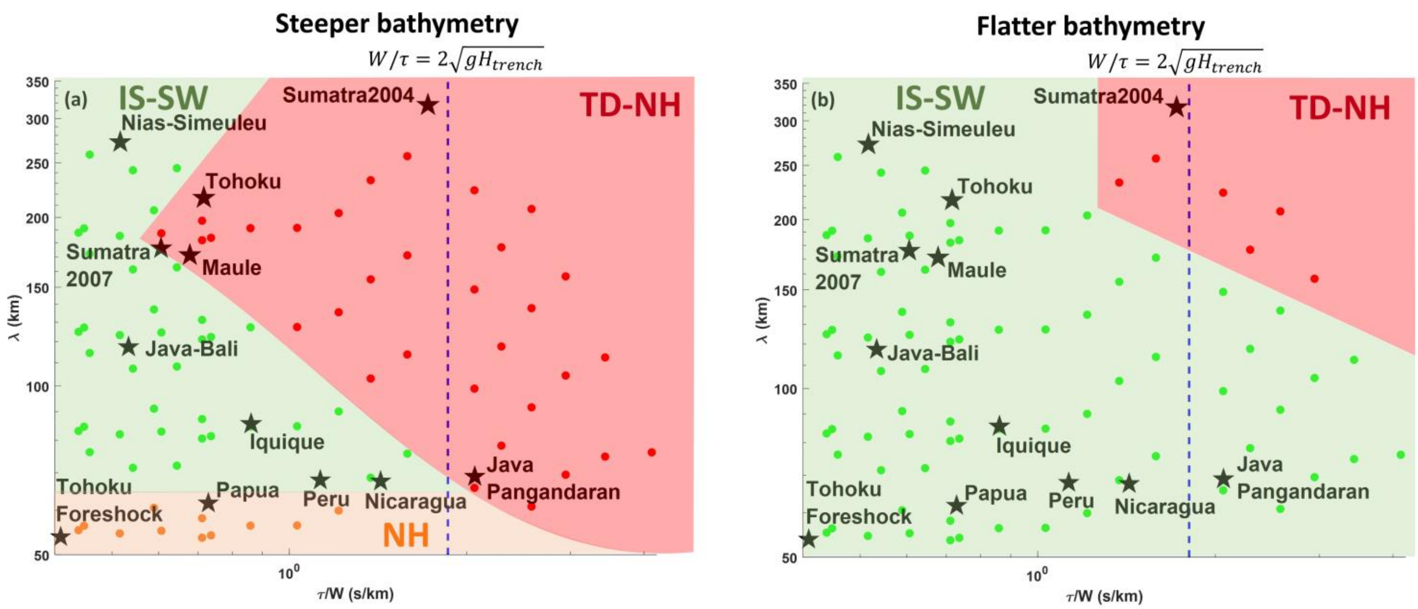

Figure 8: Summary of simulations that can be modelled with (green dots) and without (red and orange dots) enough accuracy using simplified models in terms of maximum run-up R. In all panels, each simulation is placed according to τ/W and λ with the green and red dots representing $|\Delta R_{max}| \leq 0.1$ and $|\Delta R_{max}| > 0.1$ respectively when the comparison (TD-NH vs IS-NH) is performed. Orange dots represent the simulations for which ΔR_{max} (TD-NH vs IS-NH) < 0.1 while ΔR_{max} (TD-NH vs TD-SW) > 0.1 The colored regions indicate the regions where different models must be used. The blue dashed lines border the regions where the seismic rupture velocity proxy W/τ is equal to 2 times the maximum tsunami velocity at the source $\sqrt{gH_{trench}}$. Panels (a) and (b) refer to simulations performed on an intermediate slope ("Tohoku Hypo") and flat slope bathymetry geometry ("Sendai"), respectively.

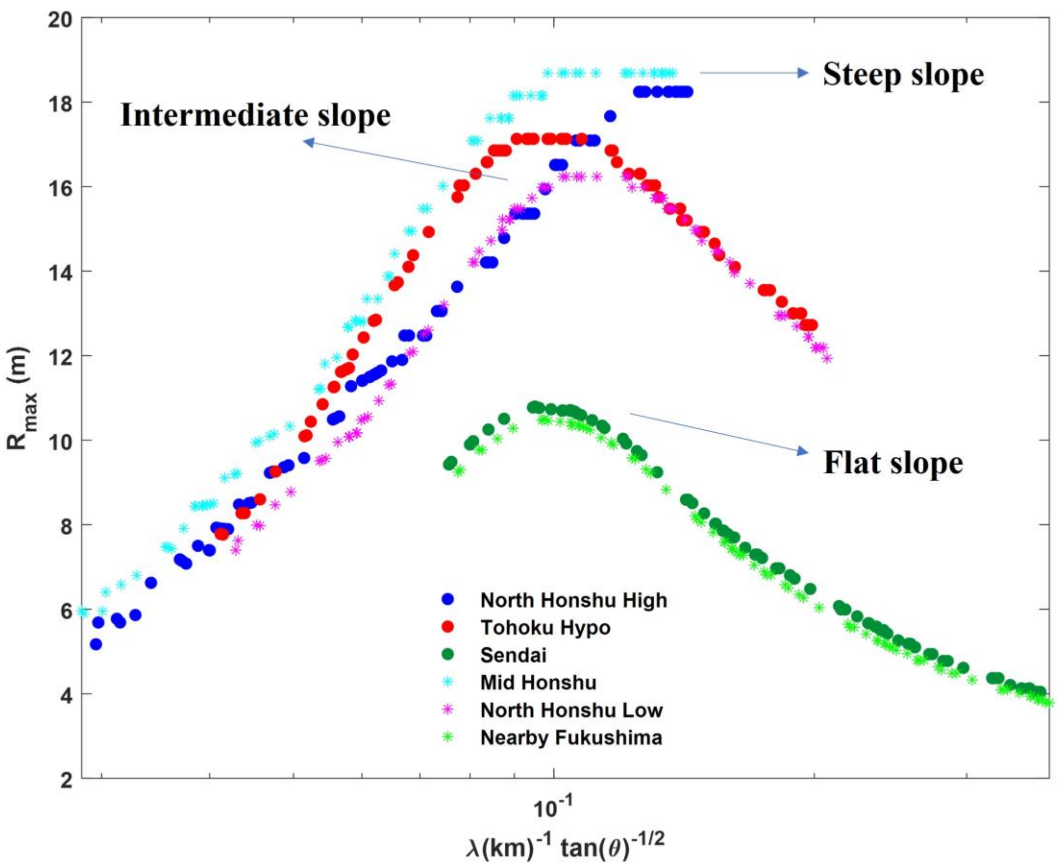

Figure 9: maximum run-up as a function of $1/(\lambda\sqrt{\tan\theta})$ as suggested by the model of Stefanakis et al. (2012). As indicated by the arrows the blue dots and cyan stars refer to steeper slope geometry, the red dots and magenta stars to intermediate slope and the dark green dots and green stars to flatter slope bathymetry, respectively, as reported in the legend.

5.2 Resonance

Another important result concerns the size of the resonance observed in the computation of maximum run-up and its connection to the geometry of bathymetric profiles. In this framework, Stefanakis et al. (2012) have shown how a monochromatic source, with pulsation ω, generates resonant waves whose maximum run-up on planar beaches depends on the incident wavelength and beach slope (with larger run-ups associated with steeper slopes). They verified that for a fixed beach length L the resonance is always retrieved at the same normalized pulsation $\omega' = \omega/\sqrt{g\tan\theta/L}$, with g and θ being the gravity acceleration and the slope of the bathymetry (in the vicinity of the beach and inland), respectively. To verify the consistency of the same model for our application, we can replace ω with $1/\lambda$ since in the vicinity of the source the depth variation and hence the propagation velocity are the same for all the bathymetries. Moreover, we can neglect the effect of L because the beaches are always long enough to avoid backward reflections. Figure 9 shows the maximum run-up R_{max} for all the 81 IS-NH simulations and the 6 bathymetries, as a function of the parameter $1/\left(\lambda\sqrt{\tan\theta}\right)$, θ being the different slopes of the bathymetry in the vicinity and on the coast. Although the sources modelled in this work are quite different as compared to the simplified monochromatic source, with characteristic wavelength inherited by a realistic parameterization of the seismic rupture, the resonant mechanism is preserved (compare Figure 9 with Figure 7c) at least for instantaneous sources. When a TD source is implemented this resonance symmetry is partially smeared since the maximum run-up is also controlled by the seismic source duration (See Figure 6c), with slower ruptures leading to smaller inundation. This latter result challenges the common assumption, for example, for tsunami earthquakes, that slow ruptures are one of the reasons why larger than expected tsunami inundation for a given earthquake magnitude is observed. Nevertheless, our modelling indicates that the inundation amplification could still be due to larger slip occurring at shallower depths, where the surrounding medium is weaker, and/or eventually to an unexpectedly large extension of the rupture along the strike direction.

5.3 Limits of numerical modelling

Some of the choices made in terms of seismic source parameters deserve further discussion since they can affect the investigated tsunami metrics. As an example, different values of the critical slip weakening distance D_c or the possibility to consider the contribution of horizontal sea-floor deformation (Tanioka & Satake, 1996b; Tanioka & Seno, 2001) to the tsunami initial condition might modify the maximum amplitude of the source time history (see Figure 1b) and hence generate different wave amplitudes, flow-depths, and maximum run-ups. Besides, as discussed in section 3.3, we used a single slope to model the interface between the fault and the seafloor for all the cases and this allowed us to perform several tsunami simulations from a single rupture dynamic model. However, the use of a different and more realistic interface geometry is expected to slightly change the wave amplitudes as an effect of the variable dip and its time history, even when ending up with the same residual amplitude (See Figure S16a in Supporting Information). Nevertheless, at least regarding the latter point, we verified for some of the performed simulations that the ranges of ΔD_{max} on the coast and the $\Delta\eta_{max}$ offshore values (for TD-NH vs IS-NH comparison) are not significantly affected by these initial source amplitude perturbations (See Figure S16 and its caption in Supporting Information). Therefore, we can argue that the results presented in section 4 as well as the general interpretation presented in this section hold for most of the conditions that simply affect the maximum amplitude of the waves triggered in the vicinity of the source.

We focused on megathrust earthquakes while tsunamis may arise also from other type of mechanisms such as the outer-rise normal events for which time-dependent and non-hydrostatic modelling might have a non-negligible effect as well (Baba et al., 2021). One should be cautious to extend the findings of this study to those events and related tsunamis because they feature different radiation fields and sea-floor deformation history and space scale.

Finally, more complex models, taking into account the solid-acoustic coupling at the elastic-fluid interface (e.g. Ma, 2022), more sophisticated dynamic effects, like bi-material slip amplification (e.g. Scala et al. 2017), off-fault damage dissipation (e.g. Wilson & Ma, 2021, Ma, 2023) and realistic, short-sized bathymetry features as the ones shown within the insets of Figure 1(c), may affect the results. All these physical complexities, even though well beyond the scope of this work, deserve a deeper investigation possibly in a fully 3D coupled seismic-tsunami source model.

6 Conclusions

The main goal of this work is to understand when the accuracy needed to model the earthquake source and tsunami generation can be achieved with the commonly adopted simplifications (e.g. instantaneous source, shallow water) that reduce the computational cost. This is crucial for applications like the PTHA (e.g., Grezio et al., 2017; Davies et al., 2018; Basili et al., 2021; Behrens et al., 2021), where many scenarios need to be simulated, and tsunami early warning (e.g., Selva et al., 2021), where a short time-to-solution is needed. We measured the accuracy of the solutions in terms of wave amplitude and inundation metrics (flow-depth and run-up) for a Tohoku-like test-case using different topo-bathymetric morphologies. We systematically compared the approximated results and the ones deriving from a more realistic representation of the physical processes, accounting for a time-dependent earthquake-tsunami source and/or a multi-layer non-hydrostatic tsunami modelling. We varied systematically the duration and the size of the tsunami sources, using realistic ranges related to the corresponding seismic source and surrounding medium parameters, in particular the stress drop and the rigidity around the fault plane.

The main results can be summarized as follows:

1. An instantaneous source leads to increasingly less accurate results as the velocity of the seismic source decreases and becomes comparable with the characteristic velocity of tsunami propagation, in turn proportional to the square root of the bathymetric depth. However, within this framework, the size of the rupture also plays a fundamental role with larger ruptures leading to less accurate solutions. The inundation metrics are systematically overestimated by the instantaneous source approximation.
2. For what concerns the comparison between shallow water and non-hydrostatic, in realistic conditions featuring an average bathymetric depth $H \ll \lambda$ (horizontal extension of the source) the discrepancy for the maximum wave amplitudes and inundations are often not significant. Even for very small ruptures the relative flow-depth and run-up overestimation from SW-IS as compared to NH-IS are always smaller than the 10%. Nevertheless, when we compare NH and SW in those conditions requiring TD source modelling, such discrepancy increases up to $\sim$20%. Thus, it is almost always recommended to use NH modeling when dealing with time dependent seismic ruptures. In this frame, the common use of multi sub-faults, activated at different instants, along with a SW propagation, might lead to large overestimation.
3. All the results presented depend on the geometric characteristics of the topo/bathymetry in the vicinity of the coast and inland. The differences between TD and IS inundation on flatter bathymetric profiles (e.g., the ones characterizing the flood plains) are smaller than those for steeper profiles. As a result, flooding on a flatter bathymetry could be modelled with sufficient accuracy as an instantaneous source, as has been shown for some real tsunamigenic events (Satake et al. 2013).
4. The maximum run-up features a resonant mechanism, that is an amplified R_{max} in correspondence of a narrow range of the source size λ. The size of resonance was shown

to be inversely proportional to $\sqrt{\tan\theta}$ with θ being the topo-bathymetry slope in the vicinity of the coastline.

5. Comparing all these results with real events, we found that megathrust and tsunami earthquakes might require non-hydrostatic time-dependent modelling, in particular for more pronounced variation of nearshore topo-bathymetry to prevent overestimation of inundation intensity. Conversely, tsunami generated by deeper higher stress drop seismic ruptures can be simulated through approximated IS-SW modelling, still preserving enough accuracy in terms of propagating waves and inundation features.

- **Acknowledgments**

This research has been partially funded by MCIN/AEI/10.13039/501100011033 and by the "European Union NextGenerationEU/PRTR" through the grant PDC2022-133663-C21 and by MCIN/AEI/10.13039/50110001103 and by "ERDF A way of making Europe", by the European Union through the grant PID2022-137637NB-C21

Open Research

The whole simulated dataset is available at the following link: https://zenodo.org/doi/10.5281/zenodo.10497579

All the figures were originally produced for this paper through the software MATLAB: version 2023b. First accessed: September 2023. Academic license number: 40500131.

References

Abercrombie, R. E., Bannister, S., Ristau, J., & Doser, D. (2017). Variability of earthquake stress drop in a subduction setting, the Hikurangi Margin, New Zealand. *Geophysical Journal International*, *208*(1), 306–320. https://doi.org/10.1093/gji/ggw393

Abrahams, L. S., Krenz, L., Dunham, E. M., Gabriel, A.-A., & Saito, T. (2023). Comparison of methods for coupled earthquake and tsunami modelling. *Geophysical Journal International*, *234*(1), 404–426. https://doi.org/10.1093/gji/ggad053

Adsuara, J. E., Cordero-Carrión, I., Cerdá-Durán, P., & Aloy, M. A. (2016). Scheduled Relaxation Jacobi method: Improvements and applications. Journal of Computational Physics, 321, 369–413. https://doi.org/10.1016/j.jcp.2016.05.053

Audusse, E., Bristeau, M.-O., Perthame, B., & Sainte-Marie, J. (2011). A multilayer Saint-Venant system with mass exchanges for shallow water flows. Derivation and numerical validation. *ESAIM: Mathematical Modelling and Numerical Analysis*, *45*(1), 169–200. https://doi.org/10.1051/m2an/2010036

Baba, T., Chikasada, N., Imai, K., Tanioka, Y., & Kodaira, S. (2021). Frequency dispersion amplifies tsunamis caused by outer-rise normal faults. *Scientific Reports*, *11*(1), 20064. https://doi.org/10.1038/s41598-021-99536-x

Babeyko, A., Lorito, S., Hernandez, F., Lauterjung, J., Løvholt, F., Rudloff, A., Sørensen, M., Androsov, A., Aniel-Quiroga, I., Armigliato, A., Baptista, M. A., Baglione, E., Basili, R., Behrens, J., Brizuela, B., Bruni, S., Cambaz, D., Cantavella Nadal, J., Carillho, F., … Yalciner, A. (2022). Towards the new Thematic Core Service Tsunami within the EPOS Research Infrastructure. *Annals of Geophysics*, *65*(2), DM215. https://doi.org/10.4401/ag-8762

Banerjee, P., Pollitz, F., Nagarajan, B., & Bürgmann, R. (2007). Coseismic Slip Distributions of the 26 December 2004 Sumatra–Andaman and 28 March 2005 Nias Earthquakes from <scp>gps</scp> Static Offsets. *Bulletin of the Seismological Society of America*, *97*(1A), S86–S102. https://doi.org/10.1785/0120050609

Basili, R., Brizuela, B., Herrero, A., Iqbal, S., Lorito, S., Maesano, F. E., Murphy, S., Perfetti, P., Romano, F., Scala, A., Selva, J., Taroni, M., Tiberti, M. M., Thio, H. K., Tonini, R., Volpe, M., Glimsdal, S., Harbitz, C. B., Løvholt, F., … Zaytsev, A. (2021). The Making of the NEAM Tsunami Hazard Model 2018 (NEAMTHM18). *Frontiers in Earth Science*, *8*. https://doi.org/10.3389/feart.2020.616594

Behrens, J., Løvholt, F., Jalayer, F., Lorito, S., Salgado-Gálvez, M. A., Sørensen, M., Abadie, S., Aguirre-Ayerbe, I., Aniel-Quiroga, I., Babeyko, A., Baiguera, M., Basili, R., Belliazzi, S., Grezio, A., Johnson, K., Murphy, S., Paris, R., Rafliana, I., De Risi, R., … Vyhmeister, E. (2021). Probabilistic Tsunami Hazard and Risk Analysis: A Review of Research Gaps. *Frontiers in Earth Science*, *9*. https://doi.org/10.3389/feart.2021.628772

Beji, S., & Battjes, J. A. (1994). Numerical simulation of nonlinear wave propagation over a bar. Coastal Engineering, 23(1–2), 1–16. https://doi.org/10.1016/0378-3839(94)90012-4

Bilek, S. L., & Lay, T. (1999). Rigidity variations with depth along interplate megathrust faults in subduction zones. *Nature*, *400*(6743), 443–446. https://doi.org/10.1038/22739

Bilek, S. L., Rotman, H. M. M., & Phillips, W. S. (2016). Low stress drop earthquakes in the rupture zone of the 1992 Nicaragua tsunami earthquake. *Geophysical Research Letters*, *43*(19). https://doi.org/10.1002/2016GL070409

Bonaventura, L., Fernández-Nieto, E. D., Garres-Díaz, J., & Narbona-Reina, G. (2018). Multilayer shallow water models with locally variable number of layers and semi-implicit time discretization. *Journal of Computational Physics*, *364*, 209–234. https://doi.org/10.1016/j.jcp.2018.03.017

Brocchini, M., & Peregrine, D. H. (1996). Integral flow properties of the swash zone and averaging. *Journal of Fluid Mechanics*, *317*, 241–273. https://doi.org/10.1017/S0022112096000742

Burridge, R. (1973). Admissible Speeds for Plane-Strain Self-Similar Shear Cracks with Friction but Lacking Cohesion. *Geophysical Journal International*, *35*(4), 439–455. https://doi.org/10.1111/j.1365-246X.1973.tb00608.x

Castro Díaz, M. J., & Fernández-Nieto, E. (2012). A Class of Computationally Fast First Order Finite Volume Solvers: PVM Methods. SIAM Journal on Scientific Computing, 34(4), A2173–A2196. https://doi.org/10.1137/100795280

Casulli, V. (1999). A semi-implicit finite difference method for non-hydrostatic, free-surface flows. *International Journal for Numerical Methods in Fluids*, *30*(4), 425–440. https://doi.org/10.1002/(SICI)1097-0363(19990630)30:4<425::AID-FLD847>3.0.CO;2-D

Chazel, F., Lannes, D., & Marche, F. (2011). Numerical Simulation of Strongly Nonlinear and Dispersive Waves Using a Green–Naghdi Model. Journal of Scientific Computing, 48(1–3), 105–116. https://doi.org/10.1007/s10915-010-9395-9

Chorin, A. J. (1968). Numerical Solution of the Navier-Stokes Equations. Mathematics of Computation, 22(104), 745. https://doi.org/10.2307/2004575

Davies, G., & Griffin, J. (2020). Sensitivity of Probabilistic Tsunami Hazard Assessment to Far-Field Earthquake Slip Complexity and Rigidity Depth-Dependence: Case Study of Australia. *Pure and Applied Geophysics*, *177*(3), 1521–1548. https://doi.org/10.1007/s00024-019-02299-w

Davies, G., Griffin, J., Løvholt, F., Glimsdal, S., Harbitz, C., Thio, H. K., Lorito, S., Basili, R., Selva, J., Geist, E., & Baptista, M. A. (2018). A global probabilistic tsunami hazard assessment from earthquake sources. *Geological Society, London, Special Publications*, *456*(1), 219–244. https://doi.org/10.1144/SP456.5

Davies, G., Weber, R., Wilson, K., & Cummins, P. (2022). From offshore to onshore probabilistic tsunami hazard assessment via efficient Monte Carlo sampling. *Geophysical Journal International*, *230*(3), 1630–1651. https://doi.org/10.1093/gji/ggac140

Dingemans, M. W. (1994). MAST PROJECT 1: WAVES G8-M Comparison of computations with Boussinesq-like models and laboratory measurements.

Ebeling, C. W., & Okal, E. A. (2012). An extension of the E/M0 tsunami earthquake discriminant Θ to regional distances. *Geophysical Journal International*, *190*(3), 1640–1656. https://doi.org/10.1111/j.1365-246X.2012.05566.x

Ehara, A., Salmanidou, D. M., Heidarzadeh, M., & Guillas, S. (2023). Multi-level emulation of tsunami simulations over Cilacap, South Java, Indonesia. *Computational Geosciences*, *27*(1), 127–142. https://doi.org/10.1007/s10596-022-10183-1

Escalante, C., Fernández-Nieto, E. D., Garres-Díaz, J., & Mangeney, A. (2023). Multilayer Shallow Model for Dry Granular Flows with a Weakly Non-hydrostatic Pressure. *Journal of Scientific Computing*, *96*(3), 88. https://doi.org/10.1007/s10915-023-02299-y

Escalante, C., Fernández-Nieto, E. D., Garres-Díaz, J., Morales de Luna, T., & Penel, Y. (2023). Non-hydrostatic layer-averaged approximation of Euler system with enhanced dispersion properties. *Computational and Applied Mathematics*, *42*(4), 177. https://doi.org/10.1007/s40314-023-02309-7

Escalante, C., Fernández-Nieto, E. D., Morales de Luna, T., & Castro, M. J. (2019). An Efficient Two-Layer Non-hydrostatic Approach for Dispersive Water Waves. *Journal of Scientific Computing*, *79*(1), 273–320. https://doi.org/10.1007/s10915-018-0849-9

Escalante, C., Morales de Luna, T., & Castro, M. J. (2018). Non-hydrostatic pressure shallow flows: GPU implementation using finite volume and finite difference scheme. *Applied Mathematics and Computation*, *338*, 631–659. https://doi.org/10.1016/j.amc.2018.06.035

Fernández-Nieto, E. D., Koné, E. H., & Chacón Rebollo, T. (2014). A Multilayer Method for the Hydrostatic Navier-Stokes Equations: A Particular Weak Solution. *Journal of Scientific Computing*, *60*(2), 408–437. https://doi.org/10.1007/s10915-013-9802-0

Fernández-Nieto, E. D., Parisot, M., Penel, Y., & Sainte-Marie, J. (2018). A hierarchy of dispersive layer-averaged approximations of Euler equations for free surface flows. *Communications in Mathematical Sciences*, *16*(5), 1169–1202. https://doi.org/10.4310/CMS.2018.v16.n5.a1

Festa, G., & Vilotte, J.-P. (2005). The Newmark scheme as velocity-stress time-staggering: an efficient PML implementation for spectral element simulations of elastodynamics.

Geophysical Journal International, *161*(3), 789–812. https://doi.org/10.1111/j.1365-246X.2005.02601.x
Folesky, J., Kummerow, J., & Shapiro, S. A. (2021). Stress Drop Variations in the Region of the 2014 M_W 8.1 Iquique Earthquake, Northern Chile. *Journal of Geophysical Research: Solid Earth*, *126*(4). https://doi.org/10.1029/2020JB020112
Gailler, A., Hébert, H., Schindelé, F., & Reymond, D. (2018). Coastal Amplification Laws for the French Tsunami Warning Center: Numerical Modeling and Fast Estimate of Tsunami Wave Heights Along the French Riviera. *Pure and Applied Geophysics*, *175*(4), 1429–1444. https://doi.org/10.1007/s00024-017-1713-9
Geist, E. L., & Bilek, S. L. (2001). Effect of depth-dependent shear modulus on tsunami generation along subduction zones. *Geophysical Research Letters*, *28*(7), 1315–1318. https://doi.org/10.1029/2000GL012385
Gibbons, S. J., Lorito, S., Macías, J., Løvholt, F., Selva, J., Volpe, M., Sánchez-Linares, C., Babeyko, A., Brizuela, B., Cirella, A., Castro, M. J., de la Asunción, M., Lanucara, P., Glimsdal, S., Lorenzino, M. C., Nazaria, M., Pizzimenti, L., Romano, F., Scala, A., … Vöge, M. (2020). Probabilistic Tsunami Hazard Analysis: High Performance Computing for Massive Scale Inundation Simulations. *Frontiers in Earth Science*, *8*. https://doi.org/10.3389/feart.2020.591549
Glimsdal, S., Løvholt, F., Harbitz, C. B., Romano, F., Lorito, S., Orefice, S., Brizuela, B., Selva, J., Hoechner, A., Volpe, M., Babeyko, A., Tonini, R., Wronna, M., & Omira, R. (2019). A New Approximate Method for Quantifying Tsunami Maximum Inundation Height Probability. *Pure and Applied Geophysics*, *176*(7), 3227–3246. https://doi.org/10.1007/s00024-019-02091-w
Gopinathan, D., Heidarzadeh, M., & Guillas, S. (2021). Probabilistic quantification of tsunami current hazard using statistical emulation. *Proceedings of the Royal Society A: Mathematical, Physical and Engineering Sciences*, *477*(2250). https://doi.org/10.1098/rspa.2021.0180
Grezio, A., Babeyko, A., Baptista, M. A., Behrens, J., Costa, A., Davies, G., Geist, E. L., Glimsdal, S., González, F. I., Griffin, J., Harbitz, C. B., LeVeque, R. J., Lorito, S., Løvholt, F., Omira, R., Mueller, C., Paris, R., Parsons, T., Polet, J., … Thio, H. K. (2017). Probabilistic Tsunami Hazard Analysis: Multiple Sources and Global Applications. *Reviews of Geophysics*, *55*(4), 1158–1198. https://doi.org/10.1002/2017RG000579
Hayes, G. P., Moore, G. L., Portner, D. E., Hearne, M., Flamme, H., Furtney, M., & Smoczyk, G. M. (2018). Slab2, a comprehensive subduction zone geometry model. *Science*, *362*(6410), 58–61. https://doi.org/10.1126/science.aat4723
Huang, Y., Meng, L., & Ampuero, J.-P. (2012). A dynamic model of the frequency-dependent rupture process of the 2011 Tohoku-Oki earthquake. *Earth, Planets and Space*, *64*(12), 1061–1066. https://doi.org/10.5047/eps.2012.05.011
Ida, Y. (1972). Cohesive force across the tip of a longitudinal-shear crack and Griffith's specific surface energy. *Journal of Geophysical Research*, *77*(20), 3796–3805. https://doi.org/10.1029/JB077i020p03796
Kajiura, K. (1963). The leading wave of a tsunami. *Bulletin of Earthquake Research Institute, University of Tokyo*, *41*, 535–571.
Kanamori, H. (1971). Seismological evidence for a lithospheric normal faulting — the Sanriku earthquake of 1933. *Physics of the Earth and Planetary Interiors*, *4*(4), 289–300. https://doi.org/10.1016/0031-9201(71)90013-6

Kanamori, H., & Brodsky, E. E. (2004). The physics of earthquakes. *Reports on Progress in Physics*, *67*(8), 1429–1496. https://doi.org/10.1088/0034-4885/67/8/R03

Kazolea, M., & Delis, A. I. (2013). A well-balanced shock-capturing hybrid finite volume–finite difference numerical scheme for extended 1D Boussinesq models. Applied Numerical Mathematics, 67, 167–186. https://doi.org/10.1016/j.apnum.2011.07.003

Komatitsch, D., & Vilotte, J.-P. (1998). The spectral element method: An efficient tool to simulate the seismic response of 2D and 3D geological structures. *Bulletin of the Seismological Society of America*, *88*(2), 368–392. https://doi.org/10.1785/BSSA0880020368

Kozdon, J. E., & Dunham, E. M. (2013). Rupture to the Trench: Dynamic Rupture Simulations of the 11 March 2011 Tohoku Earthquake. *Bulletin of the Seismological Society of America*, *103*(2B), 1275–1289. https://doi.org/10.1785/0120120136

LeVeque, R. J., Waagan, K., González, F. I., Rim, D., & Lin, G. (2016). Generating Random Earthquake Events for Probabilistic Tsunami Hazard Assessment. *Pure and Applied Geophysics*, *173*(12), 3671–3692. https://doi.org/10.1007/s00024-016-1357-1

Li, L., Lay, T., Cheung, K. F., & Ye, L. (2016). Joint modeling of teleseismic and tsunami wave observations to constrain the 16 September 2015 Illapel, Chile, M_w 8.3 earthquake rupture process. *Geophysical Research Letters*, *43*(9), 4303–4312. https://doi.org/10.1002/2016GL068674

Lotto, G. C., & Dunham, E. M. (2015). High-order finite difference modeling of tsunami generation in a compressible ocean from offshore earthquakes. *Computational Geosciences*, *19*(2), 327–340. https://doi.org/10.1007/s10596-015-9472-0

Lotto, G. C., Jeppson, T. N., & Dunham, E. M. (2019). Fully Coupled Simulations of Megathrust Earthquakes and Tsunamis in the Japan Trench, Nankai Trough, and Cascadia Subduction Zone. *Pure and Applied Geophysics*, *176*(9), 4009–4041. https://doi.org/10.1007/s00024-018-1990-y

Ludwig, W. J., Nafe, J. E., & Drake, C. L. (1970). Seismic refraction New York: Wiley-Interscience. *The Sea, Edited by Maxwell, A. E.*, *4*(1), 53–84.

Ma, G., Shi, F., & Kirby, J. T. (2012). Shock-capturing non-hydrostatic model for fully dispersive surface wave processes. *Ocean Modelling*, *43–44*, 22–35. https://doi.org/10.1016/j.ocemod.2011.12.002

Ma, S. (2022). Dynamic off-fault failure and tsunamigenesis at strike-slip restraining bends: Fully-coupled models of dynamic rupture, ocean acoustic waves, and tsunami in a shallow bay. *Tectonophysics*, *838*, 229496. https://doi.org/10.1016/j.tecto.2022.229496

Ma, S. (2023). Wedge plasticity and a minimalist dynamic rupture model for the 2011 MW 9.1 Tohoku-Oki earthquake and tsunami. *Tectonophysics*, *869*, 230146. https://doi.org/10.1016/j.tecto.2023.230146

Macías, J., Escalante, C., & Castro, M. J. (2021a). Multilayer-HySEA model validation for landslide-generated tsunamis – Part 1: Rigid slides. *Natural Hazards and Earth System Sciences*, *21*(2), 775–789. https://doi.org/10.5194/nhess-21-775-2021

Macías, J., Escalante, C., & Castro, M. J. (2021b). Multilayer-HySEA model validation for landslide-generated tsunamis – Part 2: Granular slides. *Natural Hazards and Earth System Sciences*, *21*(2), 791–805. https://doi.org/10.5194/nhess-21-791-2021

Makinoshima, F., Oishi, Y., Yamazaki, T., Furumura, T., & Imamura, F. (2021). Early forecasting of tsunami inundation from tsunami and geodetic observation data with convolutional neural networks. *Nature Communications*, *12*(1), 2253. https://doi.org/10.1038/s41467-021-22348-0

Meade, B. J. (2007). Algorithms for the calculation of exact displacements, strains, and stresses for triangular dislocation elements in a uniform elastic half space. *Computers & Geosciences*, *33*(8), 1064–1075. https://doi.org/10.1016/j.cageo.2006.12.003

Miyake, H., Koketsu, K., & Furumura, T. (2008). *SOURCE MODELING OF SUBDUCTION-ZONE EARTHQUAKES AND LONG-PERIOD GROUND MOTION VALIDATION IN THE TOKYO METROPOLITAN AREA*.

Murphy, S., Di Toro, G., Romano, F., Scala, A., Lorito, S., Spagnuolo, E., Aretusini, S., Festa, G., Piatanesi, A., & Nielsen, S. (2018). Tsunamigenic earthquake simulations using experimentally derived friction laws. *Earth and Planetary Science Letters*, *486*, 155–165. https://doi.org/10.1016/j.epsl.2018.01.011

Murphy, S., Scala, A., Herrero, A., Lorito, S., Festa, G., Trasatti, E., Tonini, R., Romano, F., Molinari, I., & Nielsen, S. (2016). Shallow slip amplification and enhanced tsunami hazard unravelled by dynamic simulations of mega-thrust earthquakes. *Scientific Reports*, *6*(1), 35007. https://doi.org/10.1038/srep35007

Nakano, M., Murphy, S., Agata, R., Igarashi, Y., Okada, M., & Hori, T. (2020). Self-similar stochastic slip distributions on a non-planar fault for tsunami scenarios for megathrust earthquakes. *Progress in Earth and Planetary Science*, *7*(1), 45. https://doi.org/10.1186/s40645-020-00360-0

Oglesby, D. D., Archuleta, R. J., & Nielsen, S. B. (2000). Dynamics of dip-slip faulting: Explorations in two dimensions. *Journal of Geophysical Research: Solid Earth*, *105*(B6), 13643–13653. https://doi.org/10.1029/2000JB900055

Okada, Y. (1985). Surface deformation due to shear and tensile faults in a half-space. *Bulletin of the Seismological Society of America*, *75*(4), 1135–1154. https://doi.org/10.1785/BSSA0750041135

Okal, E. A., Kirby, S. H., & Kalligeris, N. (2016). The Showa Sanriku earthquake of 1933 March 2: a global seismological reassessment. *Geophysical Journal International*, *206*(3), 1492–1514. https://doi.org/10.1093/gji/ggw206

Ricchiuto, M., & Filippini, A. G. (2014). Upwind residual discretization of enhanced Boussinesq equations for wave propagation over complex bathymetries. Journal of Computational Physics, 271, 306–341. https://doi.org/10.1016/j.jcp.2013.12.048

Roeber, V., Cheung, K. F., & Kobayashi, M. H. (2010). Shock-capturing Boussinesq-type model for nearshore wave processes. *Coastal Engineering*, *57*(4), 407–423. https://doi.org/10.1016/j.coastaleng.2009.11.007

Romano, F., Gusman, A. R., Power, W., Piatanesi, A., Volpe, M., Scala, A., & Lorito, S. (2021). Tsunami Source of the 2021 M_W 8.1 Raoul Island Earthquake From DART and Tide-Gauge Data Inversion. *Geophysical Research Letters*, *48*(17). https://doi.org/10.1029/2021GL094449

Romano, F., Lorito, S., Lay, T., Piatanesi, A., Volpe, M., Murphy, S., & Tonini, R. (2020). Benchmarking the Optimal Time Alignment of Tsunami Waveforms in Nonlinear Joint Inversions for the Mw 8.8 2010 Maule (Chile) Earthquake. *Frontiers in Earth Science*, *8*. https://doi.org/10.3389/feart.2020.585429

Saito, T., Baba, T., Inazu, D., Takemura, S., & Fukuyama, E. (2019). Synthesizing sea surface height change including seismic waves and tsunami using a dynamic rupture scenario of anticipated Nankai trough earthquakes. *Tectonophysics*, *769*, 228166. https://doi.org/10.1016/j.tecto.2019.228166

Sallarès, V., & Ranero, C. R. (2019). Upper-plate rigidity determines depth-varying rupture behaviour of megathrust earthquakes. *Nature*, *576*(7785), 96–101. https://doi.org/10.1038/s41586-019-1784-0

Satake, K., Fujii, Y., Harada, T., & Namegaya, Y. (2013). Time and Space Distribution of Coseismic Slip of the 2011 Tohoku Earthquake as Inferred from Tsunami Waveform Data. *Bulletin of the Seismological Society of America*, *103*(2B), 1473–1492. https://doi.org/10.1785/0120120122

Scala, A., Festa, G., Vilotte, J. -P., Lorito, S., & Romano, F. (2019). Wave Interaction of Reverse-Fault Rupture With Free Surface: Numerical Analysis of the Dynamic Effects and Fault Opening Induced by Symmetry Breaking. *Journal of Geophysical Research: Solid Earth*, *124*(2), 1743–1758. https://doi.org/10.1029/2018JB016512

Scala, A., Festa, G., & Vilotte, J.-P. (2017). Rupture dynamics along bimaterial interfaces: a parametric study of the shear-normal traction coupling. *Geophysical Journal International*, ggw489. https://doi.org/10.1093/gji/ggw489

Scala, A., Lorito, S., Romano, F., Murphy, S., Selva, J., Basili, R., Babeyko, A., Herrero, A., Hoechner, A., Løvholt, F., Maesano, F. E., Perfetti, P., Tiberti, M. M., Tonini, R., Volpe, M., Davies, G., Festa, G., Power, W., Piatanesi, A., & Cirella, A. (2020). Effect of Shallow Slip Amplification Uncertainty on Probabilistic Tsunami Hazard Analysis in Subduction Zones: Use of Long-Term Balanced Stochastic Slip Models. *Pure and Applied Geophysics*, *177*(3), 1497–1520. https://doi.org/10.1007/s00024-019-02260-x

Scala, A. (2024). Dataset repository for paper "On the relation between seismic source dynamics, tsunami generation and propagation, and numerical modelling complexity for large earthquakes in subduction zones" [Data set]. Zenodo. https://doi.org/10.5281/zenodo.10497580

Selva, J., Lorito, S., Volpe, M., Romano, F., Tonini, R., Perfetti, P., Bernardi, F., Taroni, M., Scala, A., Babeyko, A., Løvholt, F., Gibbons, S. J., Macías, J., Castro, M. J., González-Vida, J. M., Sánchez-Linares, C., Bayraktar, H. B., Basili, R., Maesano, F. E., … Amato, A. (2021). Probabilistic tsunami forecasting for early warning. *Nature Communications*, *12*(1), 5677. https://doi.org/10.1038/s41467-021-25815-w

Sepúlveda, I., Liu, P. L. -F., Grigoriu, M., & Pritchard, M. (2017). Tsunami hazard assessments with consideration of uncertain earthquake slip distribution and location. *Journal of Geophysical Research: Solid Earth*, *122*(9), 7252–7271. https://doi.org/10.1002/2017JB014430

Skarlatoudis, A. A., Somerville, P. G., & Thio, H. K. (2016). Source-Scaling Relations of Interface Subduction Earthquakes for Strong Ground Motion and Tsunami Simulation. *Bulletin of the Seismological Society of America*, *106*(4), 1652–1662. https://doi.org/10.1785/0120150320

Souty, V., & Gailler, A. (2021). Fast High-Resolution S-PTHA Along the Western Mediterranean Sea Coastlines. Application to the Bay of Cannes. *Frontiers in Earth Science*, *9*. https://doi.org/10.3389/feart.2021.765610

Stefanakis, T., Dias, F., & Dutykh, D. (2012). Resonant Long-Wave Run-Up On A Plane Beach. *Proceedings of the 22nd (2012) International Offshore and Polar Engineering Conference*, 116–121. https://hal.science/hal-00728747

Stoker J. J. (1992). *Water Waves: The Mathematical Theory with Applications*. Wiley Classic Library.

Strasser, F. O., Arango, M. C., & Bommer, J. J. (2010). Scaling of the Source Dimensions of Interface and Intraslab Subduction-zone Earthquakes with Moment Magnitude. *Seismological Research Letters*, *81*(6), 941–950. https://doi.org/10.1785/gssrl.81.6.941

Sugawara, D. (2021). Numerical modeling of tsunami: advances and future challenges after the 2011 Tohoku earthquake and tsunami. *Earth-Science Reviews*, *214*, 103498. https://doi.org/10.1016/j.earscirev.2020.103498

Takahashi, N., Kodaira, S., Tsuru, T., Park, J.-O., Kaneda, Y., Suyehiro, K., Kinoshita, H., Abe, S., Nishino, M., & Hino, R. (2004). Seismic structure and seismogenesis off Sanriku region, northeastern Japan. *Geophysical Journal International*, *159*(1), 129–145. https://doi.org/10.1111/j.1365-246X.2004.02350.x

Tanioka, Y., & Satake, K. (1996a). Fault parameters of the 1896 Sanriku Tsunami Earthquake estimated from Tsunami Numerical Modeling. *Geophysical Research Letters*, *23*(13), 1549–1552. https://doi.org/10.1029/96GL01479

Tanioka, Y., & Satake, K. (1996b). Tsunami generation by horizontal displacement of ocean bottom. *Geophysical Research Letters*, *23*(8), 861–864. https://doi.org/10.1029/96GL00736

Tanioka, Y., & Seno, T. (2001). Sediment effect on tsunami generation of the 1896 Sanriku Tsunami Earthquake. *Geophysical Research Letters*, *28*(17), 3389–3392. https://doi.org/10.1029/2001GL013149

Titov, V. V., & Synolakis, C. E. (1995). Modeling of Breaking and Nonbreaking Long-Wave Evolution and Runup Using VTCS-2. Journal of Waterway, Port, Coastal, and Ocean Engineering, 121(6), 308–316. https://doi.org/10.1061/(ASCE)0733-950X(1995)121:6(308)

Tonini, R., Basili, R., Maesano, F. E., Tiberti, M. M., Lorito, S., Romano, F., Scala, A., & Volpe, M. (2020). Importance of earthquake rupture geometry on tsunami modelling: the Calabrian Arc subduction interface (Italy) case study. *Geophysical Journal International*, *223*(3), 1805–1819. https://doi.org/10.1093/gji/ggaa409

Uenishi, K., & Rice, J. R. (2003). Universal nucleation length for slip-weakening rupture instability under nonuniform fault loading. *Journal of Geophysical Research: Solid Earth*, *108*(B1). https://doi.org/10.1029/2001JB001681

Venkataraman, A., & Kanamori, H. (2004). Observational constraints on the fracture energy of subduction zone earthquakes. *Journal of Geophysical Research: Solid Earth*, *109*(B5). https://doi.org/10.1029/2003JB002549

Williamson, A. L., Rim, D., Adams, L. M., LeVeque, R. J., Melgar, D., & González, F. I. (2020). A Source Clustering Approach for Efficient Inundation Modeling and Regional Scale Probabilistic Tsunami Hazard Assessment. *Frontiers in Earth Science*, *8*. https://doi.org/10.3389/feart.2020.591663

Wilson, A., & Ma, S. (2021). Wedge Plasticity and Fully Coupled Simulations of Dynamic Rupture and Tsunami in the Cascadia Subduction Zone. *Journal of Geophysical Research: Solid Earth*, *126*(7). https://doi.org/10.1029/2020JB021627

Yamada, N., & Iwata, T. (2005). Long-period ground motion simulation in the Kinki area during the MJ 7.1 foreshock of the 2004 off the Kii peninsula earthquakes. *Earth, Planets and Space*, *57*(3), 197–202. https://doi.org/10.1186/BF03351815

Ye, L., Lay, T., Kanamori, H., & Rivera, L. (2016). Rupture characteristics of major and great ($M_w \geq 7.0$) megathrust earthquakes from 1990 to 2015: 1. Source parameter scaling relationships. *Journal of Geophysical Research: Solid Earth*, *121*(2), 826–844. https://doi.org/10.1002/2015JB012426

Yoshimoto, M., & Yamanaka, Y. (2014). Teleseismic inversion of the 2004 Sumatra-Andaman earthquake rupture process using complete Green's functions. *Earth, Planets and Space*, *66*(1), 152. https://doi.org/10.1186/s40623-014-0152-4

On the relation between seismic source dynamics, tsunami generation and propagation, and numerical modelling complexity for large earthquakes in subduction zones

A. Scala[1,2], S. Lorito[2], C. Escalante Sánchez[3], F. Romano[2], G. Festa[1,2], A. Abbate[2,4], H. B. Bayraktar[2], M. J. Castro[3], J. Macías[3], J. M. Gonzalez-Vida[3]

[1] Department of Physics “Ettore Pancini”, University Federico II, Napoli, 80126, Italy.

[2] Istituto Nazionale di Geofisica e Vulcanologia, Rome, 00143, Italy

[3] EDANYA Group, University of Malaga, Malaga, 29080, Spain

[4] Department of Mathematics, Informatics and Geosciences, University of Trieste, 34128, Italy

Corresponding author: Antonio Scala (antonio.scala@unina.it)

Key Points:

- Slow and large ruptures (e.g. tsunami earthquakes and mega-thrust) require a time-dependent, non-hydrostatic modelling
- Deeper, high stress-drop earthquakes might be modelled through an instantaneous source, shallow water approximation
- Inundation depends on bathymetric features: larger inundations on steeper depth gradients and resonant run-up amplifications are observed

Abstract

Tsunamis are rare, destructive events, whose generation, propagation and coastal impact processes involve several complex physical phenomena. Most tsunami applications, like probabilistic tsunami hazard assessment, make extensive use of large sets of numerical simulations, facing a systematic trade-off between the computational costs and the modelling accuracy. For seismogenic tsunami, the source is often modelled as an instantaneous sea-floor displacement due to the fault static slip distribution, while the propagation in open-sea is computed through a shallow water approximation.

Here, through 1D earthquake-tsunami coupled simulations of large M>8 earthquakes in Tohoku-like subduction zone, we tested for which conditions the instantaneous source (IS) and/or the shallow water (SW) approximations can be used to simulate with enough accuracy the whole tsunami evolution. We used as a reference a time-dependent (TD), multi-layer, non-hydrostatic (NH) model whose source features, duration, and size, are based on seismic rupture dynamic simulations with realistic stress drop and rigidity, within a Tohoku-like environment.

We showed that slow ruptures, generating slip in shallow part of subduction slabs (e.g. tsunami earthquakes), and very large events, with an along-dip extension comparable with the trench-coast distance (e.g. mega-thrust) require a TD-NH modelling, in particular when the bathymetry close to the coast features sharp depth gradients. Conversely, deeper, higher stress-drop events can be accurately modelled through an IS-SW approximation. We finally showed to what extent inundation depend on bathymetric geometrical features: (i) steeper bathymetries generate larger inundations and (ii) a resonant mechanism emerges with run-up amplifications associated with larger source size on flatter bathymetries.

Plain Language Summary

In the last two decades, tsunamis originated by large earthquakes have generated major damages and more than 250k casualties. Strategies to quantify and mitigate the associated risk are based on numerical simulations of the physical processes regulating the generation, propagation of the waves and subsequent flooding on the coast. These simulations would require unaffordable computational resources; to solve this problem, numerous approximations are introduced that need to be tested. In this work, we studied which earthquakes, depending on the speed at which they deform the sea bottom when they trigger a tsunami, and on how big they are, require a more detailed modelling approach, and which ones, instead, might be accurately simulated through approximated approaches. We also show how such findings are related to different bathymetric characteristics near the coast and inland, which may enhance or reduce the tsunami effects.

1 Introduction

Due to the rare occurrence of tsunamis and the strong influence of bathymetry and coastal morphology on tsunami evolution, tsunami community makes use of numerical simulations to compensate for the scarcity of observations (see e.g. Behrens et al., 2021; Sugawara, 2021; Babeyko et al., 2022). Here, we consider tsunamis generated by earthquakes in subduction zones, since the most destructive tsunamis in the last decades were generated by interslab subduction events (Grezio et al., 2017; Davies & Griffin, 2020). For these sources, tsunami simulations require the numerical modelling of the earthquake source process, the solid-fluid interaction during the tsunami generation, and the wave propagation on a complex bathymetry up to the inundation of the coastal topography. Numerical modelling of these diverse physical processes typically requires different solvers with a certain level of coupling between them. They range from the simplest solution consisting of instantaneous seafloor from a static slip (Okada, 1985) to more complex modelling implementing either a two-step (Saito et al., 2019) or a fully coupled approach to describe the seismic and the tsunami source processes (Lotto & Dunham, 2015; Lotto et al., 2019).

Each solver adopts approximations and simplifications to limit the computational cost associated with the simulations. This is particularly relevant when an application requires many high-resolution simulations, such as in probabilistic tsunami hazard analysis (PTHA, Grezio et al., 2017; Davies et al., 2018; Gibbons et al., 2020; Basili et al., 2021; Behrens et al., 2021), inverse problems (Romano et al., 2020, 2021), or tsunami forecasting for early warning purposes (Selva et al., 2021). One way to cope with the containment of the computational cost is to approximate the tsunami height after shoaling, or the runup process with analytical or stochastic methods (Brocchini & Peregrine, 1996; Gailler et al., 2018; Glimsdal et al., 2019; Souty & Gailler, 2021). Recently, an emerging way to approach the problem is to exploit emulators as surrogates of the simulations (Gopinathan et al., 2021; Ehara et al., 2023) or AI-based techniques to estimate the inundation parameters from offshore or low-resolution simulations (Makinoshima et al., 2021; Ehara et al., 2023). From a distinct perspective, the computational cost of numerical modeling can be reduced without losing resolution by opportunely decreasing the number of simulations. This can be done by performing an optimal sampling of the parameter space (e.g. Davies et al., 2022), or by exploiting the similarity of tsunami scenarios due to different earthquake sources (e.g. Williamson et al., 2020).
All these strategies are complementary to the purpose of this study, which aims to establish an optimal simulation strategy for the specific case of large earthquakes in subduction zones and the ensuing tsunamis.

The subduction slab is often represented as a planar or a segmented interface (LeVeque et al., 2016; Li et al., 2016; Sepúlveda et al., 2017). However, recently, curved surfaces are being modelled increasingly often (Nakano et al., 2020; Scala et al., 2020; Tonini et al., 2020). The seismic rupture on the interface is modelled as an instantaneous elastic dislocation, or as the linear superposition of dislocations of different amplitude representing heterogeneous slip distributions, in a homogeneous half-space (Okada, 1985; Meade, 2007). The resulting instantaneous elastic deformation of the sea floor is eventually smoothed (Kajiura, 1963) to obtain a static sea surface anomaly, that generates waves owing to gravity. The tsunami propagation is then numerically computed in the nonlinear shallow water approximation (Stoker J. J., 1992) until the coastal inundation, fully neglecting dispersive wave effects.

However, the rupture process has a finite duration and the zones affected by elastic dislocation change as the seismic rupture expands. The spatial and temporal scales of the seismic rupture process, controlled by roughness, size and speed, have a wide range of variability making the above-mentioned approximations valid depending on specific applications (see Abrahams et al., 2023 and references therein). At the first order, we can characterize the scales through the duration and extent of the initial sea level perturbation which, in turn, can be related to the average rigidity and the stress drop of the seismic source (Bilek & Lay, 1999; Geist & Bilek, 2001). On the other hand, the generation process cannot always be accurately modelled as an instantaneous deformation smoothed with a Kajiura filter as input to a shallow water model to propagate the initial static displacement. For slow ruptures, or short-wavelength sea bottom displacements, a more accurate modelling of the time-dependent coupling between the sea bottom and the water layer, and of the subsequent tsunami evolution may be necessary (see, as well, the discussion in Abrahams et al., 2023 and references therein). Beyond that, several numerical comparisons against experimental data (Ma et al., 2012; Macías et al., 2021a, 2021b) demonstrated that accounting for dispersive effects is essential for faithfully simulating waves in the vicinity of the continental shelf, as well as to model run-up, shoaling, and wet-dry areas. Although in a different tectonic setting (outer-rise normal faulting) the dispersive effects might amplify tsunami waves (Baba et al., 2021). To enhance the model's non-linear dispersive properties, it is crucial also to include information on the vertical structure of the flow. In Macías et al. (2021a, 2021b), waves generated after rigid or granular landslides were found to be high frequency and dispersive, with the generated flows exhibiting a complex vertical structure.

Here, we aim to address if and for which cases a modelling of time-dependent rupture complexity and non-hydrostatic regime accounting for a more physically realistic modelling of seismic source and tsunami processes, respectively, are necessary to guarantee the accuracy of the results for the forecasting of tsunamis generated by large earthquakes in subduction zones. At the same time, we approach this problem keeping in mind the compromise between accuracy and computational demand for practical applications. Thus, a complementary goal is to identify, depending on the cases, which is the minimum computational effort needed to preserve an acceptable accuracy in the results.

In this work we start with the 1D time-dependent sea-level displacement (along the x -direction of the sketch in Figure 1a) generated by a 1D numerical model of the seismic rupture (Murphy et al., 2016, 2018; Scala et al., 2017, 2019). This displacement is the input for the 1D tsunami generation and evolution with a non-hydrostatic 3-layer tsunami code (Escalante et al., 2019, 2023). The bathymetry and topography adopted in this study are simplified 1-D versions of transects perpendicular to the coast of Tohoku in Japan. This setup is used as the ‘ground-truth’ to benchmark more simplified approaches using either instantaneous seafloor displacement, or a one-layer shallow water scheme, or a combination of the two. Although we are aware of the limitations of the 1D approach, it allows us to perform a large number of simulations spanning a broad range of rupture velocities and extensions on different bathymetric profiles and coastal slopes, and with enough spatial resolution to perform inundation modelling. The metrics used to validate the different approaches/approximations are the sea-surface evolution, the offshore maximum wave amplitude at different depths, seaward and landward from the trench, the flow depth and the maximum runup inland.

The paper is organized as follows: the coupled modeling of earthquake and tsunami and the numerical setup are presented in sections 2 and 3, respectively. In section 4 the results are described, while discussions about results and final remarks can be found in sections 5 and 6, respectively.

2 Methods: Coupling modelling of earthquake and tsunami

2.1 Earthquake rupture dynamics modelling

To model 1D earthquake rupture dynamics in a 2D elastic domain, we used the same approach proposed in Scala et al. (2017, 2019). We solve the general elastodynamic problem:

$$\begin{cases} \rho(x)\ddot{u}(x,t) = \vec{\nabla}\cdot\sigma(x,t) \\ \sigma(x,t) = c(x)\colon\vec{\nabla}u(x,t) \end{cases} \tag{1}$$

In equation (1), x is the position, t the time, $\rho(x)$ is the bulk density, $\sigma(x,t)$ and $c(x)$ the stress and the elastic coefficient tensors respectively, while $u(x,t)$ represents the particle displacement. The traction $T = \sigma \cdot n$ is imposed to be zero on the seafloor interface, neglecting the acoustic coupling between the seafloor and the water itself.

The fault is modelled through a domain decomposition around a 1D interface where the continuity of the traction T is imposed. The fault slip and slip rate are defined as $\delta u(\tilde{x},t) = u_2(x_2,t) - u_1(x_1,t)$ and $\delta v(\tilde{x},t) = v_2(x_2,t) - v_1(x_1,t)$ respectively, with $\tilde{x}$ representing a generic point on the interface while the subscripts 1 and 2 mark the quantities computed on the two sides of the fault. The contact between the two sides of the fault is modelled through the Signorini's condition: the normal traction is either negative and hence the two lips are in contact and prone to frictionally slide or equal to zero, making each side of the interface a free surface and generating an opening (see also eq. (2) in Scala et al., 2019). When the two sides of the fault interface are in contact, the frictional sliding is governed by the following Coulomb condition:

$$\begin{cases} [T^t(\tilde{x},t) - C(\tilde{x}) + fT^n(\tilde{x},t)]\cdot|\delta v^t(\tilde{x},t)| = 0 \\ [T^t(\tilde{x},t) - C(\tilde{x}) + fT^n(\tilde{x},t)] \le 0 \end{cases} \tag{2}$$

In equation (2), the superscripts t and n represent the tangential and normal directions with respect to the interface, C is a level of remote cohesion on the fault that is assumed to decrease to zero approaching the free surface. The friction f is here assumed to linearly decrease with slip from a static level f_s to a dynamic one f_d over a finite length of slip D_c (Slip weakening; Ida, 1972).
Elastodynamic equations with a sliding interface are numerically solved through a 2D Spectral Element Method (SEM, Komatitsch & Vilotte, 1998) where quadrangular elements are discretized using $9x9$ Gauss-Lobatto-Legendre nodes, ensuring at least 5 points for the minimum propagating wavelength and at least 4 points to model the fault cohesive zone (Scala et al., 2017).The free surface is naturally modelled in SEM while the other boundaries mimic an infinite half-space through the implementation of PMLs (Festa & Vilotte, 2005).
A Newmark second order forward time scheme is implemented with an average Courant number of about 0.04. Such a small value allows to model the shallowest part of the domain honouring the shape of the domain between the fault and the free surface, and ensuring the stability also in the stretched elements within this wedge.
The fault is modelled as a planar interface embedded in a homogeneous medium and forming a dip angle $\delta = 20°$ with the horizontal direction similarly to what proposed by Scala et al., (2019). The free surface, in turn, is inclined of an angle $\alpha = 3.5°$ with respect to the horizontal direction, this value being an average of the bathymetry slopes for the different profiles in the vicinity of the trench (Figure 1). Since we aim to model a simplified Tohoku-like environment in terms of fault

geometry and topo-bathymetric distributions (see Section 2.4 for more details), the dip angle represents an average value between the almost horizontal trench and the steeper slope of the deep crust-mantle interface as shown in other works (Kozdon & Dunham, 2013; Murphy et al., 2018) implementing 1D extrapolations of Slab 2.0 modelling (Hayes et al., 2018).
The remote stress field is oriented to mimic the combination of a vertical lithostatic and a horizontal tectonic loading. Their components are compatible with a reverse frictional sliding mechanism as expected for interface subduction events. On the fault interface the initial normal traction $T_0^n(\tilde{x},t)$ linearly increases to mimic the increase of lithostatic loading (Huang et al., 2012; Murphy et al., 2016, 2018). The static and the dynamic friction coefficients f_s and f_d are imposed to be equal to 0.25 and 0.05 respectively to prevent the opening at the free surface (Scala et al., 2019). The strength excess $s = (f_s T_0^n - T_0^t)/(T_0^t - f_d T_0^n)$ is set to 2 on the entire interface to avoid the acceleration of rupture toward supershear regimes (Burridge, 1973), since it was never observed during the largest reverse subduction tsunamigenic earthquakes. Therefore, the shear strength $f_s T_0^n$ the dynamic level $f_d T_0^n$, the initial shear stress T_0^t and the local stress drop $T_0^t - f_d T_0^n$ increase with depth accordingly to T_0^n. A cohesion C vanishing toward the fault-free surface intersection is imposed with a value of about 10% of the maximum stress
All the input/output physical quantities are normalised to infer general results from the simulations. The slip on the fault δu and the ensuing displacement on the surface d are normalised by means of the critical slip weakening distance leading to the dimensionless parameters $\widetilde{\delta u} = \delta u/D_c$ and $\tilde{d} = d/D_c$. All the tractions T are normalised through the maximum stress drop on the fault $\Delta\sigma_0$ as $\tilde{T} = T/\Delta\sigma_0$. The distances z, including the fault extension W and the ensuing tsunami source size λ (See Figure 1), and the time t are normalised as $\tilde{z} = \frac{\Delta\sigma_0}{\mu D_c} z$ and $\tilde{t} = \frac{V_s \Delta\sigma_0}{\mu D_c} t = \frac{\Delta\sigma_0}{V_s \rho D_c} t$ respectively. In these two latter normalisation factors, μ and ρ are the medium rigidity and density respectively with $V_s = \sqrt{\mu/\rho}$ the S-wave propagation velocity. This setup allows us to define an ensemble of different tsunami sources featuring a broad range of source extensions and durations running a single dimensionless earthquake simulation and selecting parameters like $D_c, \Delta\sigma_0, \mu$ and ρ in realistic ranges constrained by observations (see details in Section 3).
To trigger the spontaneous crack, we defined an asperity featuring an initial shear stress larger than the shear strength and having a size L_c large enough to allow the rupture to move away from the nucleation zone (Uenishi & Rice, 2003) .The nucleation asperity is placed at an intermediate depth with respect to the whole domain. Previous numerical experiments have shown that this is the preferential nucleation depth to generate events rupturing the whole domain and hence to describe the behaviour of a megathrust earthquake (Murphy et al., 2018).

2.2 Tsunami modelling

We used a multilayer shallow-water non-hydrostatic model. The multilayer approach was introduced by Audusse et al. (2011) and Fernández-Nieto et al. (2014) to capture vertical effects in shallow flows. The equations are depth-averaged at every layer, leading to a layer-wise constant approximation. Such a technique was already efficiently applied to landslide-generated tsunamis (Macías et al., 2021a) and for dry granular flows (Escalante et al., 2023a). Concerning dispersion, following the pioneering work of Casulli (1999), non-hydrostatic effects are incorporated into the shallow water framework by splitting the total pressure into hydrostatic and non-hydrostatic components, providing a given profile for the non-hydrostatic component and the vertical velocity, together with the incompressibility condition. This approach has been recently further developed improving the dispersive layer-averaged approximations (Fernández-Nieto et al., 2018; Escalante et al., 2023b), and efficiently GPU-implemented using finite volume and finite difference schemes (Escalante et al., 2018). A vertical discretization of the fluid into several layers only approximates the physics of the fluid. The number of layers can be increased to bring the system close to three-dimensional solvers, becoming able of adequately describing the vertical structure of the flow. That leads to notable improvements in the dispersion properties of the model. The multilayer model used in this study is the following (see, Fernández-Nieto et al., 2018):

$$\begin{gathered}\partial_t h + \partial_x(h\bar{u}) = 0,\\ \partial_t(h_\alpha u_\alpha) + \partial_x(h_\alpha u_\alpha^2) + g h_\alpha \partial_x \eta + u_{\alpha+1/2}\Gamma_{\alpha+1/2} - u_{\alpha-1/2}\Gamma_{\alpha-1/2}\\ = -\frac{1}{2} h_\alpha \partial_x\big(p_{\alpha+1/2} + p_{\alpha-1/2}\big) + \big(p_{\alpha+1/2} - p_{\alpha-1/2}\big)\partial_x z_\alpha + K_{\alpha-1/2} - K_{\alpha+1/2} - \tau_\alpha^u,\\ \partial_x(h_\alpha w_\alpha) + \partial_x(h_\alpha w_\alpha u_\alpha) + w_{\alpha+1/2}\Gamma_{\alpha+1/2} - w_{\alpha-1/2}\Gamma_{\alpha-1/2} = -h_\alpha\big(p_{\alpha+1/2} - p_{\alpha-1/2}\big) - \tau_\alpha^w.\end{gathered} \tag{3}$$

In the system (3), $h(x,t)$ represents the total water height at each point $x \in \Omega \subset R$, and time $t \geq 0$, where Ω is the considered (horizontal) domain. The water height is decomposed along the vertical axis into a prescribed number of layers $L \geq 1$ (see Figure S1 in Supporting Information). For any layer α, its thickness will be assumed to be $h_\alpha = l_\alpha h$, for some values $l_\alpha \in (0,1)$ such that $\sum_{\alpha=1}^{L} l_\alpha = 1$. Usually, $l_\alpha = 1/L$ is selected. The upper and lower interfaces of the layer α are represented by $z_{\alpha+1/2}$ and $z_{\alpha-1/2}$, respectively, that is, $z_{\alpha+1/2} = z_b + \sum_{\beta=1}^{\alpha} l_\beta h$. The uppermost interface corresponds to the sea surface, denoted by $\eta(x,t) = h(x,t) + z_b(x,t)$; the lowermost one corresponds to the seafloor basin represented by $z_b(x,t)$, which is supposed to be perturbed by the earthquake. Finally, $z_\alpha = \frac{1}{2}\big(z_{\alpha-1/2} + z_{\alpha+1/2}\big)$ denotes the level of the middle point of the layer. The depth-averaged velocities in the horizontal and vertical directions are written as $u_\alpha(x,t)$, and $w_\alpha(x,t)$, respectively. Finally, $p_{\alpha+1/2}$ denotes the non-hydrostatic pressure at the interface $z_{\alpha+1/2}$, and is assumed to be 0 at the free surface. The mean of the depth-averaged horizontal velocities is indicated by $\bar{u} = \sum_{\alpha=1}^{L} l_\alpha u_\alpha$.
Moreover, for any field $f \in \{u,\ w\}$, we denote $f_{\alpha+1/2} = \frac{1}{2}(f_{\alpha+1} + f_\alpha)$. As usual $g = 9.81\ m/s^2$ is the gravity acceleration and $\Gamma_{\alpha+1/2}$ parametrizes the mass transfer across interfaces:

$$\Gamma_{\alpha+1/2} = \sum_{\beta=\alpha+1}^{L} \partial_x\left(h_\beta\big(u_\beta - \bar{u}\big)\right), \tag{4}$$

where we assume no mass transfer through the seafloor or the free surface ($\Gamma_{1/2} = \Gamma_{L+1/2} = 0$). Each layer is supplemented with the following divergence-free constraint $\mathcal{I}_\alpha = 0,\ \alpha \in \{1,2,\dots,L\}$, where

$$\begin{gathered}\mathcal{I}_\alpha = h\alpha\partial_x u_\alpha + 2\overline{w}_{\alpha+\frac{1}{2}} - 2w_\alpha,\\ \overline{w}_{\alpha+\frac{1}{2}} = \partial_t z_b + u_\alpha \partial_x z_{\alpha+1/2} - \sum_{\beta=1}^{\alpha} \partial_x\,(h_\beta u_\beta),\end{gathered} \tag{5}$$

and the term $\partial_t z_b$ accounts for the movement of the bottom interface.

Note that the system is endorsed with extra dissipation accounting for friction with the bottom (τ_α^u), for viscous terms that model the shear stresses between the layers ($K_{\alpha\pm1/2}$), and for the breaking of the waves near the coast (τ_α^w). Here, we used the following dissipation models proposed by Macías et al. (2021a)
For the friction effects between the water and the seafloor, we used a standard Gauckler-Manning friction formula applied to the lowest layer

$$\tau_\alpha^u = \begin{cases} gLn^2|u_1|\dfrac{hu_1}{h^{4/3}}, & \alpha = 0 \\ 0, & \alpha \in \{2,\dots,L\} \end{cases} \tag{6}$$

We followed a simplified version of the model presented in Bonaventura et al. (2018) for the shear stress between the layers

$$K_{\alpha+1/2} = -\nu\frac{u_{\alpha+1} - u_\alpha}{(h_{\alpha+1} + h_\alpha)/2} \tag{7}$$

where ν is a constant kinematic viscosity, and $K_{1/2} = K_{L+1/2} = 0$.

For the breaking dissipation model, we considered here an extension of the simple, efficient, and robust model considered in Escalante et al. (2019) for a two-layer model:

$$\tau_\alpha^w = C\, w_\alpha\, |\partial_x(hu_\alpha)|, \quad \alpha \in \{1,\dots,L\} \tag{8}$$

The coefficient $C(x,t)$ defines breaking criteria to switch on/off the dissipation of the energy due to the presence of a breaking wave (e.g., Roeber et al., 2010). Here, we used

$$C = \begin{cases} 35\left(\dfrac{|\bar{u}|}{0.4\sqrt{gh}} - 1\right) & \text{if } |\bar{u}| > \sqrt{gh}, \\ 0 & \text{if } |\bar{u}| \le \sqrt{gh}. \end{cases} \tag{9}$$

The system in equations (3)-(5) satisfies an energy balance equation (Fernández-Nieto et al., 2018). The used modelling includes the non-hydrostatic ocean response and accurately captures dispersion and related effects during tsunami propagation and generation (Ma et al., 2012; Macías et al., 2021a, 2021b). Using a standard, Stokes-type, Fourier analysis for the linearized version of equations (3)-(5) around the water at rest steady-state, the phase, group velocities, and linear shoaling gradient are determined and compared with the Airy or Stokes linear theory for different numbers of layers (see Figure S2 in the Supporting Information, where relative errors are shown for the phase and group velocities, as well as for the shoaling gradient). One can prove uniform convergence for the analytical values when the number of layers increases (Fernández-Nieto et al. 2018).

A detailed description of the numerical discretization and implementation of this model, along with the comparison of results with standard benchmark problems, were presented in Text S1 and Text S2 of Supporting Information.

3 Numerical setup and the simulated dataset

The time-dependent vertical displacements caused by the dynamic rupture simulations are used as generation mechanism for the tsunami simulations. The displacement of the bathymetry and of the topography are both considered. The intersection between the fault and the free surface (the seafloor) coincides with the deepest point of the bathymetry and corresponds to the trench (see sketch in Figure 1a). The zero height of the bathymetry represents the initial sea level and positive values represent the topographic elevation of the coast. The sea surface elevation for all the grid points, both offshore and inland, is collected each 30 seconds. All the tsunami simulations last 2 hours.

One example of the dimensionless sea floor deformation at various times during one simulation is shown in Figure1(b). The distance from the trench is meant along the horizontal direction. It is worth to notice that the final static deformation (yellow curve in Figure 1b) might feature a lower maximum amplitude with respect to the transient deformation occurring previously (green curves in Figure 1b). This effect is due to the surface deformation induced by the trapped waves within the wedge as already shown by Oglesby et al. (2000) and Scala et al. (2019). A secondary vanishing deformation with a maximum amplitude of about 25% of the final static displacement, still due to the propagating seismic waves, triggers a tsunami wave propagating rightward from the trench ahead of the main wave.

Starting from a single dimensionless seismic rupture simulation, a broad range of different tsunami sources can be modelled. Exploiting the normalization presented in Section 2.1, we can vary the rigidity μ and the density ρ of the medium, the stress drop $\Delta\sigma$ of the earthquake and the characteristic slip weakening distance D_c, to obtain different durations, maximum amplitudes, and lateral extensions. The event size is then directly connected to the characteristic tsunami source wavelength.

The rigidity and the density are selected to cover a broad range of elastic properties which typically characterize the slab interfaces at the characteristic seismogenic depths, integrating values from reports released by Earthquake Research Promotion of Japanese Government (available at https://jishin.go.jp/main/chousa/17apr_chikakozo/model_concept-e.pdf, with densities extrapolated through Ludwig et al., 1970) and from several tomographic models for the Japanese slab (e.g. Takahashi et al., 2004; Yamada & Iwata, 2005; Miyake et al., 2008). The sampled rigidity, density values, the shear wave velocity $V_s = \sqrt{\mu/\rho}$ and the corresponding subduction layers, are reported in Table S1 of Supporting Information.

The stress drop values are sampled in a range between 0.2 and 30 MPa according to general observations about crustal, downdip interplate and tsunami earthquakes (Kanamori & Brodsky, 2004; Venkataraman & Kanamori, 2004; Bilek et al., 2016; Abercrombie et al., 2017; Folesky et al., 2021). Within this range, we selected 15 values such that their logarithms are equally spaced. A single characteristic slip weakening distance is selected ($D_c = 2\ m$) leading to a maximum slip $\delta u{\sim}15\ m$ for the rupture dynamic simulations. This value is consistent with the one extrapolated for a $M_w = 9.0$ event according to the scaling law proposed by Skarlatoudis et al. (2016).

Combining all the sampled parameters, 345 different tsunami initial conditions could be set. However, most of them lead to either unrealistic or out of range of interest seismic source size.

The smallest rigidity values cannot be associated indeed with large stress drops and vice versa, to avoid modelling too small and too large earthquakes, respectively. Imposing a range of fault widths compatible with the expected value ($\pm 1\sigma$) of the scaling relations proposed by Strasser et al. (2010) for a magnitude interval $8.0 \leq M_w \leq 9.0$, we selected 81 out of the 345 combinations of parameters (See figure S9a and Table S2 in Supporting Information).
Each parameter combination leads to a characteristic source duration $\tau = \tau' \mu \mathrm{D_c}/(\Delta\sigma V_s)$ and to an along-dip source size $W = W' \mu D_c / \Delta\sigma$, with $\tau' = 17.1$ and $W' = 8.3$ representing the dimensionless duration and width computed through the dynamic rupture simulation. From τ and W values a proxy of rupture velocity V_r can be estimated (Figure S9b in Supporting Information). The rupture duration ranges between 25 s and 570 s, while $0.2 km/s \leq V_r \leq 2.3 km/s$, these values fitting the common observations for recent tsunamigenic earthquakes (Yoshimoto & Yamanaka, 2014; Ye et al., 2016). In the next section, all the results will be presented as a function of τ, W and the ratio $\tau/W \propto 1/\mathrm{V_s}$ that represents a size-normalized rupture duration and hence a measure of the characteristic rupture slowness. Some of the results will be presented as a function of $\lambda = W \cdot cos(dip) = W \cdot cos(20°)$ as indicated in Figure 1(a). This last quantity is the horizontal maximum extension of the seismic source and within this simple geometrical model represents a proxy of the characteristic wavelength of the source. The longest durations owe to small values of rigidity and stress drops, in turn deriving from shallow-depths rheological conditions, while the fastest sources are associated with large values of rigidity and stress drop, a more realistic condition for deeper events (Bilek & Lay, 1999; Geist & Bilek, 2001; Ebeling & Okal, 2012; Okal et al., 2016).Within this framework, the choice of a logarithmic scale for the stress drop along with the large number of models featuring small rigidity values (Table S2 in Supporting Information) allows us to more finely sample sources characterized by longer duration which are expected to mostly detach from the standard instantaneous source modelling.

We considered the time-dependent 3-layer non-hydrostatic model (hereinafter TD-NH) as the reference and we compared against it the simplified models (instantaneous source and shallow water, hereinafter IS and SW respectively). For the aim we simulated each initial condition 4 times (TD-NH, IS-NH, TD-SW and IS-SW). The IS were simulated imposing an instantaneous seafloor deformation equals to the final static displacement (as the yellow curve in Figure 1b). SW is simulated through a single layer hydrostatic approximation, and we used a Manning friction coefficient equal to 0.025. A constant Courant number equal to 0.9 is imposed. All these choices are justified by the performed tests, described in sections TextS1 and TextS2 in Supporting Information

The comparison is performed through three metrics: the wave amplitude η (sea surface elevation with respect to the still water level) and its maximum η_{max} at offshore gauges, the flow-depth D and its maximum D_{max} at onshore gauges (the water amplitude onto the topographic elevation) and the maximum run-up R_{max} that is the maximum topographic elevation reached by the tsunami during the inundation. For any metrics K we defined the discrepancy ΔK as the relative error due to the use of a simplified model:

$$\Delta K = \frac{K_{ref} - K_{simpl}}{K_{simpl}} \tag{10}$$

ΔK might assume negative values indicating that a simplified model produces an overestimation with respect to the reference one.

To investigate how much the results depend on the coupling between the tsunami and the oceanic and coastal morphology, the initial deformations are projected onto 6 different 1D topo-bathymetric profiles (colored lines on the map of Figure 1c). Each profile (blue lines in the insets around the map in Figure 1c) is extracted from the 30 arc-sec model SRTM30+ (https://topex.ucsd.edu/WWW_html/srtm30_plus.html) and then simplified to obtain piece-wise linear depth variations (colored profiles in the insets of Figure 1c) characterized by a planar scarp combined with either a planar or a segmented shelf towards and beyond the coast. This simplification allows to limit the effect of short size discontinuities and to provide general considerations about the effects depending on the large-scale geometrical features. The scarp slopes are quite similar to each other and are characterized by an average angle of 3.5° among the 6 profiles. Conversely, in the vicinity of the coast, the slopes are gentler in the southern part of the Tohoku region (Sendai and Fukushima areas), and steeper in the northern part (Iwate prefecture) with an intermediate behavior along the profile containing the nucleation area of the Tohoku earthquake. The mainland is modelled as a single slope. Most of the results presented in the next section will be obtained for the Tohoku nucleation area (red profile and bathymetry in Figure 1c) while a comparison between the different bathymetries is shown in section 4.3.

To ensure enough spatial resolution we performed a preliminary convergence test, running equivalent simulations on 6 grids characterized by different space sampling $\Delta x = [500m;\ 250m;\ 125m;\ 62{,}5m;\ 31{,}25m;\ 15{,}625m]$. We tested the discrepancy of each grid with respect to the finer one (assumed as a reference) computing the $\Delta_{\eta_{max}}$ offshore and the $\Delta_{D_{max}}$ on the coast similarly to eq. (**10**) but considering the module of the difference as numerator and the value on the finest grid as denominator. With this definition the Δ values represent the relative errors due to the use of a rougher grid. This analysis has been carried out extracting η_{max} and D_{max} at fixed gauge positions (regardless of the time at which these maxima are recorded) for two end-member initial conditions that is the largest size event (ID 1 in Table S2, $W = 275.3\ km$) and the smallest size one (ID 81 in Table S2 $W = 57.06\ km$) respectively. We retrieved $\Delta_{\eta_{max}} < 5\%$ everywhere and for both tests, already with rather rough grids (up to $\Delta x = 125\ m$ offshore and $\Delta x = 62.5\ m$ in the vicinity of the coast, Figures S10c and S10d in Supporting Information). However, $\Delta_{D_{max}}$ is below the threshold only for $\Delta x = 31{,}25\ m$ in the vicinity of the maximum run-up position at least for the smallest size simulations (see Figure S10a in Supporting Information). Since one of our aims is to model with enough accuracy the inundation features, including the maximum run-up, we finally used $\Delta x = 31{,}25\ m$ for the whole simulation dataset.

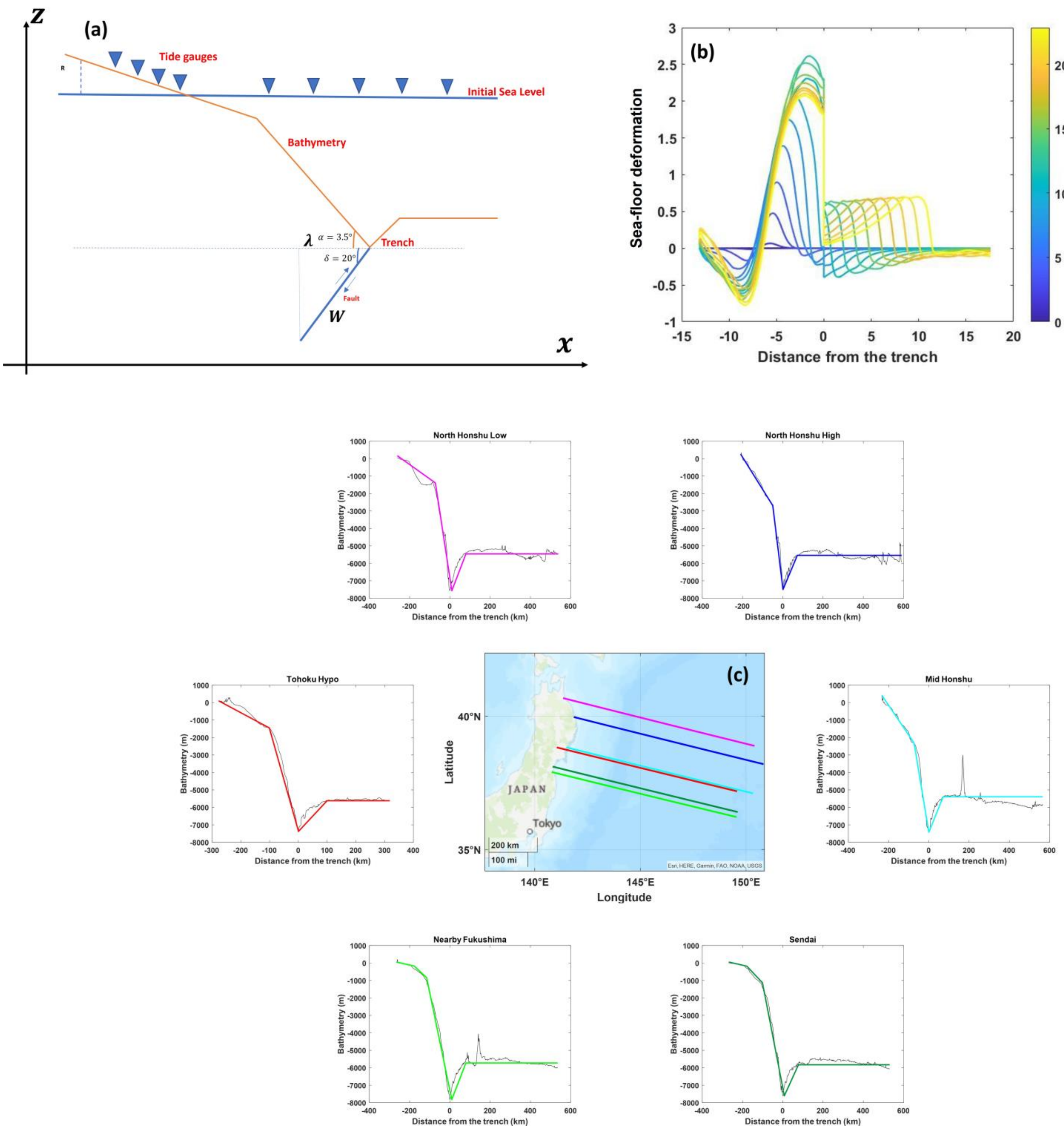
(a)
z
Tide gauges
Initial Sea Level
Bathymetry
Trench
$\alpha = 3.5°$
$\delta = 20°$
Fault
W
x
(b)
Sea-floor deformation
Distance from the trench
Time
North Honshu Low
North Honshu High
Tohoku Hypo
Mid Honshu
Nearby Fukushima
Sendai
Bathymetry (m)
Distance from the trench (km)
(c)
JAPAN
Tokyo
Latitude
Longitude
40°N
35°N
140°E
145°E
150°E
200 km
100 mi
Esri, HERE, Garmin, FAO, NOAA, USGS

Figure 1: Schematic description of the simulation setup. (a) Sketch of the geometrical setup. The angle between the bathymetry (orange line) and the horizontal dashed line is exaggerated for sake of clarity. The blue triangles represent the gauges where the wave amplitude is computed both inland and offshore. W and λ represent the width on the fault and the horizontal extension of the surface deformation respectively. (b) Time dependent vertical topo-bathymetric deformation as a function of the distance from the trench. The time increases from blue to yellow curves with a final static deformation featuring a lower maximum with respect to the transient deformation occurring before. All the variables are plotted as dimensionless parameters. (c) Different modelled bathymetries. The modelled bathymetries are extracted from the 1D profiles in the map. Within the insets the bathymetry variation for each profile is plotted as a black line while the simplified geometry used in the simulations is plotted with the same color of correspondent profile in the map.

4 Results

4.1 Off-shore and coastal wave amplitude

Time-dependent VS instantaneous source

First, we show a qualitative comparison between the water waves generated by the non-hydrostatic time-dependent (TD-NH) and instantaneous sources (IS-NH). Figure 2 shows the wave amplitude as a function of the distance from the trench for two different initial conditions (simulations ID 31 and 11 are plotted on the left and right columns respectively, see Table S2 in Supporting Information) at different time steps and for both TD-NH and IS-NH. While the two simulations are characterized by the same τ/W value and hence by an equivalent dynamic evolution, the simulations on the right panels (Figures 2b-d-f) feature a large enough W (and τ) to generate coastal subsidence. For both simulations (small and large W), the TD sources feature a larger maximum wave amplitude than the corresponding IS, and the maxima occurs at various times, as an effect of the different duration of the transient. However, this transient is rapidly attenuated during the landward propagation outside of the source region, and, starting from a certain time, the IS systematically features larger η_{max} with respect to the TD simulation (Figures 2e and 2f). Conversely, towards the open sea, rightward from the trench, we retrieve the opposite behavior with the TD source leading to larger yet delayed maximum η as an effect of the directivity (the seaward motion of the upper plate).

Regardless of the source temporal features (TD vs IS), the main difference between simulations with small and large W emerges while the waves are approaching the coast. For small W , such that λ is smaller than half distance between trench and the coast, (Figures 2a-c-e), the wave shoals. For larger ruptures (Figures 2b-d-f), the instantaneous sea drawback limits the shoaling and thus the amplification of the wave close to the coast as can be spotted by comparing Figures 2e and 2f.

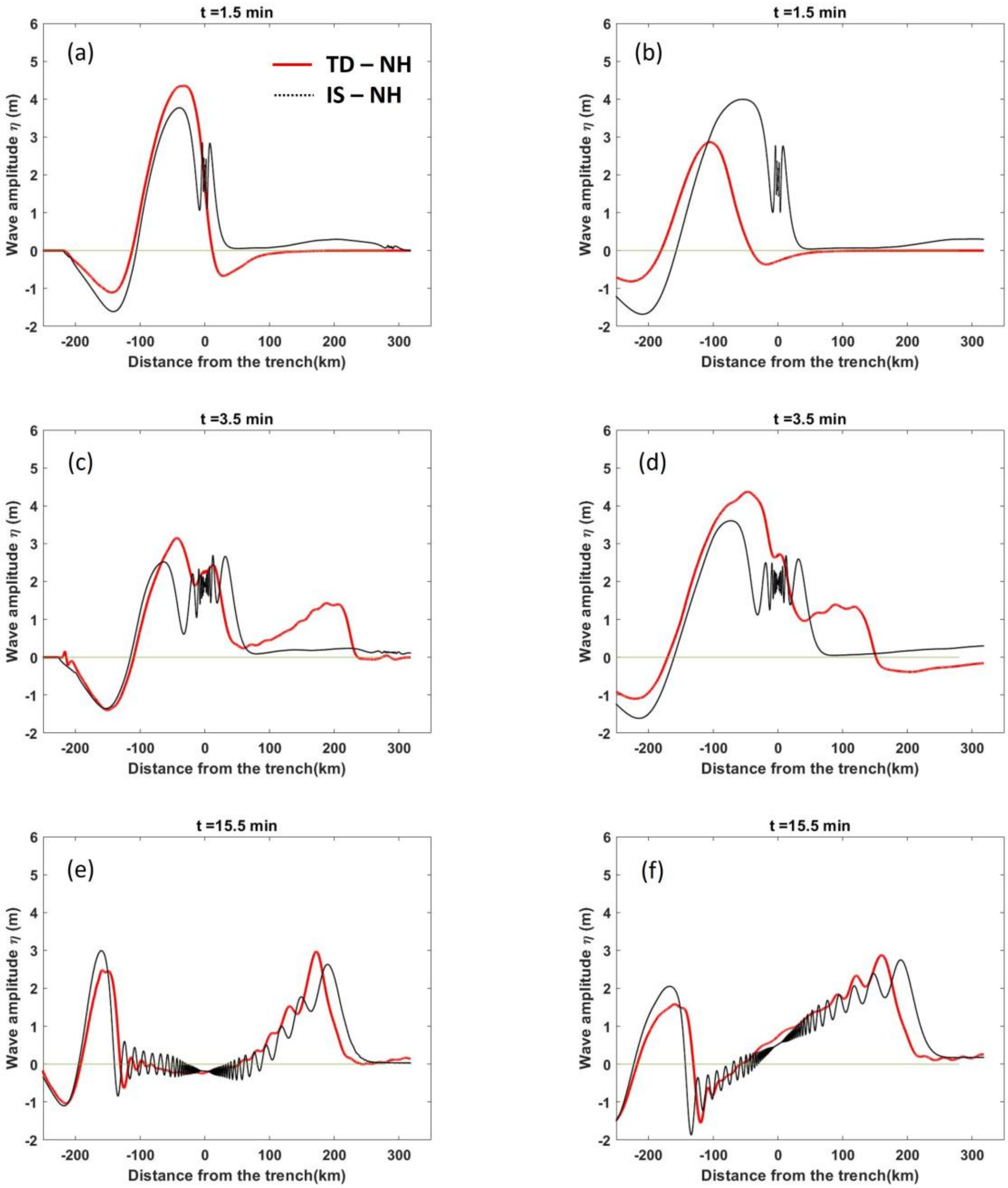

Figure 2: Wave amplitude as a function of the distance from the trench for TD – NH (red curves) and IS – NH (black dotted lines) at three different time steps and for two simulations: the ID 31 (left panels) and the ID 11 (right panels) in Table S2 in Supporting Information. These simulations represent examples of small and large-size sources, respectively. The whole evolution can be found in the Supporting Information (Movies S1 and S2).

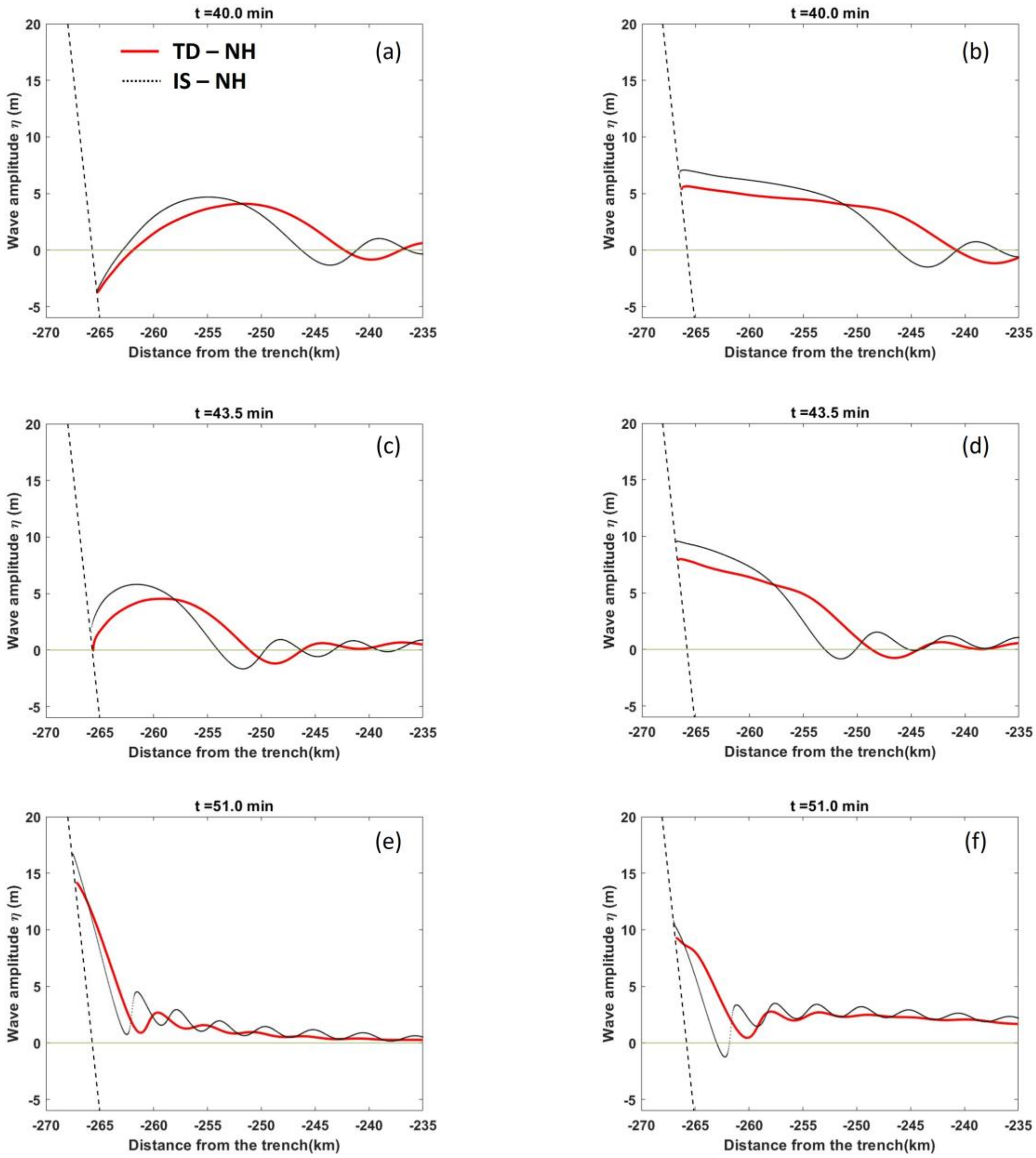

Figure 3: Wave amplitudes, zoomed around the coast, as a function of the distance from the trench for TD – NH (red curves) and IS – NH (black dotted lines) at three different time steps and for two simulations: the ID 31 (left panels) and the ID 11 (right panels) in Table S2 of Supporting Information. These simulations represent examples of small and large size sources respectively. The short-dashed line on the left represents the coastline within each panel. The whole evolution can be found in the Supporting Information (Movies S3 and S4).

This difference is evident also by zooming around the coastline (Figure 3) at a later stage ($t > 40\text{min}$). From this close-by view, it can also be seen that the inundation begins earlier for rupture with large W (Figure 3b), when for the small W simulation, the tsunami is still in the shoaling phase (Figure 3a). When the large source simulation has almost reached its maximum (Figure 3d), the inundation for the smaller source starts (Figure 3c), reaching in the end a maximum run-up that is about 1.5 times the one for the large W, for both IS and TD sources. This is a direct consequence of the potential energy accumulation during the shoaling process (Figures 3e and 3f). However, independently of the size and duration of the TD source, approximating it with an instantaneous source always results in a larger inundation both in terms of flow-depth D and maximum run-up R_{max}.

To systematically quantify the discrepancy between the IS and TD sources, we investigated the variability of $\Delta_{D_{max}}$ at the points on the coast (eq. (**10**)), as a function of τ/W (horizontal axis) and λ (different colors) for all the 81 simulations (see section 3 and Table S2 in Supporting Information). In Figure 4 the results for the first point on the coast are summarized. We observed that the IS source systematically overestimates the flow-depth ($\Delta_{D_{max}}$ values are always negative, Figure 4a). The slower the TD rupture, the larger the discrepancy with the correspondent IS simulation. A second trend depending on the source extension emerges, as for fixed τ/W, larger ruptures lead to larger discrepancies. A comparison between the time histories of the flow-depths at the first point on the coast is shown in Figure 4b, for the simulations inside the dashed rectangle in Figure 4a. The four simulations are characterized by the same source dynamic time scale, that is τ/W, with the larger extension due to a larger stress drop $\Delta\sigma$. The flow-depth amplitude D_{max} increases with λ until a maximum value (cyan curves in Fig. 4b) with an overestimation between 3% and 7% due to the instantaneous modelling. For larger λ, D_{max} decreases featuring larger overestimations up to about 14%. This overestimation is particularly significant for the largest λ values, because the inundation directly relates with source time history which becomes dominant given the virtual absence of landward propagation and shoaling. We have verified that comparable results hold when a SW propagation modelling is used, which is important because the most commonly adopted approximation is the SW-IS approach (Figure S11 of Supporting Information).

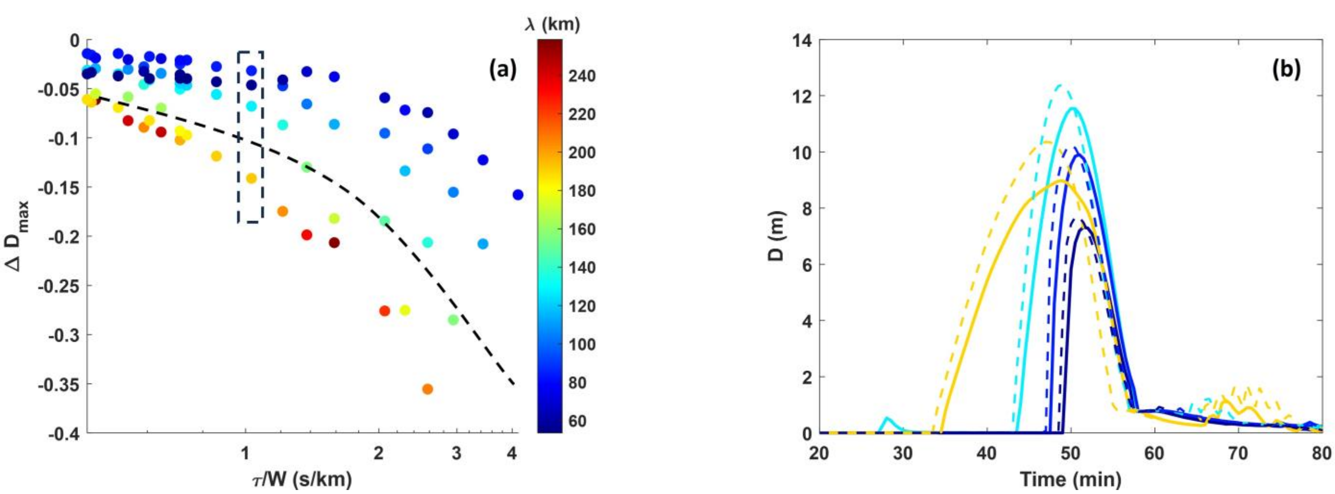

Figure 4: Relative discrepancy between time-dependent (TD-NH) and instantaneous source (IS-NH) results in terms of flow-depth at the first point on the coast (a) ΔD_{max} at the first point on the coast as a function of τ/W with color scale marking the source horizontal extension λ**.** The black dashed line separates the two highlighted trends for small and large ruptures. (b) Flow-depth as a

function of time for the four simulations within the black-dashed rectangle in panel (a) plotted with the same colors. In panel (b) TD and IS sources are represented through solid and dashed lines respectively.

Non-hydrostatic VS Shallow Water propagation

To perform a systematic comparison between the accuracies of NH and SW propagation schemes in modelling a tsunami generated by a TD seismic source, we run a set of SW propagation simulations of tsunamis triggered by the same seismic TD source as used in the NH simulations described in the previous section.

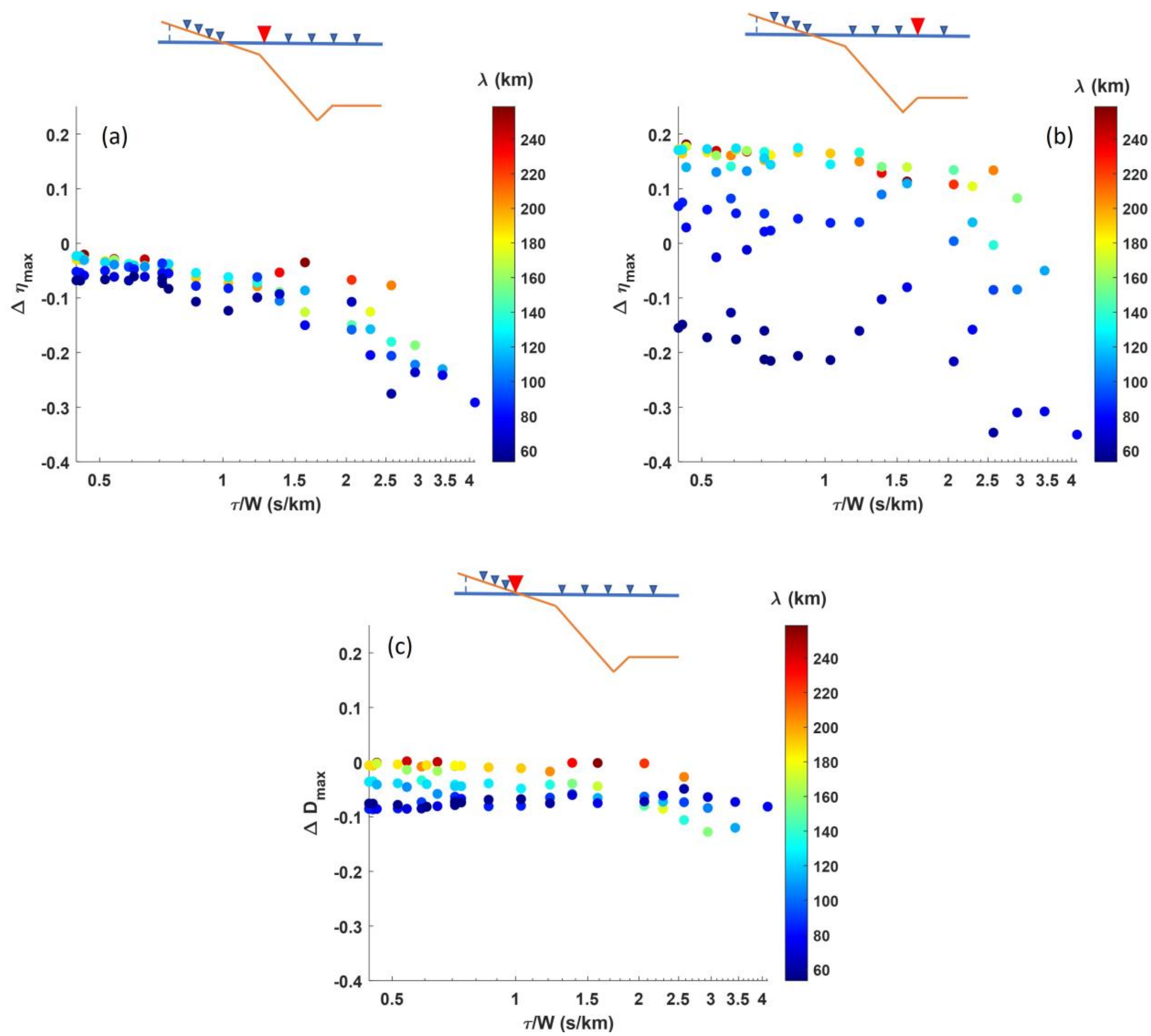

Figure 5**:** Relative discrepancy between Non-Hydrostatic (NH) and Shallow Water (SW) results when TD sources are used for both propagation regime. (a) $\Delta\eta_{max}$ at a gauge placed along the coastward propagation as a function of τ/W with color scale marking the source horizontal extension λ. (b) $\Delta\eta_{max}$ at a gauge placed rightward beyond the trench as a function of τ/W with color scale marking the source horizontal extension λ. (c) ΔD_{max} at the first point on coast as a function of τ/W with color scale marking the source horizontal extension λ. For sake of comparison the figures are plotted with the same scale. A sketch of the position of points where the Δ are computed is plotted within each panel.

Figures 5(a) and (b) show the $\Delta\eta_{max}$ for two gauges located between the source and the coast and beyond the trench respectively, while in Figure 5(c) the ΔD_{max} is shown for the first point on the coast. Even though for the smallest modelled source, λ is more than 7 times larger than the maximum sea-floor depth, and hence the SW limit is quite far to be violated (Abrahams et al. 2023), significant $\Delta_{\eta_{max}}$ with negative values down to -30% occurs, indicating that SW systematically overestimates the NH wave amplitude during the coastward propagation (Figure 5a). For the slowest and smallest ruptures, the $\left|\Delta_{\eta_{max}}\right|$ is enhanced as an effect of short wavelength oscillations affecting both the primary and the secondary waves. Such oscillations are due to coupling of the dynamic evolution of the source with the instantaneous dissipative shock introduced by the SW propagation (See wave evolution in left panels of Figure S12 in Supporting Information).

For smaller ruptures, a similar SW overestimation is retrieved also in the open ocean propagation beyond the trench, while a systematic underestimation emerges at intermediate and large source sizes λ as shown in Figure 5(b).

However, such differences affect to a lesser extent the flow-depth maximum amplitude on the coastal points with only few very slow simulations featuring a $|\Delta D_{max}|$ slightly larger than 0.1, as evidenced in Figure 5(c) for the slowest ruptures.
Modelling NH and SW regimes with IS instead significantly reduces $\left|\Delta_{\eta_{max}}\right|$ offshore (Figures S13a and b in Supporting Information) and $|\Delta D_{max}|$ on the coast (Figure S13c) for small source size λ, while the SW underestimation for intermediate and large λ values, beyond the trench, is characterized by similar $\Delta_{\eta_{max}}$. Despite in this condition the maximum amplitude metrics being overall convergent, an interesting feature emerges following the waveform evolution with time for the secondary waves. Indeed, when an instantaneous source is modelled, the NH propagation generates high-frequency oscillations behind the primary wave possibly hampering the correct modelling of secondary waves eventually generated by the dispersive propagation regime (Figure S14 in Supporting Information). In other words, in case of instantaneous ruptures with strong gradients, a singularity is generated on seafloor. The propagation of such a singularity generates a train of secondary waves that propagates overlapping to the dispersive waves. Such effect has been confirmed by laboratory experiment and convergence tests, performed with a refined grid and modelling 5 and 7 non-hydrostatic layers.

4.2 Inundation and maximum run-up

To address how the modelling approximations affect the inundation we used the maximum run-up R_{max} and $\Delta_{R_{max}}$ as metrics. We performed similar comparisons as for the amplitude, first between the TD-NH and IS-NH, and then between TD-SW and TD-NH. We show the results also for IS-SW.

Figure 6(a) shows the ΔR_{max} for IS-NH taking TD-NH as a reference, as a function of τ/W and λ. A trend similar to the one shown in Figure 4(a) is observed, with an increasing discrepancy for slower and larger ruptures. However, the largest ruptures generate significantly smaller values of both R_{max} and $\Delta_{R_{max}}$ as a consequence of the significant subsidence that completely prevents the shoaling limiting the run-up. When the same comparison is performed between TD-NH and TD-SW, we retrieved smaller discrepancies with maximum values of $\Delta_{R_{max}}$ around the 16% for the smallest modelled sources (Figure 6b). A negligible contribution to the discrepancy is associated to the parameter τ/W, which emerges only for very slow ruptures ($\tau/W > 3$ s/km)

The absolute R_{max} behavior for all the 81 simulations and for the 4 models is summarized in Figure 6(c) evidencing a resonant character as a function of λ. The resonance is pretty perfect for IS cases, with an optimal amplification for a narrow λ range, around 100-120 km. For TD sources, both for SW and NH, R_{max} is also influenced by the source duration leading to a scattered R_{max} pattern against λ still following the resonant trend. The λ value for which the resonance is observed depends on the specific costal slope, as will be illustrated in Section 4.3.

Focusing on the discrepancies for SW simulations we also highlight that: i) the rupture size for which the resonance is observed is independent of the propagation regime; ii) the overall SW overestimation holds even when the more realistic TD-NH and TD-SW are compared. However, in Figure 6(d), we observe that while with an IS the SW versus NH, ΔR_{max} is always less than 10%, it becomes larger with a TD source, with a maximum of about 16%. Looking at the time evolution of inundation (Figure S15 in Supporting Information), we confirmed that the largest ΔR_{max} emerging for small λ in TD simulations are actually due to the short-wavelength oscillations (left panels of Figure S15 in Supporting Information). These oscillations are attenuated for larger ruptures (Figure S15 of Supporting Information, right panels) and suppressed for IS simulations (black dotted lines in Figure S14)

To summarize, as expected in realistic conditions for large subduction earthquakes, with $\lambda \gg H$, the difference between NH and SW models are definitely less significant than the discrepancy emerging between IS and TD simulations, at least in terms of wave maximum amplitude and maximum run-up. However, the SW overestimation increases for very slow ruptures leading to $|\Delta| \sim 20\%$ for the investigated metrics. In terms of waveform features, as seen, the use of either a SW model for a TD source or a NH regime for instantaneous seafloor deformation causes short wavelength oscillations affecting both the smaller oscillations behind the primary wave and, sometimes, the inundation metrics, at least for $\lambda < \lambda_R$ with λ_R being the resonance wavelength described in Figure 6(c).

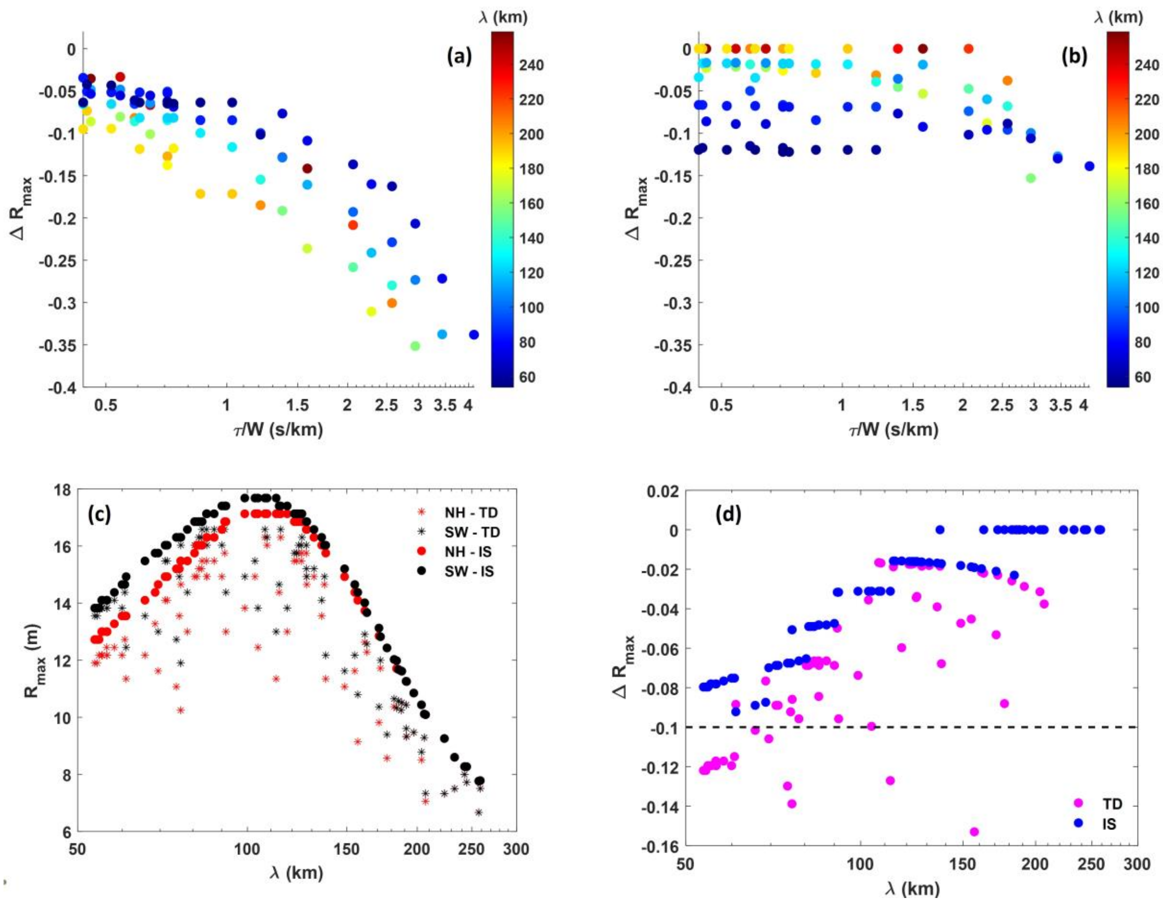

Figure 6: Maximum run-up R_{max} comparison between the four different models (TD-NH, IS-NH, TD-SW, IS-SW). (a) ΔR_{max} between TD-NH and IS-NH as a function of τ/W with color scale marking the source horizontal extension λ. (b) ΔR_{max} between TD-NH and TD-SW as a function of τ/W with color scale marking the source horizontal extension λ. For sake of comparison, the Figures in panels (a) and (b) are plotted with the same scale. (c) R_{max} on the coast as a function of λ for the four different models (d) ΔR_{max} as a function of λ with blue and magenta dots referring to IS-NH vs IS-SW and TD-NH Vs TD-SW comparison, respectively. The dashed line indicates that only for TD sources some simulations feature $|\Delta R_{max}| > 0.10$

4.3 Effect of bathymetry

To investigate the effect of different bathymetric conditions, particularly as far as the run-up resonance is concerned, we repeated the complete set of simulations for the other 5 simplified topo-bathymetric profiles (Figure 1c). While the 6 different bathymetries are similar in the deep part, they mostly differ in the slope at shallower depth in the vicinity of the coast and inland. Since some bathymetric profiles are similar, in Figure 7(a) we only show the results for three of them. The results shown so far were retrieved for the profile referred to as “Tohoku Hypo” (Figure 1c). The southernmost profile referred to as “Sendai” is characterized by a significantly flatter slope, while “North Honshu High” by a steeper slope in the vicinity of the coast. These three profiles are interpreted as a proxy of the overall behavior in presence of intermediate, flat and steep topo-bathymetric profiles, respectively.

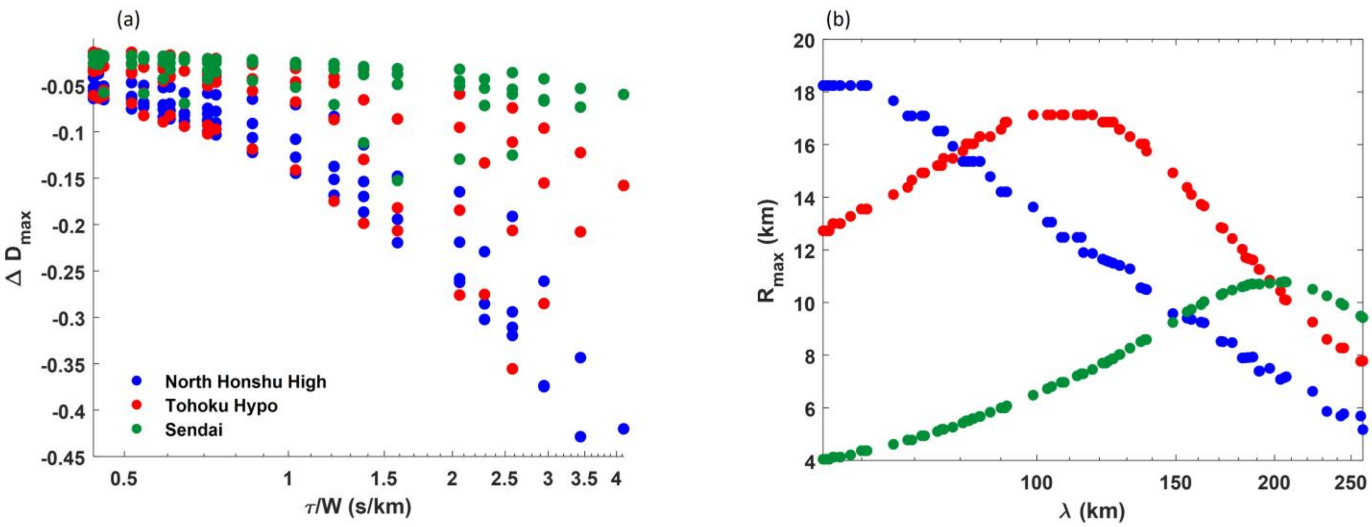

Figure 7: Inundation metrics for different bathymetric geometry. (a) ΔD_{max} (TD-NH vs IS-NH) at the first point on the coast for the profiles referred to as “North Honshu High”, “Tohoku Hypo” and “Sendai” respectively according to the map in Figure 1(c). (b) maximum run-up R_{max} (for IS-NH case) as a function of horizontal source extension λ for the 3 bathymetric profiles following the same legend of panel (a).

Figure 7(a) shows the $|\Delta D_{max}|$ between IS-NH and TD-NH source simulations at the first point on the coast, for all the simulations and for the 3 different profiles. We retrieved for all the bathymetries the double trend evidenced in Section 3.1 with larger discrepancy emerging not only for slower ruptures but also for large size sources. However, a flatter bathymetry leads to smaller $|\Delta D_{max}|$ implying that when a tsunami wave propagates towards more gentle depth variation an instantaneous source would produce inundation scenarios more similar to time-dependent sources as compared to steeper environments. Contemporarily, in a flatter environment, the inundation is attenuated both in terms of flow-depth on the coast and maximum run-up with the size of resonance that increases as the bathymetry slope decreases (see Figure 7b). For the sake of clarity, this latter panel only shows the trends for the IS-NH case. However, we verified that, for all the bathymetries, the rupture size for which the resonance occurs is independent of both the source treatment (IS or TD) and the choice of propagation regime (NH or SW, compared with Figure 6c).
In conclusion, a gentler slope of the coast, as in the case of the flood plains in the area of Sendai-Fukushima selects a longer wavelength component of tsunami waves, generating less intense inundations in terms of both flow-depth on the coast and maximum run-up. Moreover, in a

Tohoku-like environment, like the one we have modelled in this study, the longer wavelengths are more controlled by the deformation occurring very close to the hypocenter (Satake et al., 2013). This contributes to reduce the discrepancy between IS and TD simulations for the flatter bathymetric profiles.

5 Discussion

5.1 Comparison with real earthquakes and tsunamis

To understand in which cases time dependent and/or non-hydrostatic effects should be considered, the 81 simulations performed for the "Tohoku Hypo" bathymetry (intermediate slope) are plotted in Figure 8(a) as a function of their source slowness τ/W and size λ. They are classified depending on whether the parameter ΔR_{max} (TD-NH vs IS-NH) is larger (red dots) or smaller (orange and green dots) than 0.1, considering as acceptable a relative discrepancy smaller than 10%. The source slowness and size are related to seismic parameters like the stress drop, the average rigidity and hence the average depth of the source (Bilek & Lay, 1999; Geist & Bilek, 2001; Sallarès & Ranero, 2019). As expected, the slower the rupture the more time-dependent rupture modelling is needed. The instantaneous approximation tends to fail when the characteristic tsunami propagation speed at the source, on the order of $\sqrt{gH_{trench}}$ (with H_{trench} being the depth at the trench) is comparable with the rupture velocity V_r, for which the quantity $(\tau/W)^{-1}$ acts as a proxy (e.g. see Abrahams et al., 2023), as it occurs for the slowest ruptures considered here. However, beyond that, we found that the ΔR_{max} (TD-NH vs IS-NH) also depends on the source size. Indeed, larger ruptures, for which along-dip distance is comparable with trench-coast distance, more likely lead to inaccurate solutions from approximated models. In these cases, the inundation is more controlled by what happens at the source rather than by the propagation processes (e.g., the shoaling).
To provide modelers with tangible recommendations, we compared the parameters of the sources presented in Figure 8(a) with those inferred for some subduction interface tsunamigenic earthquakes . Their features are summarized in Table S3 of Supporting Information. We extracted the duration τ, the width W and the dip angle from the teleseismic data inversions by Ye et al. (2016), for all the events, including the Maule 2010 Mw 8.8 and the Tohoku-Oki 2011 Mw 9.1 earthquakes, with the exception of the 2004 Sumatra-Andaman earthquake, whose parameters are taken from the finite-fault model summary released by USGS (https://earthquake.usgs.gov/earthquakes/eventpage/official20041226005853450_30/finite-fault, Banerjee et al. 2007). We computed a proxy of the source size along the dip as $\lambda = W \cdot \cos\delta$, with δ being the dip angle (See Table S3 in Supporting Information). Such a comparison in Figure 8 has the goal of comparing the characteristic space and time scales of simulations with those of the real events. However, single real events might be also affected by specific conditions related to local geometry, shallow structure, bathymetry variation, and ratio between source size and trench-coast distance as it happens for the Maule 2010 earthquake (Romano et al., 2020), which may differ from the Tohoku-like setup used in our 1D simulations. Hence, this comparison should be regarded as a general indication. Nonetheless, according to this comparison, some of the megathrust events, characterized by relatively shallow slip and not too high stress-drop, such as Maule 2010 and Tohoku 2011, are very close to the accuracy limit to use an instantaneous source, while the 2004 Sumatra-Andaman event is well in the region where instantaneous source modelling leads to inaccurate solutions and a time-dependent source should be used. The use of a TD source implies, in turn, the necessity of a NH regime to avoid the spurious oscillations shown

in Figures S12 and S15 (in Supporting Information) and the consequent systematic SW overestimation evidenced in Figures 6(c) and 6(d).
Conversely, large stress drop events (relatively rapid ones, sometimes referred to as "snappy" earthquakes, see e.g. Ebeling & Okal, 2012; Okal et al., 2016) can be well modelled with an instantaneous source. Finally, earthquakes featuring a small extension along the dip, might lead to larger errors when modelled by an instantaneous source, if they are characterized by very slow ruptures, like the tsunami earthquakes (small values of stress drop and rigidity). However, a direct comparison between the findings of this study and tsunami earthquakes must be interpreted with some prudence, since such events are characterized by a quite large along-strike extension as compared to their width (Kanamori, 1971; Tanioka & Satake, 1996a; Tanioka & Seno, 2001). Such a feature cannot be considered in the 1D model and will be the scope of future work.
Lastly, In Figure 8(a) the orange dots represent the simulations for which ΔR_{max} (TD-NH vs IS-NH) < 0.1 while ΔR_{max} (TD-NH vs TD-SW) > 0.1. Such simulations are characterized by a small source extension ($\lambda \sim 7H_{trench}$) and, although they could be modelled through an IS description, they require a NH modelling to avoid exceeding the imposed discrepancy tolerance. Within this region we retrieve very short-sized interslab events like the 2009 Papua event or the Tohoku foreshock of 2011, March 9th. In such a case, even if metrics like the maximum run-up are accurately modelled through an IS approach, a TD source must be used to prevent the short wavelength oscillations affecting the dispersive secondary waves (See red curves in Figure S14 in Supporting Information). For the same reason, for faster events (e.g. deeper, larger stress drop earthquakes for which $\sqrt{gH} \cdot \tau / W \ll 1$), that can be precisely simulated with an IS, the choice of a SW modelling represents a preferable option (see green regions in Figure 8).

We have verified that ΔD_{max} or ΔR_{max} depend also on topographic features (see Figure 7a). Figure 8(b) shows the same plot as Figure 8(a) with the ΔR_{max} values, but using the flatter "Sendai" near-coast bathymetry and topography. As shown in Figure 7(a), the ΔD_{max} values on the coast are smaller for flatter bathymetries and this leads to smaller Δ values also in terms of maximum run-up. As a consequence, only very slow ($V_r < 0.5\ km/s$) and large ruptures (λ larger than half trench-coast distance) yield inaccurate inundation modelling when an IS source is used as a tsunami generation mechanism. Only the modelling of events similar to the giant 2004 Sumatra event would require a TD source. The differences highlighted between Figures 8(a) and (b) are consistent with the results related to the 2011 Tohoku-Oki event, by Satake et al. (2013) who showed how a time-dependent source modelling is required to accurately retrieve the inundation features along the coast in front of the hypocenter of the event. Satake et al., (2013) also showed that an instantaneous source was enough to model a realistic inundation in the southern regions of Sendai and Fukushima. For flatter bathymetries, for which the shortest wavelength sources generate negligible inundations, all the ΔR_{max} (TD-NH-vs TD-SW) values are below the imposed tolerance of 0.1. For the sake of completeness, the results summarized in Figure 8 are compared with the condition $W/\tau = 2\sqrt{gH_{trench}}$ that represents a proxy of the instantaneous source limit (Abrahams et al., 2023). An equivalent horizontal line fixing as a reference a SW limit $\lambda = 2H_{trench}$ would be well below the shortest modelled source.

At least for a Tohoku-like up-dip rupture, using an instantaneous source always overestimates the inundation on the coast as compared to the corresponding time dependent modelling. Therefore, for some applications, the IS can be still used as a conservative approach, even though relatively inaccurate, if a kinematic or a dynamic realistic description of the seismic source process is not available. Nevertheless, we have also verified that for some simulations the maximum amplitude of waves propagating towards the open ocean along the directive direction is underestimated by the IS modelling. This might produce an underestimated inundation warning towards those islands which are located along the up-dip direction, in the vicinity of the trench.

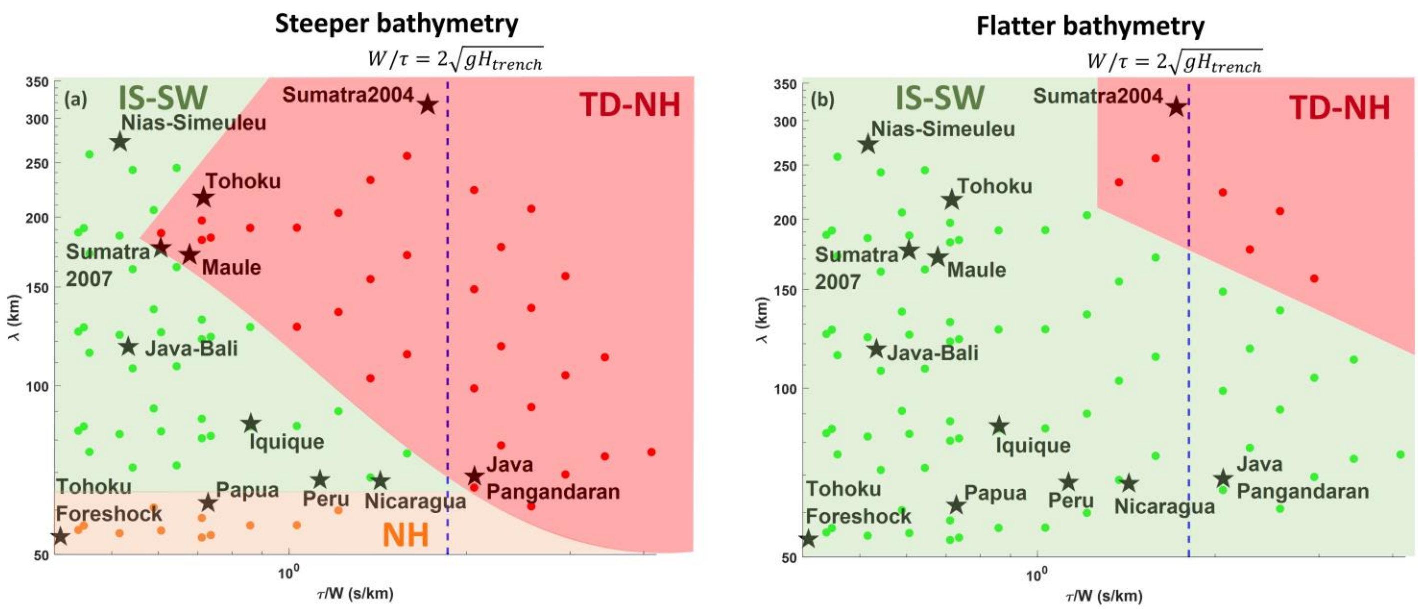

Figure 8: Summary of simulations that can be modelled with (green dots) and without (red and orange dots) enough accuracy using simplified models in terms of maximum run-up R. In all panels, each simulation is placed according to τ/W and λ with the green and red dots representing $|\Delta R_{max}| \leq 0.1$ and $|\Delta R_{max}| > 0.1$ respectively when the comparison (TD-NH vs IS-NH) is performed. Orange dots represent the simulations for which ΔR_{max} (TD-NH vs IS-NH) < 0.1 while ΔR_{max} (TD-NH vs TD-SW) > 0.1 The colored regions indicate the regions where different models must be used. The blue dashed lines border the regions where the seismic rupture velocity proxy W/τ is equal to 2 times the maximum tsunami velocity at the source $\sqrt{gH_{trench}}$. Panels (a) and (b) refer to simulations performed on an intermediate slope ("Tohoku Hypo") and flat slope bathymetry geometry ("Sendai"), respectively.

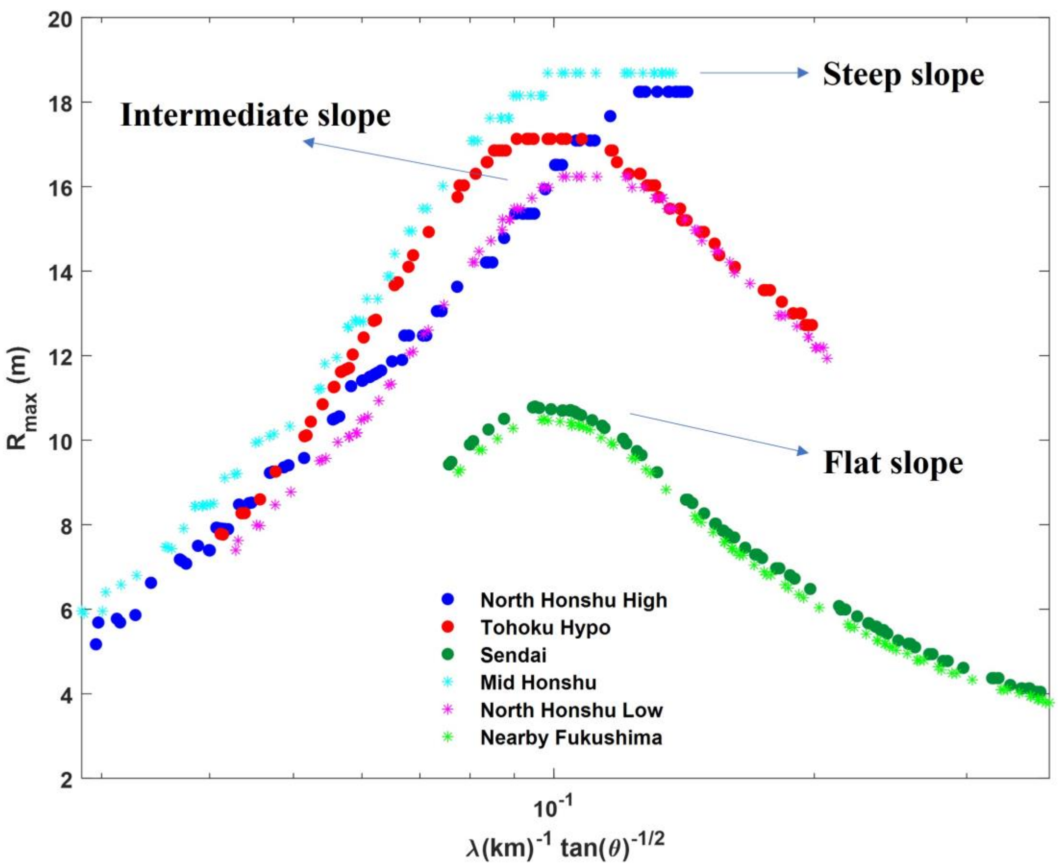

Figure 9: maximum run-up as a function of $1/\left(\lambda\sqrt{\tan\theta}\right)$ as suggested by the model of Stefanakis et al. (2012). As indicated by the arrows the blue dots and cyan stars refer to steeper slope geometry, the red dots and magenta stars to intermediate slope and the dark green dots and green stars to flatter slope bathymetry, respectively, as reported in the legend.

5.2 Resonance

Another important result concerns the size of the resonance observed in the computation of maximum run-up and its connection to the geometry of bathymetric profiles. In this framework, Stefanakis et al. (2012) have shown how a monochromatic source, with pulsation ω, generates resonant waves whose maximum run-up on planar beaches depends on the incident wavelength and beach slope (with larger run-ups associated with steeper slopes). They verified that for a fixed beach length L the resonance is always retrieved at the same normalized pulsation $\omega' = \omega/\sqrt{g\tan\theta/L}$, with g and θ being the gravity acceleration and the slope of the bathymetry (in the vicinity of the beach and inland), respectively. To verify the consistency of the same model for our application, we can replace ω with $1/\lambda$ since in the vicinity of the source the depth variation and hence the propagation velocity are the same for all the bathymetries. Moreover, we can neglect the effect of L because the beaches are always long enough to avoid backward reflections. Figure 9 shows the maximum run-up R_{max} for all the 81 IS-NH simulations and the 6 bathymetries, as a function of the parameter $1/\left(\lambda\sqrt{\tan\theta}\right)$, θ being the different slopes of the bathymetry in the vicinity and on the coast. Although the sources modelled in this work are quite different as compared to the simplified monochromatic source, with characteristic wavelength inherited by a realistic parameterization of the seismic rupture, the resonant mechanism is preserved (compare Figure 9 with Figure 7c) at least for instantaneous sources. When a TD source is implemented this resonance symmetry is partially smeared since the maximum run-up is also controlled by the seismic source duration (See Figure 6c), with slower ruptures leading to smaller inundation. This latter result challenges the common assumption, for example, for tsunami earthquakes, that slow ruptures are one of the reasons why larger than expected tsunami inundation for a given earthquake magnitude is observed. Nevertheless, our modelling indicates that the inundation amplification could still be due to larger slip occurring at shallower depths, where the surrounding medium is weaker, and/or eventually to an unexpectedly large extension of the rupture along the strike direction.

5.3 Limits of numerical modelling

Some of the choices made in terms of seismic source parameters deserve further discussion since they can affect the investigated tsunami metrics. As an example, different values of the critical slip weakening distance D_c or the possibility to consider the contribution of horizontal sea-floor deformation (Tanioka & Satake, 1996b; Tanioka & Seno, 2001) to the tsunami initial condition might modify the maximum amplitude of the source time history (see Figure 1b) and hence generate different wave amplitudes, flow-depths, and maximum run-ups. Besides, as discussed in section 3.3, we used a single slope to model the interface between the fault and the seafloor for all the cases and this allowed us to perform several tsunami simulations from a single rupture dynamic model. However, the use of a different and more realistic interface geometry is expected to slightly change the wave amplitudes as an effect of the variable dip and its time history, even when ending up with the same residual amplitude (See Figure S16a in Supporting Information). Nevertheless, at least regarding the latter point, we verified for some of the performed simulations that the ranges of ΔD_{max} on the coast and the $\Delta\eta_{max}$ offshore values (for TD-NH vs IS-NH comparison) are not significantly affected by these initial source amplitude perturbations (See Figure S16 and its caption in Supporting Information). Therefore, we can argue that the results presented in section 4 as well as the general interpretation presented in this section hold for most of the conditions that simply affect the maximum amplitude of the waves triggered in the vicinity of the source.

We focused on megathrust earthquakes while tsunamis may arise also from other type of mechanisms such as the outer-rise normal events for which time-dependent and non-hydrostatic modelling might have a non-negligible effect as well (Baba et al., 2021). One should be cautious to extend the findings of this study to those events and related tsunamis because they feature different radiation fields and sea-floor deformation history and space scale.

Finally, more complex models, taking into account the solid-acoustic coupling at the elastic-fluid interface (e.g. Ma, 2022), more sophisticated dynamic effects, like bi-material slip amplification (e.g. Scala et al. 2017), off-fault damage dissipation (e.g. Wilson & Ma, 2021, Ma, 2023) and realistic, short-sized bathymetry features as the ones shown within the insets of Figure 1(c), may affect the results. All these physical complexities, even though well beyond the scope of this work, deserve a deeper investigation possibly in a fully 3D coupled seismic-tsunami source model.

6 Conclusions

The main goal of this work is to understand when the accuracy needed to model the earthquake source and tsunami generation can be achieved with the commonly adopted simplifications (e.g. instantaneous source, shallow water) that reduce the computational cost. This is crucial for applications like the PTHA (e.g., Grezio et al., 2017; Davies et al., 2018; Basili et al., 2021; Behrens et al., 2021), where many scenarios need to be simulated, and tsunami early warning (e.g., Selva et al., 2021), where a short time-to-solution is needed. We measured the accuracy of the solutions in terms of wave amplitude and inundation metrics (flow-depth and run-up) for a Tohoku-like test-case using different topo-bathymetric morphologies. We systematically compared the approximated results and the ones deriving from a more realistic representation of the physical processes, accounting for a time-dependent earthquake-tsunami source and/or a multi-layer non-hydrostatic tsunami modelling. We varied systematically the duration and the size of the tsunami sources, using realistic ranges related to the corresponding seismic source and surrounding medium parameters, in particular the stress drop and the rigidity around the fault plane.

The main results can be summarized as follows:

1. An instantaneous source leads to increasingly less accurate results as the velocity of the seismic source decreases and becomes comparable with the characteristic velocity of tsunami propagation, in turn proportional to the square root of the bathymetric depth. However, within this framework, the size of the rupture also plays a fundamental role with larger ruptures leading to less accurate solutions. The inundation metrics are systematically overestimated by the instantaneous source approximation.
2. For what concerns the comparison between shallow water and non-hydrostatic, in realistic conditions featuring an average bathymetric depth $H \ll \lambda$ (horizontal extension of the source) the discrepancy for the maximum wave amplitudes and inundations are often not significant. Even for very small ruptures the relative flow-depth and run-up overestimation from SW-IS as compared to NH-IS are always smaller than the 10%. Nevertheless, when we compare NH and SW in those conditions requiring TD source modelling, such discrepancy increases up to $\sim$20%. Thus, it is almost always recommended to use NH modeling when dealing with time dependent seismic ruptures. In this frame, the common use of multi sub-faults, activated at different instants, along with a SW propagation, might lead to large overestimation.
3. All the results presented depend on the geometric characteristics of the topo/bathymetry in the vicinity of the coast and inland. The differences between TD and IS inundation on flatter bathymetric profiles (e.g., the ones characterizing the flood plains) are smaller than those for steeper profiles. As a result, flooding on a flatter bathymetry could be modelled with sufficient accuracy as an instantaneous source, as has been shown for some real tsunamigenic events (Satake et al. 2013).
4. The maximum run-up features a resonant mechanism, that is an amplified R_{max} in correspondence of a narrow range of the source size λ. The size of resonance was shown

to be inversely proportional to $\sqrt{\tan\theta}$ with θ being the topo-bathymetry slope in the vicinity of the coastline.

5. Comparing all these results with real events, we found that megathrust and tsunami earthquakes might require non-hydrostatic time-dependent modelling, in particular for more pronounced variation of nearshore topo-bathymetry to prevent overestimation of inundation intensity. Conversely, tsunami generated by deeper higher stress drop seismic ruptures can be simulated through approximated IS-SW modelling, still preserving enough accuracy in terms of propagating waves and inundation features.

- **Acknowledgments**

This research has been partially funded by MCIN/AEI/10.13039/501100011033 and by the “European Union NextGenerationEU/PRTR" through the grant PDC2022-133663-C21 and by MCIN/AEI/10.13039/50110001103 and by “ERDF A way of making Europe”, by the European Union through the grant PID2022-137637NB-C21

Open Research

The whole simulated dataset is available at the following link: https://zenodo.org/doi/10.5281/zenodo.10497579

All the figures were originally produced for this paper through the software MATLAB: version 2023b. First accessed: September 2023. Academic license number: 40500131.

References

Abercrombie, R. E., Bannister, S., Ristau, J., & Doser, D. (2017). Variability of earthquake stress drop in a subduction setting, the Hikurangi Margin, New Zealand. *Geophysical Journal International*, *208*(1), 306–320. https://doi.org/10.1093/gji/ggw393

Abrahams, L. S., Krenz, L., Dunham, E. M., Gabriel, A.-A., & Saito, T. (2023). Comparison of methods for coupled earthquake and tsunami modelling. *Geophysical Journal International*, *234*(1), 404–426. https://doi.org/10.1093/gji/ggad053

Adsuara, J. E., Cordero-Carrión, I., Cerdá-Durán, P., & Aloy, M. A. (2016). Scheduled Relaxation Jacobi method: Improvements and applications. Journal of Computational Physics, 321, 369–413. https://doi.org/10.1016/j.jcp.2016.05.053

Audusse, E., Bristeau, M.-O., Perthame, B., & Sainte-Marie, J. (2011). A multilayer Saint-Venant system with mass exchanges for shallow water flows. Derivation and numerical validation. *ESAIM: Mathematical Modelling and Numerical Analysis*, *45*(1), 169–200. https://doi.org/10.1051/m2an/2010036

Baba, T., Chikasada, N., Imai, K., Tanioka, Y., & Kodaira, S. (2021). Frequency dispersion amplifies tsunamis caused by outer-rise normal faults. *Scientific Reports*, *11*(1), 20064. https://doi.org/10.1038/s41598-021-99536-x

Babeyko, A., Lorito, S., Hernandez, F., Lauterjung, J., Løvholt, F., Rudloff, A., Sørensen, M., Androsov, A., Aniel-Quiroga, I., Armigliato, A., Baptista, M. A., Baglione, E., Basili, R., Behrens, J., Brizuela, B., Bruni, S., Cambaz, D., Cantavella Nadal, J., Carillho, F., … Yalciner, A. (2022). Towards the new Thematic Core Service Tsunami within the EPOS Research Infrastructure. *Annals of Geophysics*, *65*(2), DM215. https://doi.org/10.4401/ag-8762

Banerjee, P., Pollitz, F., Nagarajan, B., & Bürgmann, R. (2007). Coseismic Slip Distributions of the 26 December 2004 Sumatra–Andaman and 28 March 2005 Nias Earthquakes from <scp>gps</scp> Static Offsets. *Bulletin of the Seismological Society of America*, *97*(1A), S86–S102. https://doi.org/10.1785/0120050609

Basili, R., Brizuela, B., Herrero, A., Iqbal, S., Lorito, S., Maesano, F. E., Murphy, S., Perfetti, P., Romano, F., Scala, A., Selva, J., Taroni, M., Tiberti, M. M., Thio, H. K., Tonini, R., Volpe, M., Glimsdal, S., Harbitz, C. B., Løvholt, F., … Zaytsev, A. (2021). The Making of the NEAM Tsunami Hazard Model 2018 (NEAMTHM18). *Frontiers in Earth Science*, *8*. https://doi.org/10.3389/feart.2020.616594

Behrens, J., Løvholt, F., Jalayer, F., Lorito, S., Salgado-Gálvez, M. A., Sørensen, M., Abadie, S., Aguirre-Ayerbe, I., Aniel-Quiroga, I., Babeyko, A., Baiguera, M., Basili, R., Belliazzi, S., Grezio, A., Johnson, K., Murphy, S., Paris, R., Rafliana, I., De Risi, R., … Vyhmeister, E. (2021). Probabilistic Tsunami Hazard and Risk Analysis: A Review of Research Gaps. *Frontiers in Earth Science*, *9*. https://doi.org/10.3389/feart.2021.628772

Beji, S., & Battjes, J. A. (1994). Numerical simulation of nonlinear wave propagation over a bar. Coastal Engineering, 23(1–2), 1–16. https://doi.org/10.1016/0378-3839(94)90012-4

Bilek, S. L., & Lay, T. (1999). Rigidity variations with depth along interplate megathrust faults in subduction zones. *Nature*, *400*(6743), 443–446. https://doi.org/10.1038/22739

Bilek, S. L., Rotman, H. M. M., & Phillips, W. S. (2016). Low stress drop earthquakes in the rupture zone of the 1992 Nicaragua tsunami earthquake. *Geophysical Research Letters*, *43*(19). https://doi.org/10.1002/2016GL070409

Bonaventura, L., Fernández-Nieto, E. D., Garres-Díaz, J., & Narbona-Reina, G. (2018). Multilayer shallow water models with locally variable number of layers and semi-implicit time discretization. *Journal of Computational Physics*, *364*, 209–234. https://doi.org/10.1016/j.jcp.2018.03.017

Brocchini, M., & Peregrine, D. H. (1996). Integral flow properties of the swash zone and averaging. *Journal of Fluid Mechanics*, *317*, 241–273. https://doi.org/10.1017/S0022112096000742

Burridge, R. (1973). Admissible Speeds for Plane-Strain Self-Similar Shear Cracks with Friction but Lacking Cohesion. *Geophysical Journal International*, *35*(4), 439–455. https://doi.org/10.1111/j.1365-246X.1973.tb00608.x

Castro Díaz, M. J., & Fernández-Nieto, E. (2012). A Class of Computationally Fast First Order Finite Volume Solvers: PVM Methods. SIAM Journal on Scientific Computing, 34(4), A2173–A2196. https://doi.org/10.1137/100795280

Casulli, V. (1999). A semi-implicit finite difference method for non-hydrostatic, free-surface flows. *International Journal for Numerical Methods in Fluids*, *30*(4), 425–440. https://doi.org/10.1002/(SICI)1097-0363(19990630)30:4<425::AID-FLD847>3.0.CO;2-D

Chazel, F., Lannes, D., & Marche, F. (2011). Numerical Simulation of Strongly Nonlinear and Dispersive Waves Using a Green–Naghdi Model. Journal of Scientific Computing, 48(1–3), 105–116. https://doi.org/10.1007/s10915-010-9395-9

Chorin, A. J. (1968). Numerical Solution of the Navier-Stokes Equations. Mathematics of Computation, 22(104), 745. https://doi.org/10.2307/2004575

Davies, G., & Griffin, J. (2020). Sensitivity of Probabilistic Tsunami Hazard Assessment to Far-Field Earthquake Slip Complexity and Rigidity Depth-Dependence: Case Study of Australia. *Pure and Applied Geophysics*, *177*(3), 1521–1548. https://doi.org/10.1007/s00024-019-02299-w

Davies, G., Griffin, J., Løvholt, F., Glimsdal, S., Harbitz, C., Thio, H. K., Lorito, S., Basili, R., Selva, J., Geist, E., & Baptista, M. A. (2018). A global probabilistic tsunami hazard assessment from earthquake sources. *Geological Society, London, Special Publications*, *456*(1), 219–244. https://doi.org/10.1144/SP456.5

Davies, G., Weber, R., Wilson, K., & Cummins, P. (2022). From offshore to onshore probabilistic tsunami hazard assessment via efficient Monte Carlo sampling. *Geophysical Journal International*, *230*(3), 1630–1651. https://doi.org/10.1093/gji/ggac140

Dingemans, M. W. (1994). MAST PROJECT 1: WAVES G8-M Comparison of computations with Boussinesq-like models and laboratory measurements.

Ebeling, C. W., & Okal, E. A. (2012). An extension of the E/M0 tsunami earthquake discriminant Θ to regional distances. *Geophysical Journal International*, *190*(3), 1640–1656. https://doi.org/10.1111/j.1365-246X.2012.05566.x

Ehara, A., Salmanidou, D. M., Heidarzadeh, M., & Guillas, S. (2023). Multi-level emulation of tsunami simulations over Cilacap, South Java, Indonesia. *Computational Geosciences*, *27*(1), 127–142. https://doi.org/10.1007/s10596-022-10183-1

Escalante, C., Fernández-Nieto, E. D., Garres-Díaz, J., & Mangeney, A. (2023). Multilayer Shallow Model for Dry Granular Flows with a Weakly Non-hydrostatic Pressure. *Journal of Scientific Computing*, *96*(3), 88. https://doi.org/10.1007/s10915-023-02299-y

Escalante, C., Fernández-Nieto, E. D., Garres-Díaz, J., Morales de Luna, T., & Penel, Y. (2023). Non-hydrostatic layer-averaged approximation of Euler system with enhanced dispersion properties. *Computational and Applied Mathematics*, *42*(4), 177. https://doi.org/10.1007/s40314-023-02309-7

Escalante, C., Fernández-Nieto, E. D., Morales de Luna, T., & Castro, M. J. (2019). An Efficient Two-Layer Non-hydrostatic Approach for Dispersive Water Waves. *Journal of Scientific Computing*, *79*(1), 273–320. https://doi.org/10.1007/s10915-018-0849-9

Escalante, C., Morales de Luna, T., & Castro, M. J. (2018). Non-hydrostatic pressure shallow flows: GPU implementation using finite volume and finite difference scheme. *Applied Mathematics and Computation*, *338*, 631–659. https://doi.org/10.1016/j.amc.2018.06.035

Fernández-Nieto, E. D., Koné, E. H., & Chacón Rebollo, T. (2014). A Multilayer Method for the Hydrostatic Navier-Stokes Equations: A Particular Weak Solution. *Journal of Scientific Computing*, *60*(2), 408–437. https://doi.org/10.1007/s10915-013-9802-0

Fernández-Nieto, E. D., Parisot, M., Penel, Y., & Sainte-Marie, J. (2018). A hierarchy of dispersive layer-averaged approximations of Euler equations for free surface flows. *Communications in Mathematical Sciences*, *16*(5), 1169–1202. https://doi.org/10.4310/CMS.2018.v16.n5.a1

Festa, G., & Vilotte, J.-P. (2005). The Newmark scheme as velocity-stress time-staggering: an efficient PML implementation for spectral element simulations of elastodynamics.

Geophysical Journal International, *161*(3), 789–812. https://doi.org/10.1111/j.1365-246X.2005.02601.x

Folesky, J., Kummerow, J., & Shapiro, S. A. (2021). Stress Drop Variations in the Region of the 2014 M_W 8.1 Iquique Earthquake, Northern Chile. *Journal of Geophysical Research: Solid Earth*, *126*(4). https://doi.org/10.1029/2020JB020112

Gailler, A., Hébert, H., Schindelé, F., & Reymond, D. (2018). Coastal Amplification Laws for the French Tsunami Warning Center: Numerical Modeling and Fast Estimate of Tsunami Wave Heights Along the French Riviera. *Pure and Applied Geophysics*, *175*(4), 1429–1444. https://doi.org/10.1007/s00024-017-1713-9

Geist, E. L., & Bilek, S. L. (2001). Effect of depth-dependent shear modulus on tsunami generation along subduction zones. *Geophysical Research Letters*, *28*(7), 1315–1318. https://doi.org/10.1029/2000GL012385

Gibbons, S. J., Lorito, S., Macías, J., Løvholt, F., Selva, J., Volpe, M., Sánchez-Linares, C., Babeyko, A., Brizuela, B., Cirella, A., Castro, M. J., de la Asunción, M., Lanucara, P., Glimsdal, S., Lorenzino, M. C., Nazaria, M., Pizzimenti, L., Romano, F., Scala, A., … Vöge, M. (2020). Probabilistic Tsunami Hazard Analysis: High Performance Computing for Massive Scale Inundation Simulations. *Frontiers in Earth Science*, *8*. https://doi.org/10.3389/feart.2020.591549

Glimsdal, S., Løvholt, F., Harbitz, C. B., Romano, F., Lorito, S., Orefice, S., Brizuela, B., Selva, J., Hoechner, A., Volpe, M., Babeyko, A., Tonini, R., Wronna, M., & Omira, R. (2019). A New Approximate Method for Quantifying Tsunami Maximum Inundation Height Probability. *Pure and Applied Geophysics*, *176*(7), 3227–3246. https://doi.org/10.1007/s00024-019-02091-w

Gopinathan, D., Heidarzadeh, M., & Guillas, S. (2021). Probabilistic quantification of tsunami current hazard using statistical emulation. *Proceedings of the Royal Society A: Mathematical, Physical and Engineering Sciences*, *477*(2250). https://doi.org/10.1098/rspa.2021.0180

Grezio, A., Babeyko, A., Baptista, M. A., Behrens, J., Costa, A., Davies, G., Geist, E. L., Glimsdal, S., González, F. I., Griffin, J., Harbitz, C. B., LeVeque, R. J., Lorito, S., Løvholt, F., Omira, R., Mueller, C., Paris, R., Parsons, T., Polet, J., … Thio, H. K. (2017). Probabilistic Tsunami Hazard Analysis: Multiple Sources and Global Applications. *Reviews of Geophysics*, *55*(4), 1158–1198. https://doi.org/10.1002/2017RG000579

Hayes, G. P., Moore, G. L., Portner, D. E., Hearne, M., Flamme, H., Furtney, M., & Smoczyk, G. M. (2018). Slab2, a comprehensive subduction zone geometry model. *Science*, *362*(6410), 58–61. https://doi.org/10.1126/science.aat4723

Huang, Y., Meng, L., & Ampuero, J.-P. (2012). A dynamic model of the frequency-dependent rupture process of the 2011 Tohoku-Oki earthquake. *Earth, Planets and Space*, *64*(12), 1061–1066. https://doi.org/10.5047/eps.2012.05.011

Ida, Y. (1972). Cohesive force across the tip of a longitudinal-shear crack and Griffith's specific surface energy. *Journal of Geophysical Research*, *77*(20), 3796–3805. https://doi.org/10.1029/JB077i020p03796

Kajiura, K. (1963). The leading wave of a tsunami. *Bulletin of Earthquake Research Institute, University of Tokyo*, *41*, 535–571.

Kanamori, H. (1971). Seismological evidence for a lithospheric normal faulting — the Sanriku earthquake of 1933. *Physics of the Earth and Planetary Interiors*, *4*(4), 289–300. https://doi.org/10.1016/0031-9201(71)90013-6

Kanamori, H., & Brodsky, E. E. (2004). The physics of earthquakes. *Reports on Progress in Physics*, *67*(8), 1429–1496. https://doi.org/10.1088/0034-4885/67/8/R03

Kazolea, M., & Delis, A. I. (2013). A well-balanced shock-capturing hybrid finite volume–finite difference numerical scheme for extended 1D Boussinesq models. Applied Numerical Mathematics, 67, 167–186. https://doi.org/10.1016/j.apnum.2011.07.003

Komatitsch, D., & Vilotte, J.-P. (1998). The spectral element method: An efficient tool to simulate the seismic response of 2D and 3D geological structures. *Bulletin of the Seismological Society of America*, *88*(2), 368–392. https://doi.org/10.1785/BSSA0880020368

Kozdon, J. E., & Dunham, E. M. (2013). Rupture to the Trench: Dynamic Rupture Simulations of the 11 March 2011 Tohoku Earthquake. *Bulletin of the Seismological Society of America*, *103*(2B), 1275–1289. https://doi.org/10.1785/0120120136

LeVeque, R. J., Waagan, K., González, F. I., Rim, D., & Lin, G. (2016). Generating Random Earthquake Events for Probabilistic Tsunami Hazard Assessment. *Pure and Applied Geophysics*, *173*(12), 3671–3692. https://doi.org/10.1007/s00024-016-1357-1

Li, L., Lay, T., Cheung, K. F., & Ye, L. (2016). Joint modeling of teleseismic and tsunami wave observations to constrain the 16 September 2015 Illapel, Chile, M_w 8.3 earthquake rupture process. *Geophysical Research Letters*, *43*(9), 4303–4312. https://doi.org/10.1002/2016GL068674

Lotto, G. C., & Dunham, E. M. (2015). High-order finite difference modeling of tsunami generation in a compressible ocean from offshore earthquakes. *Computational Geosciences*, *19*(2), 327–340. https://doi.org/10.1007/s10596-015-9472-0

Lotto, G. C., Jeppson, T. N., & Dunham, E. M. (2019). Fully Coupled Simulations of Megathrust Earthquakes and Tsunamis in the Japan Trench, Nankai Trough, and Cascadia Subduction Zone. *Pure and Applied Geophysics*, *176*(9), 4009–4041. https://doi.org/10.1007/s00024-018-1990-y

Ludwig, W. J., Nafe, J. E., & Drake, C. L. (1970). Seismic refraction New York: Wiley-Interscience. *The Sea, Edited by Maxwell, A. E.*, *4*(1), 53–84.

Ma, G., Shi, F., & Kirby, J. T. (2012). Shock-capturing non-hydrostatic model for fully dispersive surface wave processes. *Ocean Modelling*, *43–44*, 22–35. https://doi.org/10.1016/j.ocemod.2011.12.002

Ma, S. (2022). Dynamic off-fault failure and tsunamigenesis at strike-slip restraining bends: Fully-coupled models of dynamic rupture, ocean acoustic waves, and tsunami in a shallow bay. *Tectonophysics*, *838*, 229496. https://doi.org/10.1016/j.tecto.2022.229496

Ma, S. (2023). Wedge plasticity and a minimalist dynamic rupture model for the 2011 MW 9.1 Tohoku-Oki earthquake and tsunami. *Tectonophysics*, *869*, 230146. https://doi.org/10.1016/j.tecto.2023.230146

Macías, J., Escalante, C., & Castro, M. J. (2021a). Multilayer-HySEA model validation for landslide-generated tsunamis – Part 1: Rigid slides. *Natural Hazards and Earth System Sciences*, *21*(2), 775–789. https://doi.org/10.5194/nhess-21-775-2021

Macías, J., Escalante, C., & Castro, M. J. (2021b). Multilayer-HySEA model validation for landslide-generated tsunamis – Part 2: Granular slides. *Natural Hazards and Earth System Sciences*, *21*(2), 791–805. https://doi.org/10.5194/nhess-21-791-2021

Makinoshima, F., Oishi, Y., Yamazaki, T., Furumura, T., & Imamura, F. (2021). Early forecasting of tsunami inundation from tsunami and geodetic observation data with convolutional neural networks. *Nature Communications*, *12*(1), 2253. https://doi.org/10.1038/s41467-021-22348-0

Meade, B. J. (2007). Algorithms for the calculation of exact displacements, strains, and stresses for triangular dislocation elements in a uniform elastic half space. *Computers & Geosciences*, *33*(8), 1064–1075. https://doi.org/10.1016/j.cageo.2006.12.003

Miyake, H., Koketsu, K., & Furumura, T. (2008). *SOURCE MODELING OF SUBDUCTION-ZONE EARTHQUAKES AND LONG-PERIOD GROUND MOTION VALIDATION IN THE TOKYO METROPOLITAN AREA*.

Murphy, S., Di Toro, G., Romano, F., Scala, A., Lorito, S., Spagnuolo, E., Aretusini, S., Festa, G., Piatanesi, A., & Nielsen, S. (2018). Tsunamigenic earthquake simulations using experimentally derived friction laws. *Earth and Planetary Science Letters*, *486*, 155–165. https://doi.org/10.1016/j.epsl.2018.01.011

Murphy, S., Scala, A., Herrero, A., Lorito, S., Festa, G., Trasatti, E., Tonini, R., Romano, F., Molinari, I., & Nielsen, S. (2016). Shallow slip amplification and enhanced tsunami hazard unravelled by dynamic simulations of mega-thrust earthquakes. *Scientific Reports*, *6*(1), 35007. https://doi.org/10.1038/srep35007

Nakano, M., Murphy, S., Agata, R., Igarashi, Y., Okada, M., & Hori, T. (2020). Self-similar stochastic slip distributions on a non-planar fault for tsunami scenarios for megathrust earthquakes. *Progress in Earth and Planetary Science*, *7*(1), 45. https://doi.org/10.1186/s40645-020-00360-0

Oglesby, D. D., Archuleta, R. J., & Nielsen, S. B. (2000). Dynamics of dip-slip faulting: Explorations in two dimensions. *Journal of Geophysical Research: Solid Earth*, *105*(B6), 13643–13653. https://doi.org/10.1029/2000JB900055

Okada, Y. (1985). Surface deformation due to shear and tensile faults in a half-space. *Bulletin of the Seismological Society of America*, *75*(4), 1135–1154. https://doi.org/10.1785/BSSA0750041135

Okal, E. A., Kirby, S. H., & Kalligeris, N. (2016). The Showa Sanriku earthquake of 1933 March 2: a global seismological reassessment. *Geophysical Journal International*, *206*(3), 1492–1514. https://doi.org/10.1093/gji/ggw206

Ricchiuto, M., & Filippini, A. G. (2014). Upwind residual discretization of enhanced Boussinesq equations for wave propagation over complex bathymetries. Journal of Computational Physics, 271, 306–341. https://doi.org/10.1016/j.jcp.2013.12.048

Roeber, V., Cheung, K. F., & Kobayashi, M. H. (2010). Shock-capturing Boussinesq-type model for nearshore wave processes. *Coastal Engineering*, *57*(4), 407–423. https://doi.org/10.1016/j.coastaleng.2009.11.007

Romano, F., Gusman, A. R., Power, W., Piatanesi, A., Volpe, M., Scala, A., & Lorito, S. (2021). Tsunami Source of the 2021 M_W 8.1 Raoul Island Earthquake From DART and Tide-Gauge Data Inversion. *Geophysical Research Letters*, *48*(17). https://doi.org/10.1029/2021GL094449

Romano, F., Lorito, S., Lay, T., Piatanesi, A., Volpe, M., Murphy, S., & Tonini, R. (2020). Benchmarking the Optimal Time Alignment of Tsunami Waveforms in Nonlinear Joint Inversions for the Mw 8.8 2010 Maule (Chile) Earthquake. *Frontiers in Earth Science, 8*. https://doi.org/10.3389/feart.2020.585429

Saito, T., Baba, T., Inazu, D., Takemura, S., & Fukuyama, E. (2019). Synthesizing sea surface height change including seismic waves and tsunami using a dynamic rupture scenario of anticipated Nankai trough earthquakes. *Tectonophysics, 769*, 228166. https://doi.org/10.1016/j.tecto.2019.228166

Sallarès, V., & Ranero, C. R. (2019). Upper-plate rigidity determines depth-varying rupture behaviour of megathrust earthquakes. *Nature*, *576*(7785), 96–101. https://doi.org/10.1038/s41586-019-1784-0

Satake, K., Fujii, Y., Harada, T., & Namegaya, Y. (2013). Time and Space Distribution of Coseismic Slip of the 2011 Tohoku Earthquake as Inferred from Tsunami Waveform Data. *Bulletin of the Seismological Society of America*, *103*(2B), 1473–1492. https://doi.org/10.1785/0120120122

Scala, A., Festa, G., Vilotte, J. -P., Lorito, S., & Romano, F. (2019). Wave Interaction of Reverse-Fault Rupture With Free Surface: Numerical Analysis of the Dynamic Effects and Fault Opening Induced by Symmetry Breaking. *Journal of Geophysical Research: Solid Earth*, *124*(2), 1743–1758. https://doi.org/10.1029/2018JB016512

Scala, A., Festa, G., & Vilotte, J.-P. (2017). Rupture dynamics along bimaterial interfaces: a parametric study of the shear-normal traction coupling. *Geophysical Journal International*, ggw489. https://doi.org/10.1093/gji/ggw489

Scala, A., Lorito, S., Romano, F., Murphy, S., Selva, J., Basili, R., Babeyko, A., Herrero, A., Hoechner, A., Løvholt, F., Maesano, F. E., Perfetti, P., Tiberti, M. M., Tonini, R., Volpe, M., Davies, G., Festa, G., Power, W., Piatanesi, A., & Cirella, A. (2020). Effect of Shallow Slip Amplification Uncertainty on Probabilistic Tsunami Hazard Analysis in Subduction Zones: Use of Long-Term Balanced Stochastic Slip Models. *Pure and Applied Geophysics*, *177*(3), 1497–1520. https://doi.org/10.1007/s00024-019-02260-x

Scala, A. (2024). Dataset repository for paper "On the relation between seismic source dynamics, tsunami generation and propagation, and numerical modelling complexity for large earthquakes in subduction zones" [Data set]. Zenodo. https://doi.org/10.5281/zenodo.10497580

Selva, J., Lorito, S., Volpe, M., Romano, F., Tonini, R., Perfetti, P., Bernardi, F., Taroni, M., Scala, A., Babeyko, A., Løvholt, F., Gibbons, S. J., Macías, J., Castro, M. J., González-Vida, J. M., Sánchez-Linares, C., Bayraktar, H. B., Basili, R., Maesano, F. E., … Amato, A. (2021). Probabilistic tsunami forecasting for early warning. *Nature Communications*, *12*(1), 5677. https://doi.org/10.1038/s41467-021-25815-w

Sepúlveda, I., Liu, P. L. -F., Grigoriu, M., & Pritchard, M. (2017). Tsunami hazard assessments with consideration of uncertain earthquake slip distribution and location. *Journal of Geophysical Research: Solid Earth*, *122*(9), 7252–7271. https://doi.org/10.1002/2017JB014430

Skarlatoudis, A. A., Somerville, P. G., & Thio, H. K. (2016). Source-Scaling Relations of Interface Subduction Earthquakes for Strong Ground Motion and Tsunami Simulation. *Bulletin of the Seismological Society of America*, *106*(4), 1652–1662. https://doi.org/10.1785/0120150320

Souty, V., & Gailler, A. (2021). Fast High-Resolution S-PTHA Along the Western Mediterranean Sea Coastlines. Application to the Bay of Cannes. *Frontiers in Earth Science*, *9*. https://doi.org/10.3389/feart.2021.765610

Stefanakis, T., Dias, F., & Dutykh, D. (2012). Resonant Long-Wave Run-Up On A Plane Beach. *Proceedings of the 22nd (2012) International Offshore and Polar Engineering Conference*, 116–121. https://hal.science/hal-00728747

Stoker J. J. (1992). *Water Waves: The Mathematical Theory with Applications*. Wiley Classic Library.

Strasser, F. O., Arango, M. C., & Bommer, J. J. (2010). Scaling of the Source Dimensions of Interface and Intraslab Subduction-zone Earthquakes with Moment Magnitude. *Seismological Research Letters*, *81*(6), 941–950. https://doi.org/10.1785/gssrl.81.6.941

Sugawara, D. (2021). Numerical modeling of tsunami: advances and future challenges after the 2011 Tohoku earthquake and tsunami. *Earth-Science Reviews*, *214*, 103498. https://doi.org/10.1016/j.earscirev.2020.103498

Takahashi, N., Kodaira, S., Tsuru, T., Park, J.-O., Kaneda, Y., Suyehiro, K., Kinoshita, H., Abe, S., Nishino, M., & Hino, R. (2004). Seismic structure and seismogenesis off Sanriku region, northeastern Japan. *Geophysical Journal International*, *159*(1), 129–145. https://doi.org/10.1111/j.1365-246X.2004.02350.x

Tanioka, Y., & Satake, K. (1996a). Fault parameters of the 1896 Sanriku Tsunami Earthquake estimated from Tsunami Numerical Modeling. *Geophysical Research Letters*, *23*(13), 1549–1552. https://doi.org/10.1029/96GL01479

Tanioka, Y., & Satake, K. (1996b). Tsunami generation by horizontal displacement of ocean bottom. *Geophysical Research Letters*, *23*(8), 861–864. https://doi.org/10.1029/96GL00736

Tanioka, Y., & Seno, T. (2001). Sediment effect on tsunami generation of the 1896 Sanriku Tsunami Earthquake. *Geophysical Research Letters*, *28*(17), 3389–3392. https://doi.org/10.1029/2001GL013149

Titov, V. V., & Synolakis, C. E. (1995). Modeling of Breaking and Nonbreaking Long-Wave Evolution and Runup Using VTCS-2. Journal of Waterway, Port, Coastal, and Ocean Engineering, 121(6), 308–316. https://doi.org/10.1061/(ASCE)0733-950X(1995)121:6(308)

Tonini, R., Basili, R., Maesano, F. E., Tiberti, M. M., Lorito, S., Romano, F., Scala, A., & Volpe, M. (2020). Importance of earthquake rupture geometry on tsunami modelling: the Calabrian Arc subduction interface (Italy) case study. *Geophysical Journal International*, *223*(3), 1805–1819. https://doi.org/10.1093/gji/ggaa409

Uenishi, K., & Rice, J. R. (2003). Universal nucleation length for slip-weakening rupture instability under nonuniform fault loading. *Journal of Geophysical Research: Solid Earth*, *108*(B1). https://doi.org/10.1029/2001JB001681

Venkataraman, A., & Kanamori, H. (2004). Observational constraints on the fracture energy of subduction zone earthquakes. *Journal of Geophysical Research: Solid Earth*, *109*(B5). https://doi.org/10.1029/2003JB002549

Williamson, A. L., Rim, D., Adams, L. M., LeVeque, R. J., Melgar, D., & González, F. I. (2020). A Source Clustering Approach for Efficient Inundation Modeling and Regional Scale Probabilistic Tsunami Hazard Assessment. *Frontiers in Earth Science*, *8*. https://doi.org/10.3389/feart.2020.591663

Wilson, A., & Ma, S. (2021). Wedge Plasticity and Fully Coupled Simulations of Dynamic Rupture and Tsunami in the Cascadia Subduction Zone. *Journal of Geophysical Research: Solid Earth*, *126*(7). https://doi.org/10.1029/2020JB021627

Yamada, N., & Iwata, T. (2005). Long-period ground motion simulation in the Kinki area during the MJ 7.1 foreshock of the 2004 off the Kii peninsula earthquakes. *Earth, Planets and Space*, *57*(3), 197–202. https://doi.org/10.1186/BF03351815

Ye, L., Lay, T., Kanamori, H., & Rivera, L. (2016). Rupture characteristics of major and great ($M_w \geq 7.0$) megathrust earthquakes from 1990 to 2015: 1. Source parameter scaling relationships. *Journal of Geophysical Research: Solid Earth*, *121*(2), 826–844. https://doi.org/10.1002/2015JB012426

Yoshimoto, M., & Yamanaka, Y. (2014). Teleseismic inversion of the 2004 Sumatra-Andaman earthquake rupture process using complete Green's functions. *Earth, Planets and Space*, *66*(1), 152. https://doi.org/10.1186/s40623-014-0152-4

AGU PUBLICATIONS

Journal of Geophysical Research: Oceans

Supporting Information for

On the relation between seismic source dynamics, tsunami generation and propagation, and numerical modelling complexity in subduction zones

A. Scala[1,2], S. Lorito[2], C. Escalante Sanchez[3], F. Romano[2], G. Festa[1,2], A. Abbate[2,4], H. B. Bayraktar[2], M. J. Castro[3], J. Macias[3], J. M. Gonzalez-Vida[3]

[1] Department of Physics "Ettore Pancini", University Federico II, Napoli, 80126, Italy.

[2] Istituto Nazionale di Geofisica e Vulcanologia, Rome, 00143, Italy

[3]EDANYA Group, University of Malaga, Malaga, 29080, Spain

[4]Department of Mathematics and Geosciences, University of Trieste, 34128, Italy

Contents of this file

Additional Supporting Information (Files uploaded separately)

Introduction

Within the following Supporting Information we include:

- a more detailed description of the tsunami numerical modelling scheme along with the validation of the presented scheme against some standard benchmark test
- 16 Figures to support the results presented in the main text
- 3 Tables summarizing:
    - Sampled seismic source parameters
    - Seismic source parameters selected for each simulation (only caption, Table S2 in a separate file)
    - Seismic source parameterization for real events reported in Figure 8
- 10 captions for the movie included to Supporting Information as separate files. The movies represent the animated wave evolution of simulations whose snapshots are plotted in Figures 2 and 3 (in the main text) and S12, S14 and S15 (in Supporting Information).

Text S1 Tsunami numerical modelling

We briefly describe the numerical discretization of system in equations (3)-(5) in the main text assuming a constant split of the layers $l_\alpha = 1/L$. Here, we follow the procedure described in Escalante et al. (2019). The numerical scheme is based on a two-step projection-correction method, similar to the standard Chorin's projection method for Navier-Stokes equations (Chorin, 1968). That is a standard procedure when dealing with dispersive systems (see Ma et al., 2012; Kazolea & Delis, 2013; Ricchiuto & Filippini, 2014; Escalante et al., 2018, 2019 and references therein).
First, we shall solve the non-conservative hydrostatic underlying system in equation (3) given by the compact equation:

$$\partial_t \mathbf{U} + \partial_x \mathbf{F}(\mathbf{U}) + \mathbf{B}(\mathbf{U})\partial_x \mathbf{U} + \mathbf{G}(\mathbf{U})\partial_x \eta = 0 \qquad (S1)$$

where the following compact notation has been used:

$$\mathbf{U} = \begin{pmatrix} h \\ hu_1 \\ \vdots \\ hu_L \\ hw_1 \\ \vdots \\ hw_L \end{pmatrix},\ \mathbf{F}(\mathbf{U}) = \begin{pmatrix} hu \\ u_1 hu_1 \\ \vdots \\ u_L hu_L \\ u_1 hw_1 \\ \vdots \\ u_L hu_L \end{pmatrix},\ \mathbf{G}(\mathbf{U}) = \begin{pmatrix} 0 \\ gh \\ \vdots \\ gh \\ 0 \\ \vdots \\ 0 \end{pmatrix}, \qquad (S2)$$

and $\boldsymbol{B}$ is a matrix such $\boldsymbol{B}\partial_x U$ contains the non-conservative products related to the mass transfer across interfaces appearing at the momentum equations.
Then, in a second step, the non-hydrostatic terms from the right-hand side of equations (3) collected by the pressure vector.

$$\mathcal{T}(h, \partial_x h, z_b, \partial_x z_b, \mathbf{P}, \partial_x \mathbf{P}) = -L \begin{pmatrix} 0 \\ \frac{1}{2} h_1 \partial_x (p_{3/2} + p_{1/2}) - (p_{3/2} - p_{1/2}) \partial_x z_1 \\ \vdots \\ \frac{1}{2} h_L \partial_x \left(0 + p_{L-\frac{1}{2}}\right) - \left(0 - p_{L-\frac{1}{2}}\right) \partial_x z_L \\ h_1 (p_{3/2} - p_{1/2}) \\ \vdots \\ h_L \left(0 - p_{L-\frac{1}{2}}\right) \end{pmatrix}, \quad \mathbf{P} = \begin{pmatrix} p_{1/2} \\ p_{3/2} \\ \vdots \\ p_{L-1/2} \end{pmatrix} \tag{S3}$$

as well as the divergence constraints at each layer given in equation (5) will be taken into account. Concerning the constraints, we will equivalently impose

$$\mathcal{B}_\alpha = 0, \text{ where } \mathcal{B}_1 = \mathcal{I}_1,\ \mathcal{B}_2 = \mathcal{I}_2 - \mathcal{I}_1,\ \dots,\ \mathcal{B}_L = \mathcal{I}_L - \mathcal{I}_{L-1} \tag{S4}$$

so that the divergence impositions read as follows:

$$\mathcal{B}\left(\mathbf{U}^{(k)}, \partial_x \mathbf{U}^{(k)}, z_b, \partial_x z_b\right) =$$

$$\begin{pmatrix} -h_1 \partial_x (h_1 u_1) + 2\partial_x z_1 h_1 u_1 - 2h_1 w_1 + 2h_1 \partial_t z_b \\ -h_2 \partial_x (h_2 u_2) - h_1 \partial_x (h_1 u_1) + 2h_2 u_2 \partial_x z_2 - 2h_1 u_1 \partial_x z_1 - 2h_2 w_2 + 2h_1 w_1 \\ \vdots \\ -h_L \partial_x (h_L u_L) - h_{L-1} \partial_x (h_{L-1} u_{L-1}) + 2h_L u_L \partial_x z_L - 2h_{L-1} u_{L-1} \partial_x z_{L-1} - 2h_L w_L + 2h_{L-1} w_{L-1} \end{pmatrix}. \tag{S5}$$

System in eq. (S1) is discretized using a second-order finite volume PVM positive-preserving well-balanced path-conservative method (Castro Díaz & Fernández-Nieto, 2012). As usual, we consider a set of N finite volume cells $I_i = [x_{(i-1/2)}\ , x_{(i+1/2)}]$ with constant lengths Δx and define:

$$\mathbf{U}_i(t) = \frac{1}{\Delta x} \int_{I_i} \mathbf{U}\,(x, t)\; dx \tag{S6}$$

the cell average of the function $U(x, t)$ on cell I_i at time t. Concerning non-hydrostatic terms, we consider mid-points x_i of each cell I_i and denote the point values of the function P at time t by:

$$\mathbf{P}_i(t) = \begin{pmatrix} p_{1/2}(x_i,t) \\ p_{3/2}(x_i,t) \\ \vdots \\ p_{L-1/2}(x_i,t) \end{pmatrix}. \tag{S7}$$

Non-hydrostatic terms will be approximated by second-order compact finite differences. Let us detail the time stepping procedure followed. Assume given time steps Δt^n , and denote $t^n = \sum_{k\le n} \Delta t^k$. To obtain second-order accuracy in time, the two-stage second-order TVD Runge-Kutta scheme is adopted. At the kth stage, $k \in \{1,2\}$, the two-step projection-correction method is given by:

$$\begin{aligned} \frac{\mathbf{U}^{(\tilde{k})} - \mathbf{U}^{(k-1)}}{\Delta t} + \partial_x \mathbf{F}(\mathbf{U}^{(k-1)}) + \mathbf{B}(\mathbf{U}^{(k-1)})\partial_x \mathbf{U}^{(k-1)} + \mathbf{G}(\mathbf{U}^{(k-1)})\partial_x z_b &= 0, \\ \frac{\mathbf{U}^{(k)} - \mathbf{U}^{(\tilde{k})}}{\Delta t} - \mathcal{T}(h^{(k)}, \partial_x h^{(k)}, z_b, \partial_x z_b, \mathbf{P}^{(k)}, \partial_x \mathbf{P}^{(k)}) &= 0 \\ \mathcal{B}(\mathbf{U}^{(k)}, \partial_x \mathbf{U}^{(k)}, z_b, \partial_x z_b) &= 0 \end{aligned} \tag{S8}$$

where $U^{(0)}$ is U at the time level t^n, $U^{(\tilde{k})}$ is an intermediate value in the two-step projection-correction method that contains the numerical solution of the hyperbolic system (S1) at the corresponding kth stage of the Runge-Kutta, and $U^{(k)}$ is the $k-th$ stage estimate. After that, a final value of the solution at the t^{n+1} time level is obtained:

$$\mathbf{U}^{n+1} = \frac{1}{2}\mathbf{U}^n + \frac{1}{2}\mathbf{U}^{(2)}. \tag{S9}$$

Observe that equations

(S8) require, at each stage of the calculation respectively, to solve a Poisson-like equation for each one of the variables contained in $P^{(k)}$. The resulting linear system is solved using an iterative Jacobi method combined with a scheduled relaxation (see Adsuara et al., 2016; Escalante et al., 2018, 2019). Note that the usual CFL restriction must be imposed for the computation of the time step Δt.

When friction with the bottom (τ_α^u), viscous shear stress $\left(K_{\alpha+1/2}\right)$, and the breaking model (τ_α^w) are considered, they will be computed semi-implicitly at the end of the second step of the projection-correction method at each kth stage of the TVD Runge-Kutta method as it is done in (Escalante et al., 2019). Note that the resolution of a straightforward tridiagonal system on the vertical for each volume I_i is exclusively required for the viscosity model. In contrast, the friction and breaking models can be considered by solving conventional algebraic problems, as is commonly the practice for friction models.

The resulting numerical scheme is well-balanced for the water at rest solution and is linearly L^∞-stable under the usual CFL condition related to the hydrostatic system. It is also worth mentioning that the numerical scheme is positive preserving and can deal with emerging topographies.

Text S2 Benchmark comparison

S2.1 Propagation of regular non-breaking waves over submerged bar

The experiments discussed in references (Beji & Battjes, 1994; Dingemans, 1994) conducted in a wave flume featuring a submerged trapezoidal bar, are well-known as a significant benchmark for dispersive models. In this test case, the spatial domain spans from 0 to 30 meters and includes a submerged trapezoidal obstacle, as depicted in Figure S3. The domain is discretized into cells with a constant length of Δx = 0.02 meters. An incident sinusoidal wave train is applied as a boundary condition on the left-hand side of the domain at x = 0 meters, following the approach described in (Escalante et al., 2019) with the following parameters:

$$\eta_l(t) = A \sin\left(\frac{2\pi}{T} t\right) \tag{S10}$$

where $A = 0.01$ meters and $T = 2.02$ seconds represent the amplitude and period, respectively. The remaining flow variables at $x = 0$ meters are set to zero. On the right side of the domain, free-outflow boundary conditions are enforced. The friction term is set to $n = 0.01$ in this test, and the CFL number is set to 0.9.

The resulting wave train is measured at eight wave gauge stations denoted as *WG1, WG2, . . . ,WG8* for the free-surface elevation η (see Figure S3). Figure S4 compares numerical simulations and experimental laboratory observations at various gauge points. Initially, we observe a good agreement for the two-layer model ($L = 2$) with the experimental data, and there is a slight improvement in results when the number of layers is increased to $L = 3$.

It's worth noting that we corroborate similar observations found in the literature, such as that in Ma et al. (2012) which utilizes σ-coordinates, or Escalante et al., (2019), where an enhanced two-layer version of the nonhydrostatic pressure multilayer system described here is employed. The findings in Chazel et al. (2011) with a three-parameter Green-Naghdi model optimized for uneven bottoms exhibit a comparable level of agreement.

S2.2 Solitary wave runup impinging on a plane beach

A classic test for dispersive shallow flows corresponds to the experimental setup by (Titov & Synolakis, 1995). Incident solitary waves of multiple relative amplitudes A/H^* were simulated to study propagation, breaking, and runup over a planar beach with a slope of 1:19.85 (corresponding to a bathymetry angle of about 2.9°). Experimental data are available in (Titov & Synolakis, 1995) for surface elevation at different times.

We consider the bathymetry of the problem as described in Figure 5. The computational domain [−15, 70] m is covered with cells of constant length $\Delta x = 0.01\,m$. The CFL number is set to 0.9, and free-outflow boundary conditions were imposed everywhere.

We begin by considering the initial condition for the model provided by a solitary wave of amplitude $A = 0.3m$ centered at point $x = 25m$ (see Escalante et al., 2018) for details on the expression of the solitary wave). In this case, a friction coefficient of n = 0.02 was used to account for the glass surface roughness effects appearing in the experiments. Figure S6 shows snapshots at different times, $t\sqrt{g/H^*} = t_0$. A good agreement between experimental and simulated

data is seen. We remark that wave breaking is observed at $t\sqrt{g/H^*} = 20$ and 25 during the experiment. The breaking criteria mechanism is mandatory, as it can be seen in Figure S7 where, independently of the number of layers, a nonphysical overshoot on the flow variables arise when waves start to break without any breaking dissipation mechanism as the one considered here.

Then, we consider the numerical simulation of solitary waves of different wave amplitudes $A = 0.1, A = 0.2, \ldots, A = 0.6\ m,$ and compute the maximum runup for each test case, and for different values of the Manning parameter $n = 0.013, n = 0.015, n = 0.02$ and $n = 0.025,$ and number of layers $L = 1, L = 3$. Furthermore, the numerical tests were run considering hydrostatic and non-hydrostatic pressure.

We then plot and compare the results with the experimental results given in (Titov & Synolakis, 1995) (See Figure S8). We first observe consistency on the computed numerically runup when considering different numbers of layers and hydrostatic or non-hydrostatic regimes. Moreover, we perform a sensitivity numerical analysis by considering a reasonable range for the Manning coefficient and observe good consistency in the runup results.

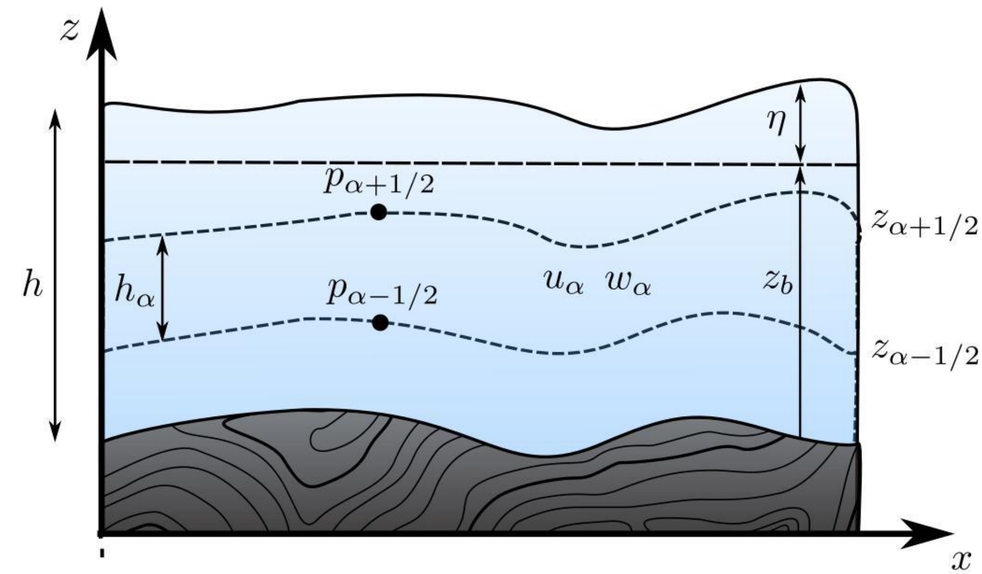

Figure S1. Schematic diagram describing the multilayer system

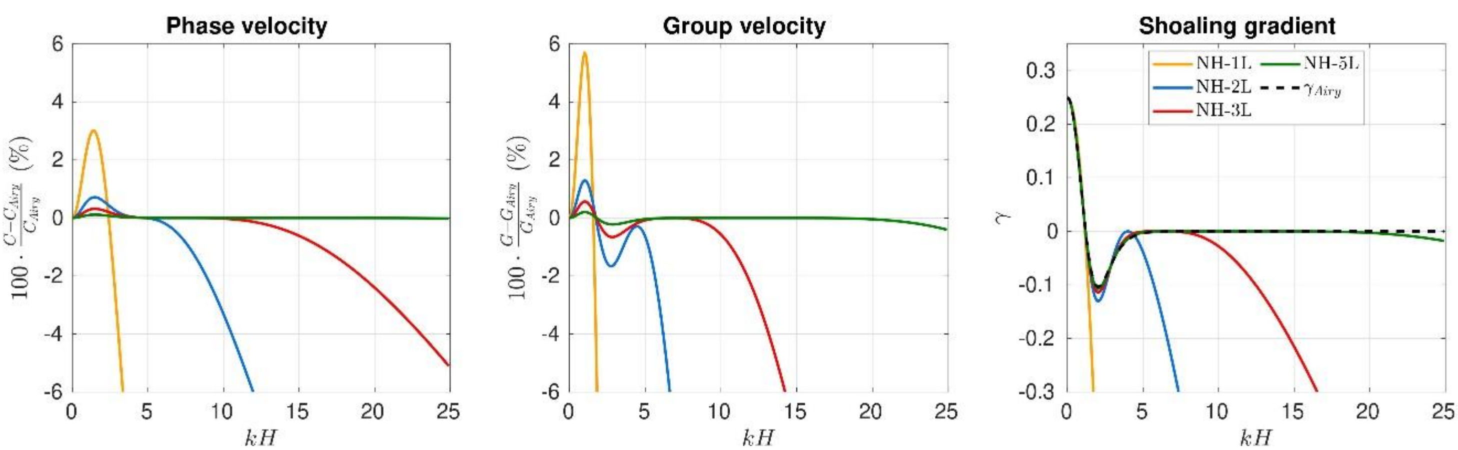

Figure S2. Relative error for the phase velocities (left), the group velocities (center), and comparison with the reference shoaling gradient (right), w.r.t. the Airy theory for NH-ML systems. NH-xL stands for NH-ML system with L = 1, 2, 3, 5 layers.

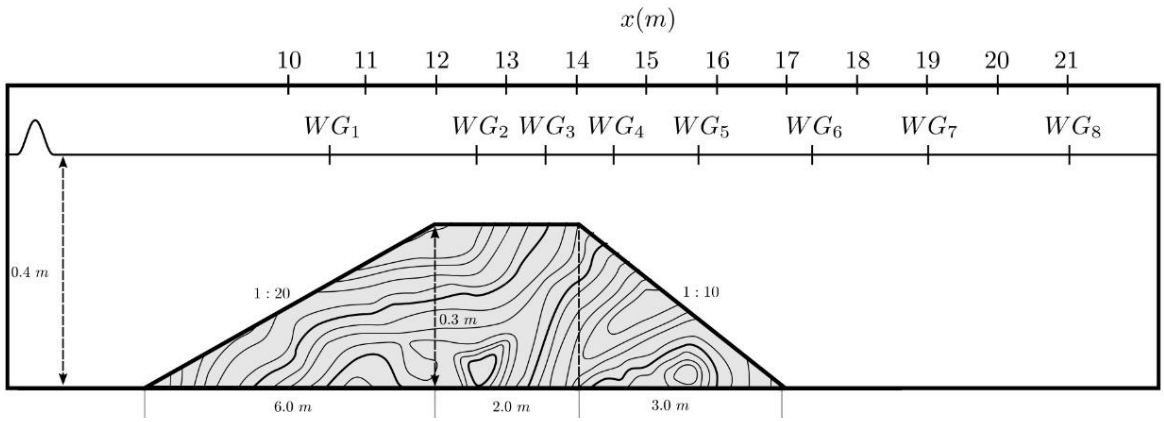

Figure S3. Periodic waves breaking over a submerged bar. Sketch of the topography and layout of the wave gauges

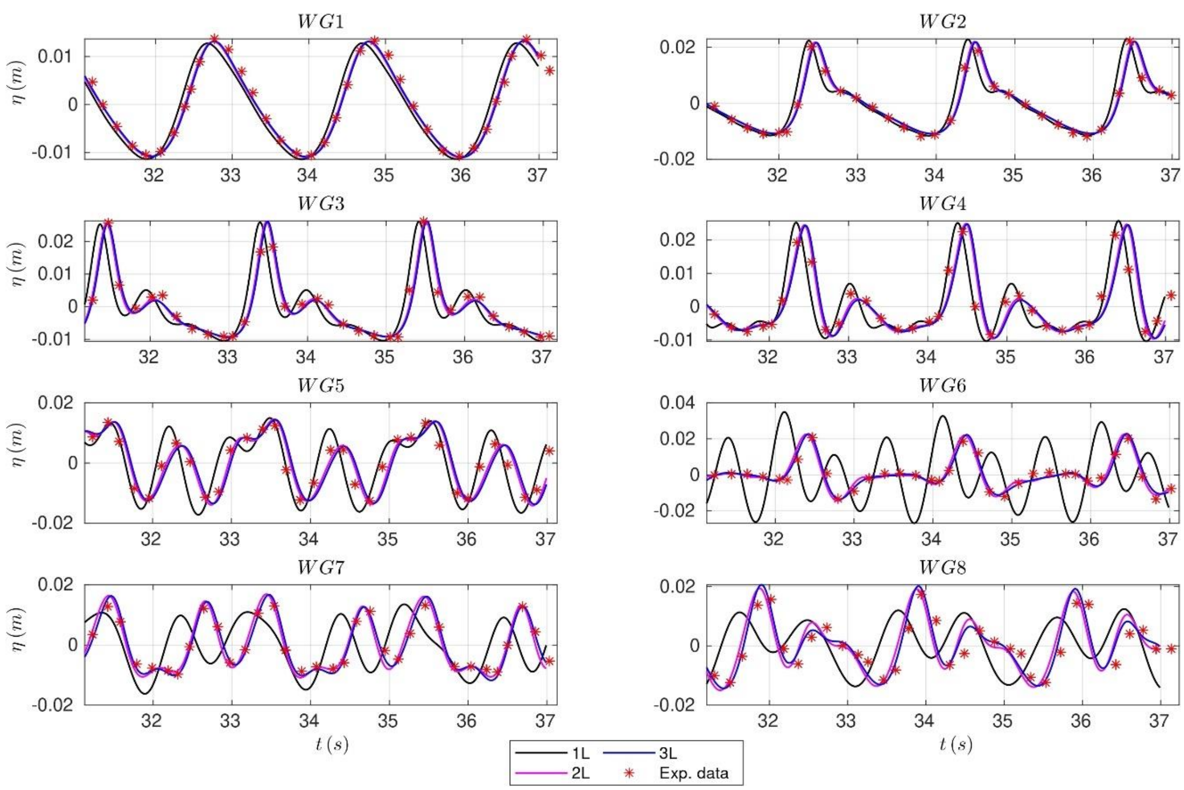

Figure S4. Comparison of data time series (red star points) and numerical values at wave gauges *WG1, WG2, WG3, WG4, WG5, WG6, WG7, WG8.*

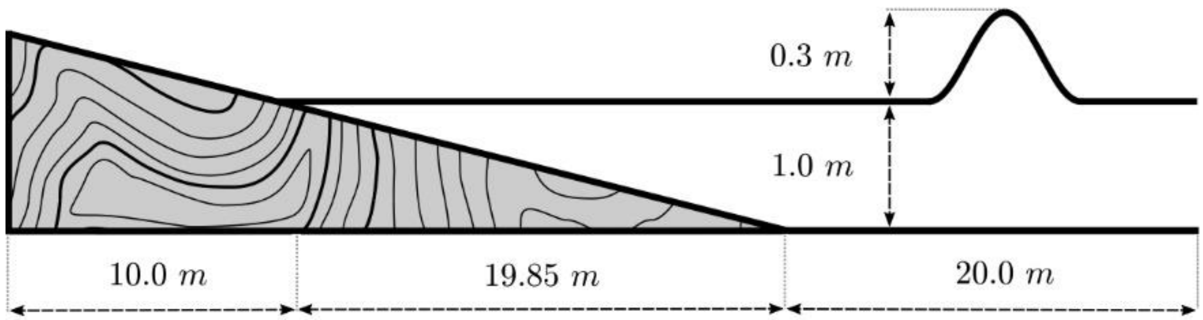

Figure S5. Sketch of the topography mimicking a beach

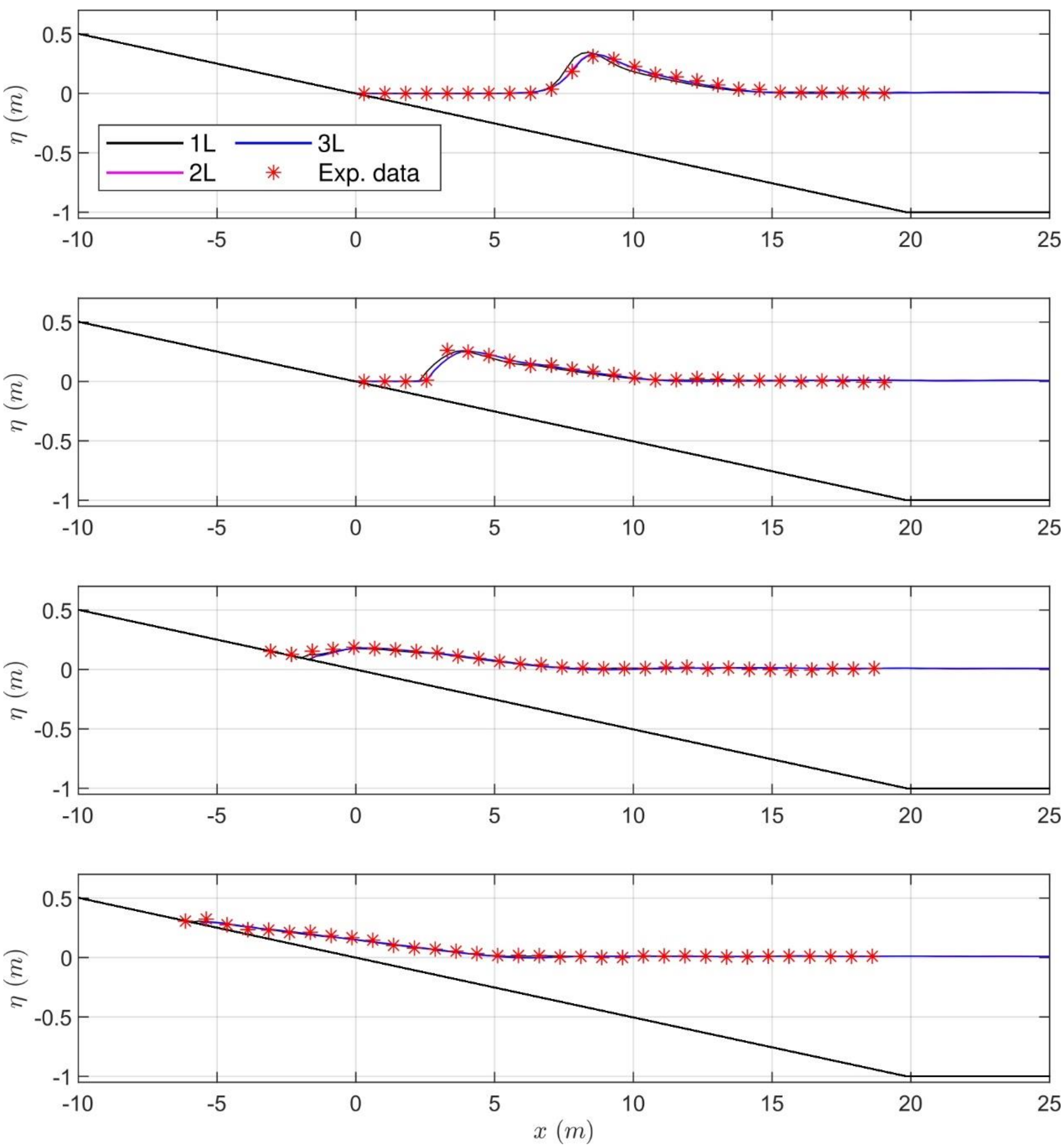

Figure S6. Comparison of experimental data (star points) and simulated ones (solid lines) at times $t\sqrt{g/H}\ = 15, 20, 25, 30$.

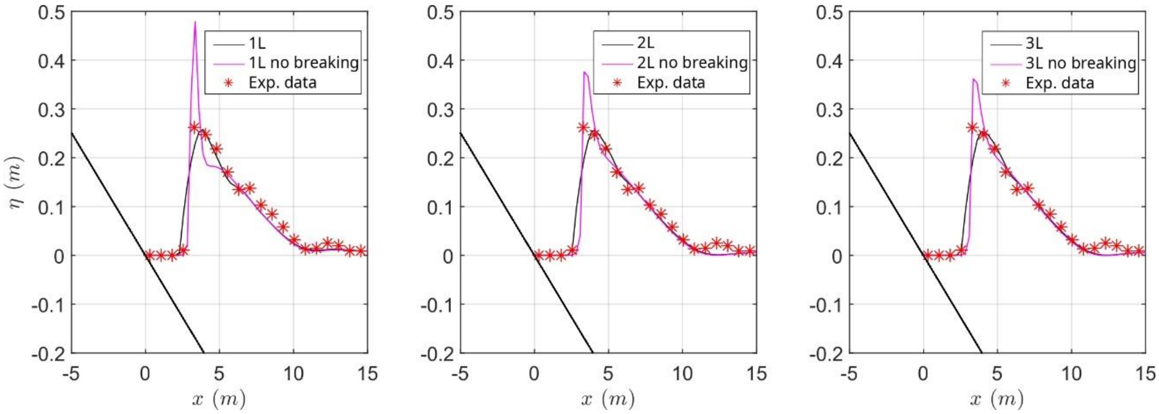

Figure S7. Comparison of experimental data (star points) and simulated ones (solid lines) at time $t\sqrt{g/H} = 20$

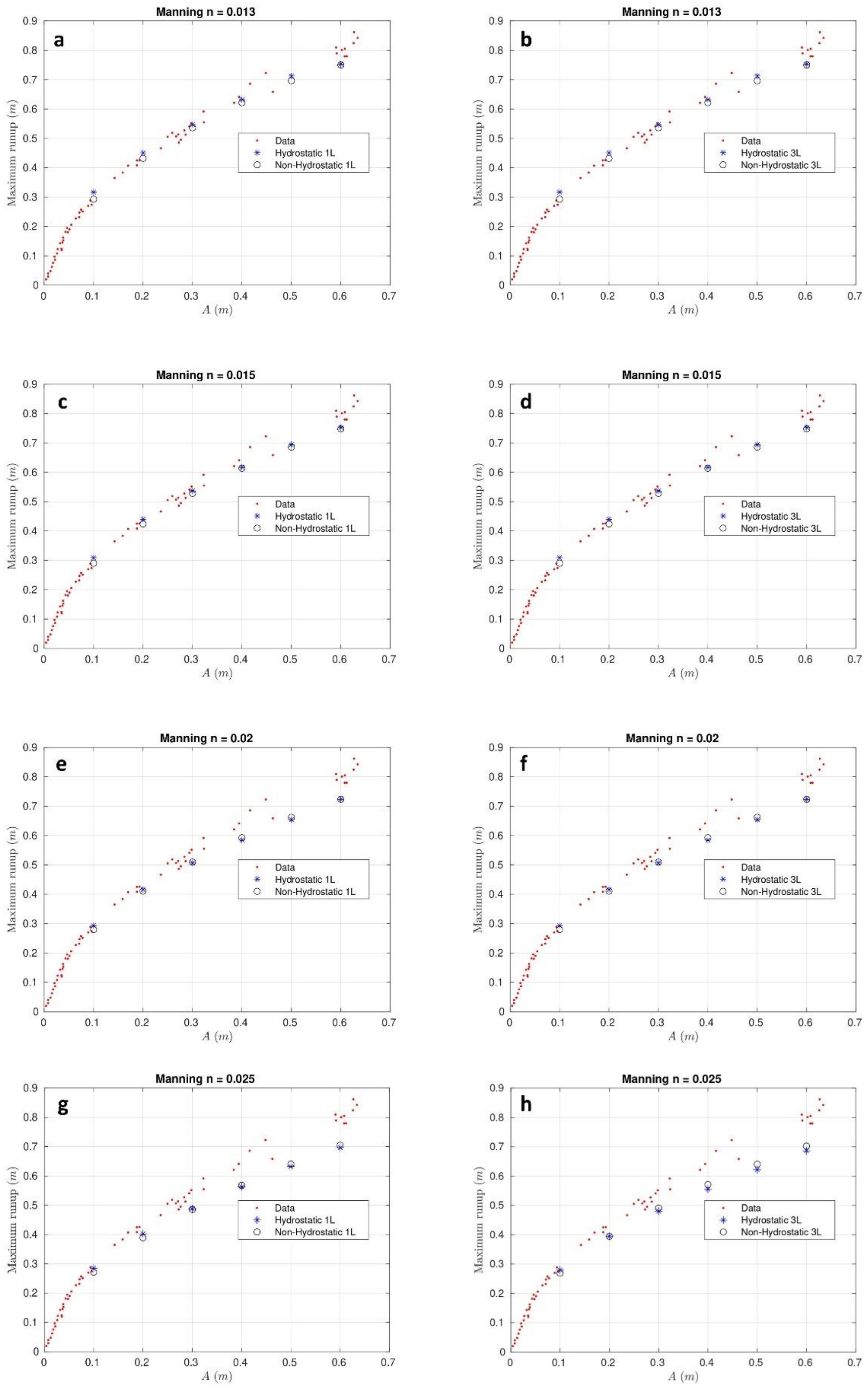
Manning n = 0.013
a
b
Manning n = 0.015
c
d
Manning n = 0.02
e
f
Manning n = 0.025
g
h
Maximum runup (m)
A (m)
Data
Hydrostatic 1L
Non-Hydrostatic 1L
Hydrostatic 3L
Non-Hydrostatic 3L

Figure S8. Experimental maximum runup (red points) and numerically computed maximum runups. A sensitivity numerical study considering different numbers of layers (1L a-c-e-g, 3L b-d-f-h), Manning coefficient n (0.013, 0.015, 0.02 and 0.025 for panels a-b, c-d, e-f, g-h respectively), and pressure regimes (Hydrostatic Non-Hydrostatic).

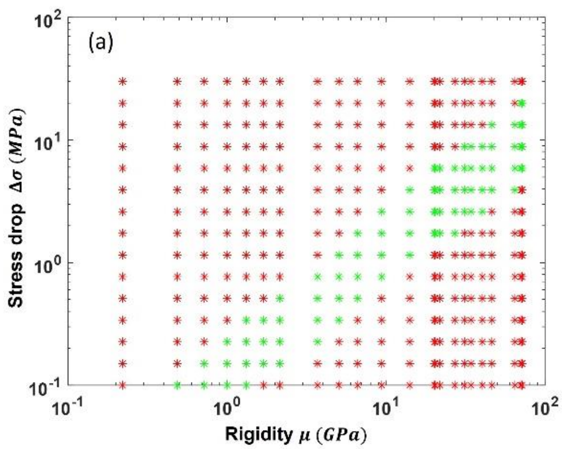

Figure S9. Parameters of the set of the simulated sources. (a) Stress drop and rigidity for all the possible combination of parameters in Table S1. Green stars represent the 81 selected simulations (See Table S2) while the red stars indicate the discarded ones according to the parametric choices described in Section 3. (b) The 81 selected simulations are plotted accordingly to their duration τ and width W.

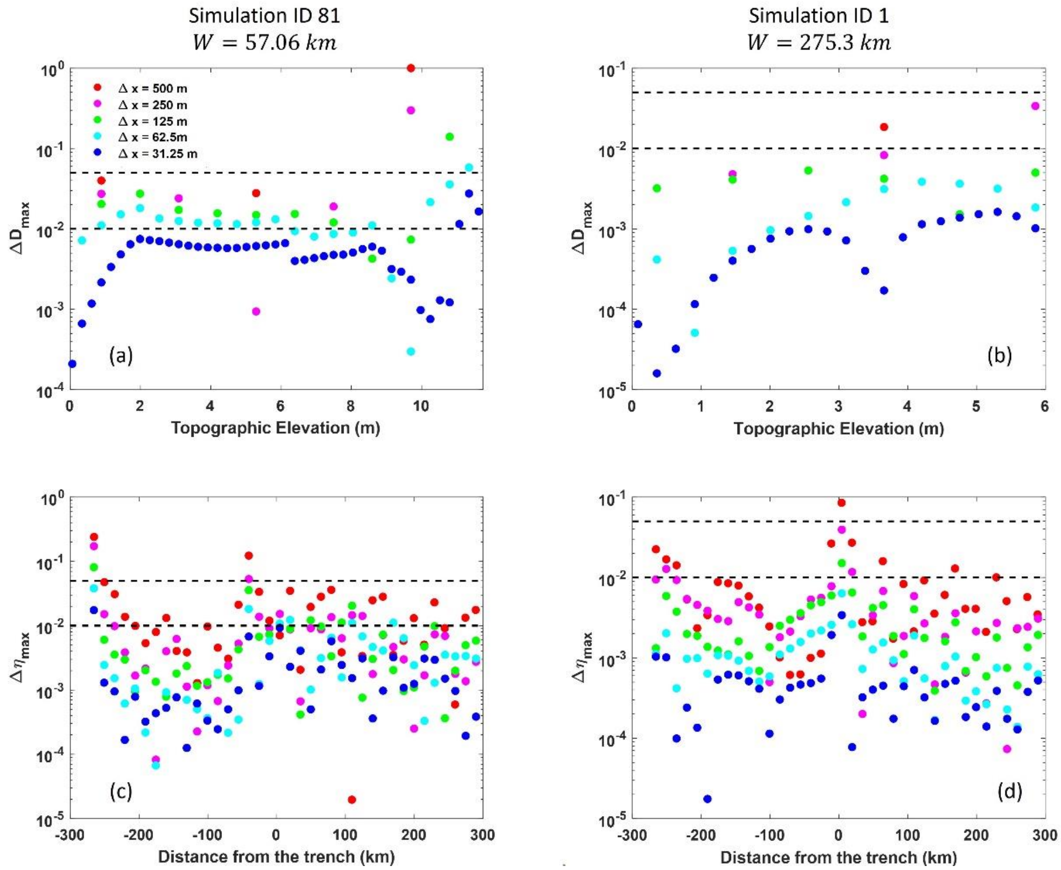

Figure S10. Results of convergence tests. (a) and (b): ΔD_{max} computed with respect to the reference grid ($\Delta x = 15.625\ m$) at different topographic elevation up to the maximum run-up for simulation ID 81 and 1 respectively. Different colors refer to different grids as indicated in the legend within the panel (a). The black dashed lines represent $\Delta D_{max} = 0.01$ and $\Delta D_{max} = 0.05$ levels. (c) and (d): $\Delta \eta_{max}$ computed with respect to the reference grid ($\Delta x = 15.625\ m$) at different distances from the trench both rightward and leftward (towards to the coast) from the source, for simulation ID 81 and 1 respectively. Different colors refer to different grids as indicated in the legend within the panel (a). The black dashed lines represent $\Delta \eta_{max} = 0.01$ and $\Delta \eta_{max} = 0.05$ levels.

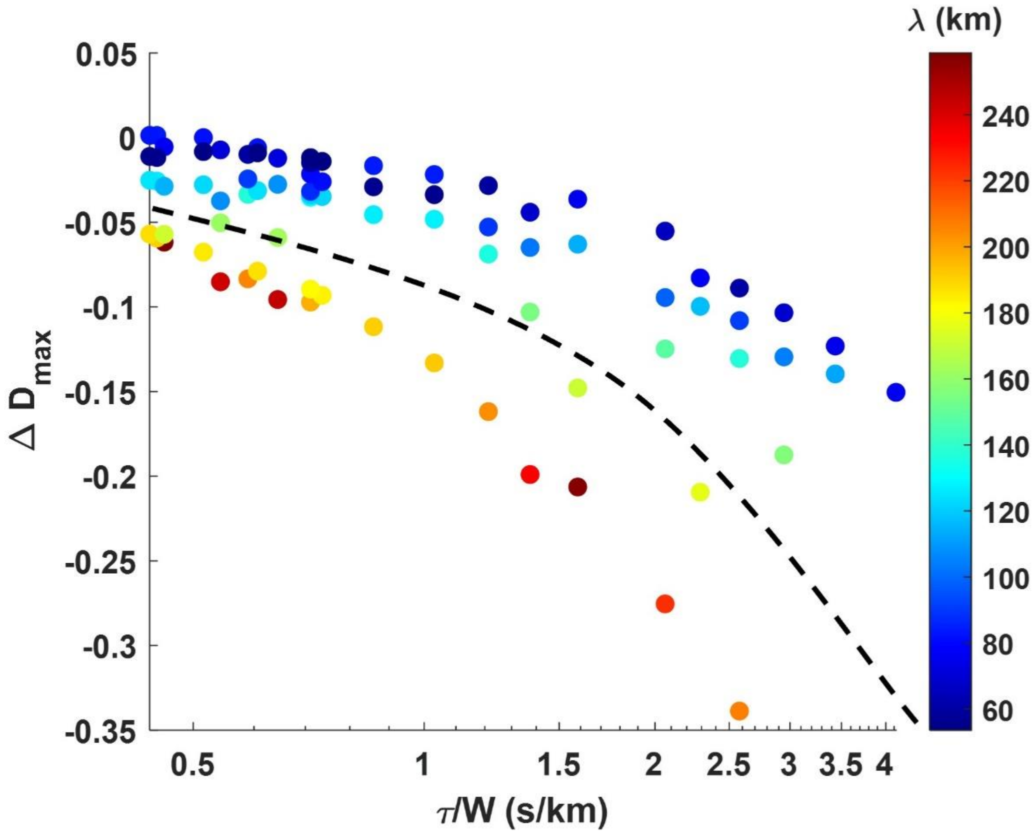

Figure S11. Relative discrepancy ΔD_{max} between time-dependent shallow water (TD-SW) and instantaneous source shallow water (IS-SW) results in terms of flow-depth at the first point on the coast as a function of τ/W with color scale marking the source horizontal extension λ. The black dashed line separates the two highlighted trends for small and large ruptures similarly to what is shown in the Figure 4(a) for the non-hydrostatic case.

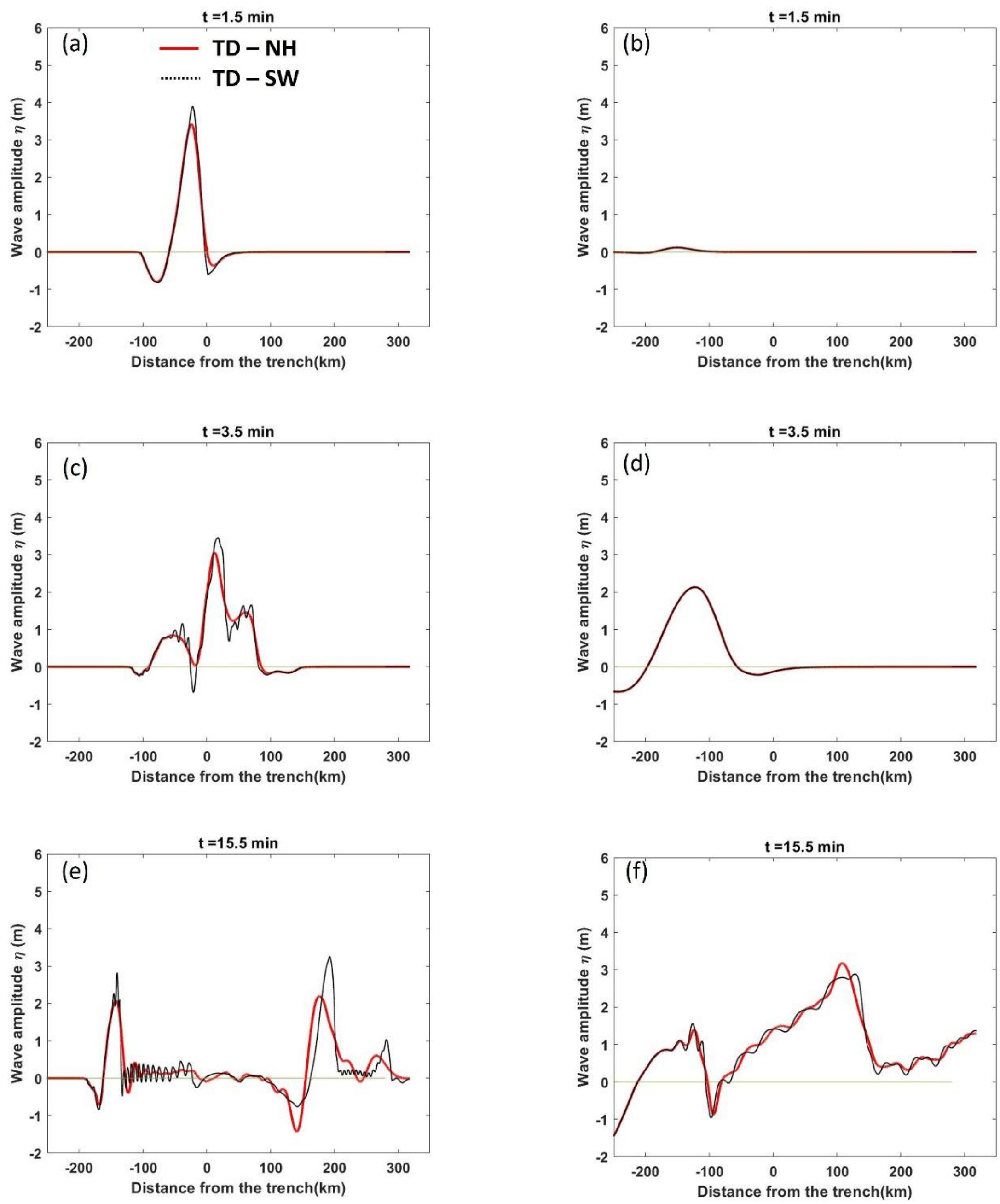

Figure S12. Wave amplitude as a function of the distance from the trench for TD – NH (red curves) and TD – SW (black dotted lines) at three different time steps and for two simulations: the ID 70 (left panels) and the ID 7 (right panels) in Table S2. These simulations represent examples of small and large size sources respectively. The whole evolution can be found in the Supporting Information (Movie S5 and S6)

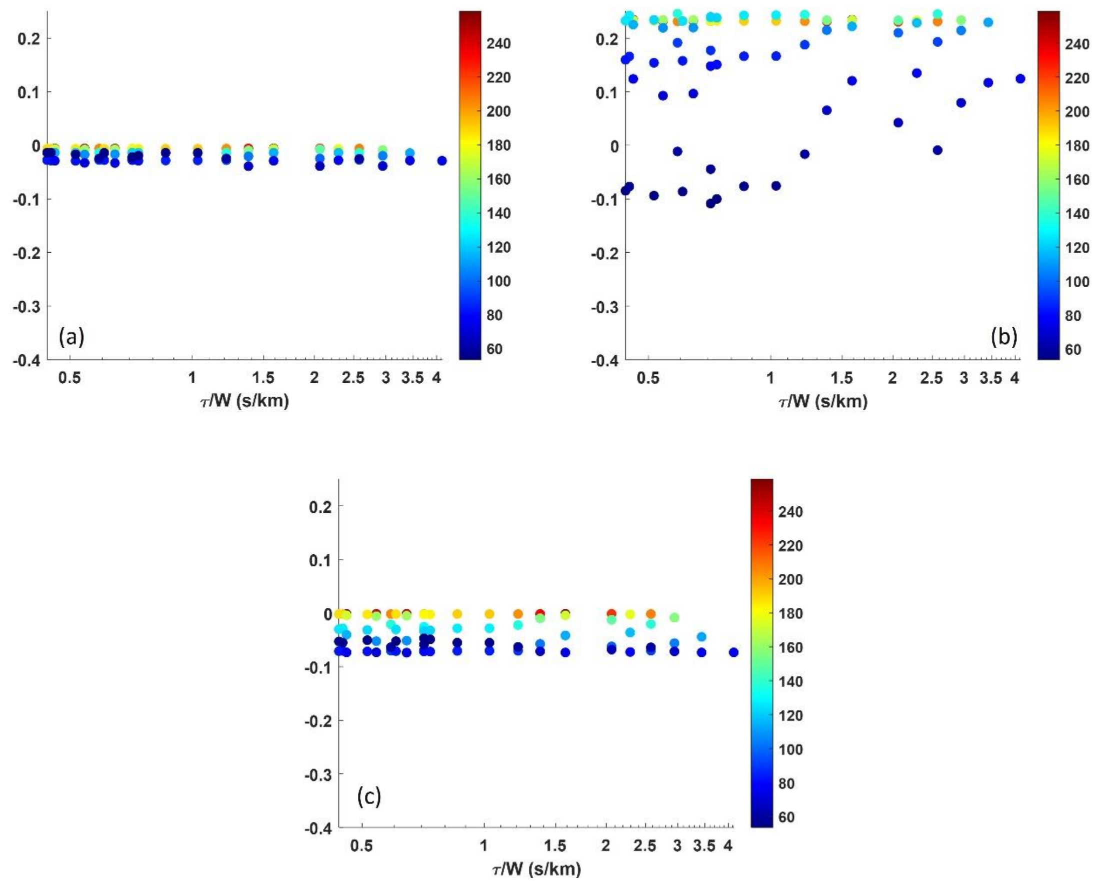

Figure S13. Relative discrepancy between Non-Hydrostatic (NH) and Shallow Water (SW) results when IS sources are used for both propagation regime. (a) $\Delta\eta_{max}$ at a gauge placed along the coastward propagation as a function of τ/W with color scale marking the source horizontal extension λ. (b) $\Delta\eta_{max}$ at a gauge placed rightward beyond the trench as a function of τ/W with color scale marking the source horizontal extension λ. (c) ΔD_{max} at the first point on coast as a function of τ/W with color scale marking the source horizontal extension λ. For sake of comparison the figures are plotted with the same scale.

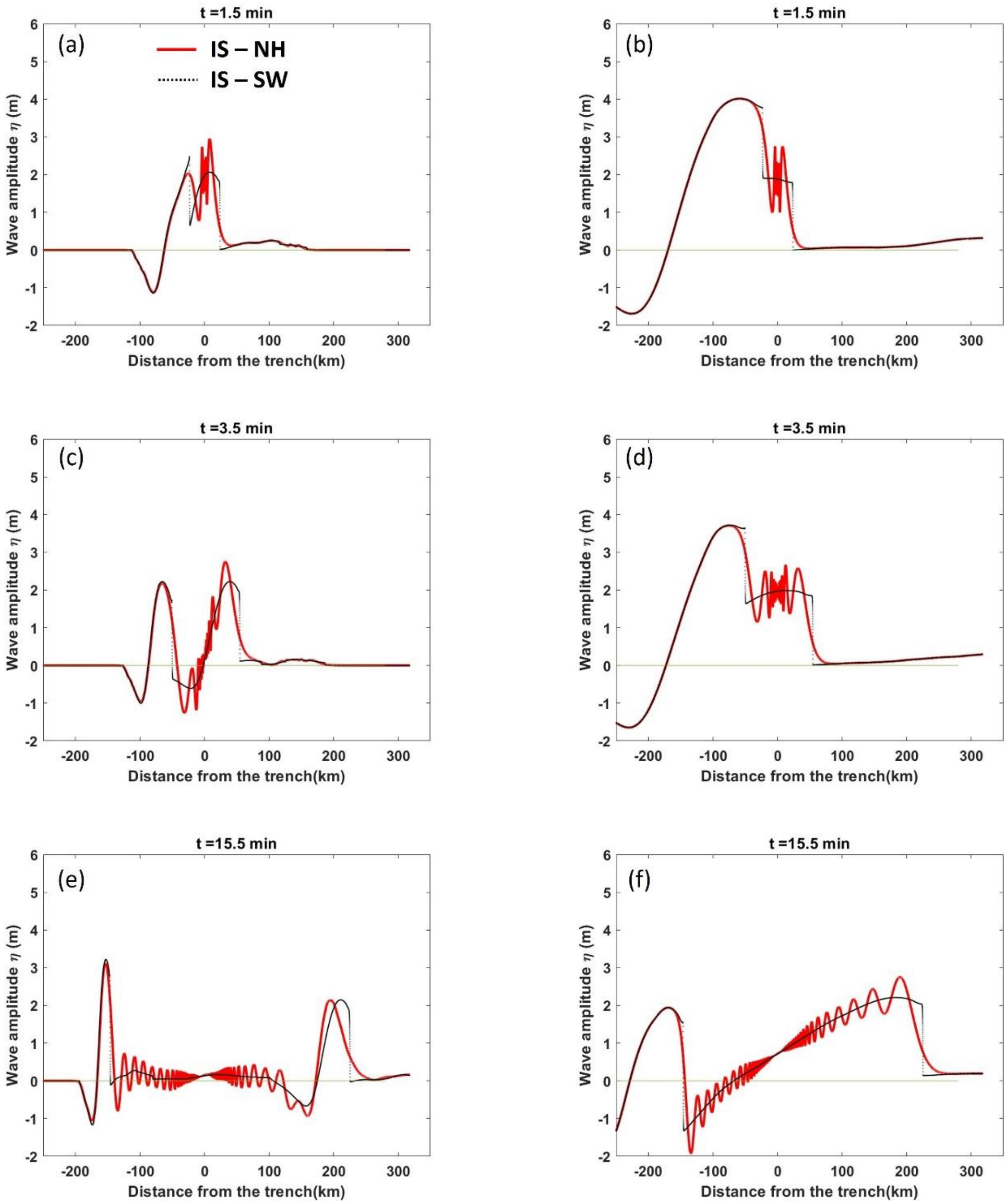

Figure S14. Wave amplitude as a function of the distance from the trench for IS – NH (red curves) and IS – SW (black dotted lines) at three different time steps and for two simulations: the ID 70 (left panels) and the ID 7 (right panels) in Table S2. These simulations represent examples of small and large size sources respectively. The whole evolution can be found in the Supporting Information (Movie S7 and S8)

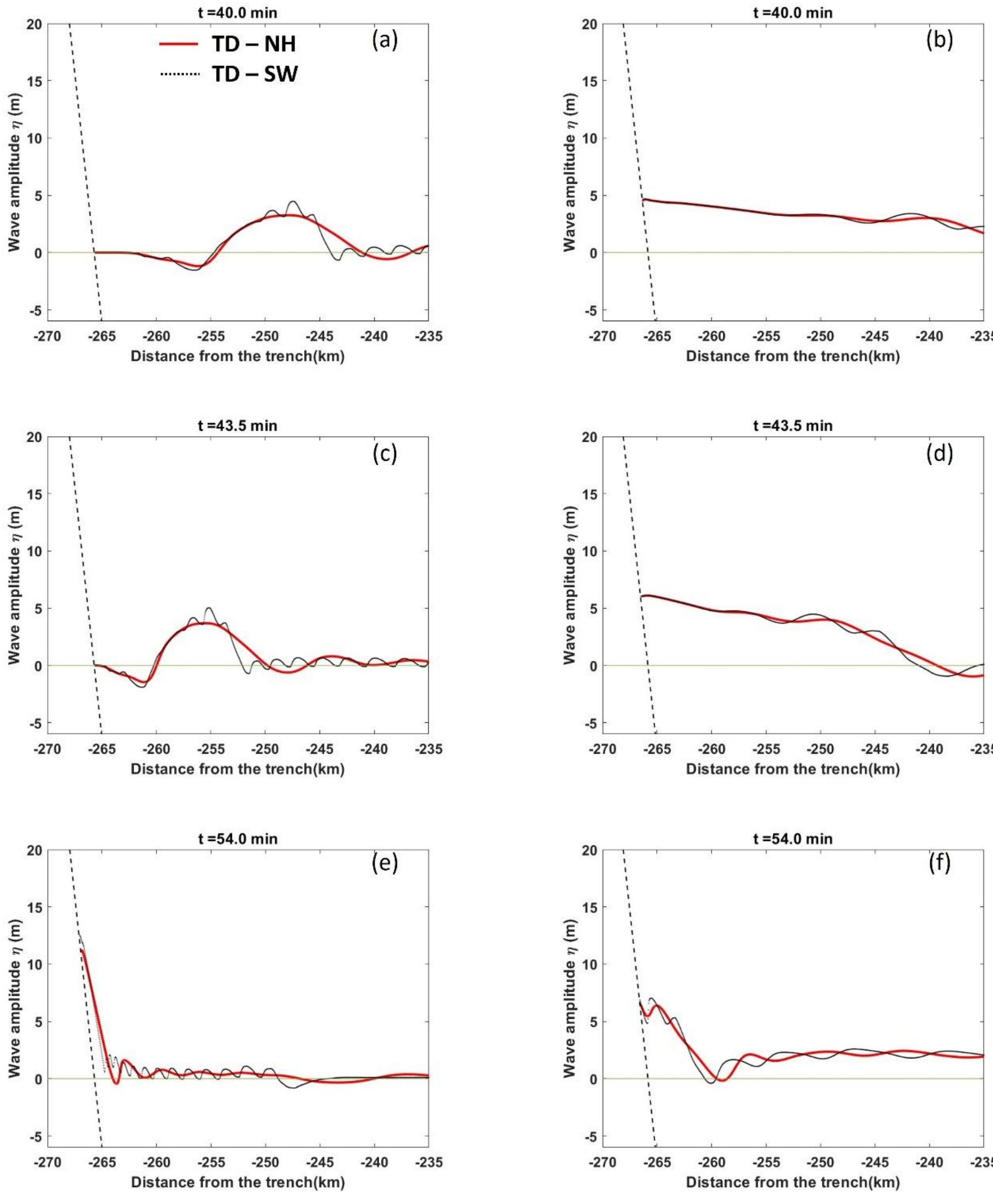

Figure S15 Wave amplitudes, zoomed around the coast, as a function of the distance from the trench for TD – NH (red curves) and TD – SW (black dotted lines) at three different time steps and for two simulations: the ID 70 (left panels) and the ID 7 (right panels) in Table S2. These simulations represent examples of small and large size sources respectively. The short-dashed line on the left represents the coast line within each panel. The whole evolution can be found in the Supporting Information (Movie S9 and S10).

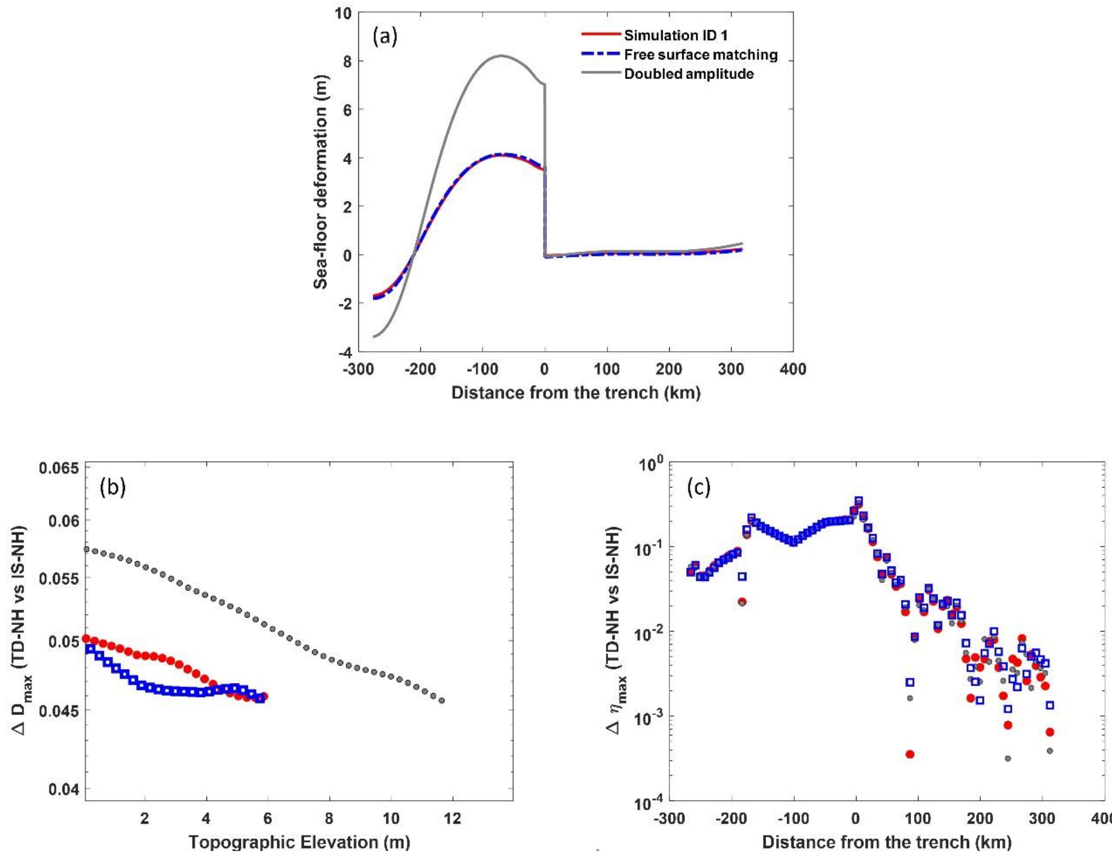

Figure S16 (a): Final sea-floor deformation for the simulation ID 1 in Table S2 (on the "Tohoku Hypo" bathymetry, red curve, "Simulation ID 1" in the legend) compared to the sea-floor deformation generated by a rupture dynamic simulation performed with a perfect matching between the free surface and the tsunami simulation bathymetry (blue dashed curve, "Free surface matching" in the legend). The grey curve represents a final sea-floor deformation with a doubled amplitude as compared to the red curve (grey curve, "Doubled amplitude" in the legend). For this test, these deformations have been used as initial conditions for further TD-NH (simulated with the same source dynamics) and IS-NH simulations. (b) ΔD_{max} (TD-NH vs IS-NH) at different topographic elevations for the initial conditions described in panel (a) (with the same color scheme). "Simulation ID 1" and "Free surface matching" simulations lead to ΔD_{max} values in the same range ([4.6%-5.0%]) converging to the same value in the vicinity of the maximum run-up. As expected, the high amount of available energy for "Doubled amplitude" simulations lead to larger discrepancies between IS and TD sources at the first points on the coast. Nevertheless, in the vicinity of the maximum run-up (doubled as compared to the other simulations) the ΔD_{max} converges to a consistent value as compared to the one from "Simulation ID 1". (c) $\Delta\eta_{max}$ (TD-NH vs IS-NH) offshore as a function of distance from the trench for the initial conditions described in panel (a) (with the same color scheme). Regardless of the different initial conditions $\Delta\eta_{max}$ takes on consistent values.

Table S1. Elastic and rheological parameters used to re-scale the dimensionless outputs of rupture dynamic simulations. In the last it is reported the subduction layer that can be realistically associated to the correspondent V_s, ρ and μ values

#	$\boldsymbol{V_s\ (km/s)}$	$\boldsymbol{\rho\ (g/cm^3)}$	$\boldsymbol{\mu\ (GPa)}$	***Layer***
1	0,35	1,80	0,22	Accretionary prism
2	0,5	1,95	0,49	//
3	0,6	2,00	0,72	//
4	0,7	2,05	1,00	//
5	0,8	2,07	1,32	//
6	0,9	2,10	1,70	//
7	1,0	2,15	2,15	//
8	1,3	2,20	3,72	//
9	1,5	2,25	5,06	//
10	1,7	2,30	6,65	//
11	2,0	2,35	9,4	//
12	2,4	2,45	14,11	//
13	2,9	2,60	21,87	Seismic bedrock
14	3,2	2,65	27,14	//
15	3,4	2,70	31,21	Upper crust layer
16	3,8	2,80	40,43	Lower crust
17	4,5	3,20	64,80	Mantle
18	2,8	2,60	20,38	Oceanic layer 1
19	2,9	2,40	20,18	//
20	3,5	2,80	34,3	Oceanic layer 2
21	4,0	2,90	46,4	//
22	4,6	3,40	71,94	Oc.-Cont. Mantle
23	4,7	3,20	70,69	Oceanic Mantle

Table S2 (In a separate file) Parameters (S-wave velocity, rigidity, stress drop and Dc from column to 2 to 5), duration (column 6) and width (column 7) for the 81 selected source models. They are ordered as indicated in column 1.

Table S3 Real subduction events used in Figure 8, classified according to their Moment magnitude Mw, stress drop, duration, width and dip

Event	**Date**	**Mw**	**Stress Drop (MPa)**	**Duration (s)**	**Width (km)**	**Dip (°)**
Nicaragua	1992-09-02	7.62	0.78	100	70	15
Java-Bali	1994-06-02	7.75	0.65	64	120	12
Peru	1996-02-21	7.50	0.76	79	70	14
Sumatra 2004	2004-12-26	9.10	4.3	567.35	330	16
Nias-Simeuleu	2005-03-28	8.61	1.20	142	275	8
Java-Pangandaran	2006-06-17	7.71	1.66	144.5	70	10
Sumatra 2007	2007-09-12	8.48	3.19	109	180	12
Papua	2009-01-03	7.66	1.75	51	65	28
Maule	2010-02-27	8.78	3.16	122	180	18
Tohoku foreshock	2011-03-09	7.34	1.76	22.5	55	12
Tohoku	2011-03-11	9.08	12.50	157.5	220	10
Iquique	2014-04-01	8.08	7.66	77.5	90	18

Movie S1. Wave amplitude time-evolution as a function of the distance from the trench for the simulations shown in Figures 2(a), 2(c) and 2(e).

Movie S2. Wave amplitude time-evolution as a function of the distance from the trench for the simulations shown in Figures 2(b), 2(d) and 2(f).

Movie S3. Inundation time-evolution as a function of the distance from the trench for the simulations shown in Figures 3(a), 3(c) and 3(e).

Movie S4. Inundation time-evolution as a function of the distance from the trench for the simulations shown in Figures 3(b), 3(d) and 3(f).

Movie S5. Wave amplitude time-evolution as a function of the distance from the trench for the simulations shown in Figures S12(a), S12(c) and S12(e) in Supporting Information.

Movie S6. Wave amplitude time-evolution as a function of the distance from the trench for the simulations shown in Figures S12(b), S12(d) and S12(f) in Supporting Information.

Movie S7. Wave amplitude time-evolution as a function of the distance from the trench for the simulations shown in Figures S14(a), S14(c) and S14(e) in Supporting Information.

Movie S8. Wave amplitude time-evolution as a function of the distance from the trench for the simulations shown in Figures S14(b), S14(d) and S14(f) in Supporting Information.

Movie S9. Inundation time-evolution as a function of the distance from the trench for the simulations shown in Figures S15(a), S15(c) and S15(e) in Supporting Information.

Movie S10. Inundation time-evolution as a function of the distance from the trench for the simulations shown in Figures S15(b), S15(d) and S15(f) in Supporting Information.

References

Adsuara, J. E., Cordero-Carrión, I., Cerdá-Durán, P., & Aloy, M. A. (2016). Scheduled Relaxation Jacobi method: Improvements and applications. *Journal of Computational Physics*, *321*, 369–413. https://doi.org/10.1016/j.jcp.2016.05.053

Beji, S., & Battjes, J. A. (1994). Numerical simulation of nonlinear wave propagation over a bar. *Coastal Engineering*, *23*(1–2), 1–16. https://doi.org/10.1016/0378-3839(94)90012-4

Castro Díaz, M. J., & Fernández-Nieto, E. (2012). A Class of Computationally Fast First Order Finite Volume Solvers: PVM Methods. *SIAM Journal on Scientific Computing*, *34*(4), A2173–A2196. https://doi.org/10.1137/100795280

Chazel, F., Lannes, D., & Marche, F. (2011). Numerical Simulation of Strongly Nonlinear and Dispersive Waves Using a Green–Naghdi Model. *Journal of Scientific Computing*, *48*(1–3), 105–116. https://doi.org/10.1007/s10915-010-9395-9

Chorin, A. J. (1968). Numerical Solution of the Navier-Stokes Equations. *Mathematics of Computation*, *22*(104), 745. https://doi.org/10.2307/2004575

Dingemans, M. W. (1994). *MAST PROJECT 1: WAVES G8-M Comparison of computations with Boussinesq-like models and laboratory measurements*.

Escalante, C., Fernández-Nieto, E. D., Morales de Luna, T., & Castro, M. J. (2019). An Efficient Two-Layer Non-hydrostatic Approach for Dispersive Water Waves. *Journal of Scientific Computing*, *79*(1), 273–320. https://doi.org/10.1007/s10915-018-0849-9

Escalante, C., Morales de Luna, T., & Castro, M. J. (2018). Non-hydrostatic pressure shallow flows: GPU implementation using finite volume and finite difference scheme. *Applied Mathematics and Computation*, *338*, 631–659. https://doi.org/10.1016/j.amc.2018.06.035

Kazolea, M., & Delis, A. I. (2013). A well-balanced shock-capturing hybrid finite volume–finite difference numerical scheme for extended 1D Boussinesq models. *Applied Numerical Mathematics*, *67*, 167–186. https://doi.org/10.1016/j.apnum.2011.07.003

Ma, G., Shi, F., & Kirby, J. T. (2012). Shock-capturing non-hydrostatic model for fully dispersive surface wave processes. *Ocean Modelling*, *43–44*, 22–35. https://doi.org/10.1016/j.ocemod.2011.12.002

Ricchiuto, M., & Filippini, A. G. (2014). Upwind residual discretization of enhanced Boussinesq equations for wave propagation over complex bathymetries. *Journal of Computational Physics*, *271*, 306–341. https://doi.org/10.1016/j.jcp.2013.12.048

Titov, V. V., & Synolakis, C. E. (1995). Modeling of Breaking and Nonbreaking Long-Wave Evolution and Runup Using VTCS-2. *Journal of Waterway, Port, Coastal, and Ocean Engineering*, *121*(6), 308–316. https://doi.org/10.1061/(ASCE)0733-950X(1995)121:6(308)

ID	$V_s\ (m/s)$	$\rho(kg/m^3)$	$\Delta\sigma\ (MPa)$	$D_c(m)$	$\mu\ (GPa)$	$\tau\ (s)$	$W\ (km)$
1	4500	3200	3.91	2	64.80	126.13	275.30
2	1300	2200	0.23	2	3.72	433.89	273.59
3	3200	2650	1.73	2	27.14	167.77	260.40
4	3800	2800	2.60	2	40.43	140.07	258.16
5	1500	2250	0.34	2	5.06	340.68	247.87
6	1000	2150	0.15	2	2.15	490.22	237.77
7	800	2070	0.10	2	1.32	567.48	220.20
8	3500	2800	2.60	2	34.30	129.01	219.01
9	1700	2300	0.51	2	6.65	262.61	216.54
10	2900	2600	1.73	2	21.87	149.18	209.83
11	2000	2350	0.77	2	9.40	210.04	203.75
12	2400	2450	1.15	2	14.11	174.84	203.53
13	4600	3400	5.88	2	71.94	91.15	203.37
14	4700	3200	5.88	2	70.69	87.65	199.82
15	3400	2700	2.60	2	31.21	120.85	199.29
16	4000	2900	3.91	2	46.40	101.60	197.13
17	2800	2600	1.73	2	20.38	144.03	195.61
18	2900	2400	1.73	2	20.18	137.70	193.69
19	900	2100	0.15	2	1.70	430.94	188.12
20	4500	3200	5.88	2	64.80	83.92	183.17
21	1300	2200	0.34	2	3.72	288.70	182.04
22	3200	2650	2.60	2	27.14	111.63	173.26
23	3800	2800	3.91	2	40.43	93.20	171.77
24	700	2050	0.10	2	1.00	491.75	166.96
25	1500	2250	0.51	2	5.06	226.68	164.92
26	1000	2150	0.23	2	2.15	326.18	158.21
27	800	2070	0.15	2	1.32	377.58	146.51
28	3500	2800	3.91	2	34.30	85.84	145.72
29	1700	2300	0.77	2	6.65	174.73	144.08
30	2900	2600	2.60	2	21.87	99.26	139.62
31	2000	2350	1.15	2	9.40	139.75	135.57
32	2400	2450	1.73	2	14.11	116.33	135.42
33	4600	3400	8.84	2	71.94	60.65	135.32
34	4700	3200	8.84	2	70.69	58.32	132.95
35	3400	2700	3.91	2	31.21	80.41	132.60
36	4000	2900	5.88	2	46.40	67.60	131.16
37	2800	2600	2.60	2	20.38	95.83	130.15
38	2900	2400	2.60	2	20.18	91.62	128.88
39	900	2100	0.23	2	1.70	286.73	125.17
40	4500	3200	8.84	2	64.80	55.84	121.88
41	1300	2200	0.51	2	3.72	192.09	121.12
42	600	2000	0.10	2	0.72	411.22	119.67
43	3200	2650	3.91	2	27.14	74.28	115.29
44	3800	2800	5.88	2	40.43	62.01	114.29
45	700	2050	0.15	2	1.00	327.19	111.09
46	1500	2250	0.77	2	5.06	150.83	109.73
47	1000	2150	0.34	2	2.15	217.03	105.27
48	800	2070	0.23	2	1.32	251.23	97.49
49	3500	2800	5.88	2	34.30	57.11	96.96
50	1700	2300	1.15	2	6.65	116.26	95.87
51	2900	2600	3.91	2	21.87	66.04	92.90
52	2000	2350	1.73	2	9.40	92.99	90.20
53	2400	2450	2.60	2	14.11	77.40	90.11
54	4600	3400	13.28	2	71.94	40.35	90.03
55	4700	3200	13.28	2	70.69	38.81	88.46
56	3400	2700	5.88	2	31.21	53.50	88.23
57	4000	2900	8.84	2	46.40	44.98	87.27

58	2800	2600	3.91	2	20.38	63.77	86.60
59	2900	2400	3.91	2	20.18	60.96	85.75
60	900	2100	0.34	2	1.70	190.78	83.28
61	4500	3200	13.28	2	64.80	37.15	81.09
62	500	1950	0.10	2	0.49	334.11	81.03
63	1300	2200	0.77	2	3.72	127.81	80.59
64	600	2000	0.15	2	0.72	273.61	79.63
65	3200	2650	5.88	2	27.14	49.42	76.71
66	3800	2800	8.84	2	40.43	41.26	76.05
67	700	2050	0.23	2	1.00	217.70	73.92
68	1500	2250	1.15	2	5.06	100.36	73.01
69	1000	2150	0.51	2	2.15	144.40	70.04
70	800	2070	0.34	2	1.32	167.16	64.86
71	3500	2800	8.84	2	34.30	38.00	64.51
72	1700	2300	1.73	2	6.65	77.36	63.79
73	2900	2600	5.88	2	21.87	43.94	61.81
74	2000	2350	2.60	2	9.40	61.87	60.02
75	2400	2450	3.91	2	14.11	51.50	59.95
76	4600	3400	19.96	2	71.94	26.85	59.91
77	4700	3200	19.96	2	70.69	25.82	58.86
78	3400	2700	8.84	2	31.21	35.60	58.70
79	4000	2900	13.28	2	46.40	29.93	58.07
80	2800	2600	5.88	2	20.38	42.43	57.62
81	2900	2400	5.88	2	20.18	40.56	57.06